Autofocus and Back-Projection in Synthetic Aperture Radar Imaging

by

Hyun Jeong Cho

A dissertation submitted in partial fulfillment
of the requirements for the degree of
Doctor of Philosophy
(Electrical Engineering: Systems)
in the University of Michigan
2016

Doctoral Committee:

Professor David C. Munson, Jr., Chair
Associate Professor Ryan M. Eustice
Professor Jeffrey A. Fessler
Professor Andrew E. Yagle

2016

TABLE OF CONTENTS

LIST OF FIGURES

LIST OF TABLES

LIST OF APPENDICES

LIST OF ABBREVIATIONS

BFA Beam Forming Algorithm

CT Computed Tomography

DEM Digital Elevation Model

DFT Discrete Fourier Transform

FBP Filtered Back-Projection

FBPC Filtered Back-Projection along Curves

FFBP Fast Factorized Back-Projection

FFT Fast Fourier Transform

FM Frequency Modulation

FMCA Fourier-domain MultiChannel Autofocus

FOV Field Of View

GPS Global Positioning System

HPHW Half-Power Half-Width

ISLR Integrated SideLobe Ratio

MCA MultiChannel Autofocus

NRMSE Normalized Root-Mean-Squared Error

PFA Polar Formatting Algorithm

PGA Phase Gradient Autofocus

PSLR Peak SideLobe Ratio

PTR Point Target Response

RMCA Reversed-step MultiChannel Autofocus

RMSE Root-Mean-Squared Error

SAR Synthetic Aperture Radar

UAVs Unmanned Aerial Vehicles

ABSTRACT

Spotlight-mode Synthetic Aperture Radar (SAR) imaging has received considerable attention due to its ability to produce high-resolution images of scene reflectivity. One of the main challenges in successful image recovery is the problem of defocusing, which occurs due to inaccuracies in the estimated round-trip delays of the transmitted radar pulses. The problem is most widely studied for far-field imaging scenarios with a small range of look angles since the problem formulation can be significantly simplified under the assumptions of planar wavefronts and one-dimensional defocusing. In practice, however, these assumptions are frequently violated.

MultiChannel Autofocus (MCA) is a subspace-based approach to the defocusing problem that was originally proposed for far-field imaging, with a small range of look angles. A key motivation behind MCA is the observation that there exists a low-return region within the recovered image, due to the weak illumination near the edges of the antenna footprint. The strength of the MCA formulation is that it can be easily extended to more realistic scenarios with polar-format data, spherical wavefronts, and arbitrary terrain, due to its flexible linear-algebraic framework.

The main aim of this thesis is to devise a more broadly effective autofocus approach by adopting MCA to the aforementioned scenarios. By forming the solution space in a domain where the defocusing effect is truly one-dimensional, we show that drastically improved restorations can be obtained for applications with small to fairly wide ranges of look angles. When the terrain topography is known, we utilize the versatile backprojection-based imaging methods in the model formulations for MCA to

accurately account for the underlying geometry. The proposed extended MCA shows reductions in RMSE of up to 50% when the underlying terrain is highly elevated. We also analyze the effects of the filtering step, the amount of wave curvature, the shape of the terrain, and the flight path of the radar, on the reconstructed image via backprojection. Finally, we discuss the selection of low-return constraints and the importance of using terrain elevation within MCA formulation.

CHAPTER 1

Introduction

1.1 Motivation

The tomographic formulation of Synthetic Aperture Radar (SAR) imaging established that the acquired SAR data are Fourier transforms of the projections of the underlying scene. This formulation has paved the way for the development and understanding of numerous efficient and effective imaging algorithms to produce high-resolution images. Among these, methods based on the 2-D Fourier transformation have been widely employed and well studied for scenarios where the radar is operating in the far-field. Under such a setting, the SAR data can be interpreted as samples of the 2-D Fourier transformation of the underlying image (terrain reflectivity).

More recently, a different class of imaging algorithms, based on backprojection, has received considerable attention due to the development of fast backprojection techniques that make backprojection computationally competitive with Fourier inversion techniques. Backprojection-based methods are especially effective for challenging scenarios where the the SAR data are not a 2-D Fourier transform of the underlying scene. These scenarios include the case of near-field imaging, cases where the radar travels on an arbitrary flight path, or situations where the topography of the scene is not flat.

To utilize 2-D Fourier transform based methods for these scenarios, image reconstruction algorithms must employ sophisticated post-processing steps to remove the defocus and other defects caused by non-ideal situations, i.e., imaging scenarios that are not 2-D and in the far field. Backprojection offers a more general framework that has the potential to integrate such complicated scenarios directly into the formulation. However, despite such promising potential, the performance of backprojection-based algorithms has not been studied in depth.

Another challenge in SAR imaging is that the recovered images can suffer from severe defocusing caused by inaccuracies in the estimated round-trip travel time of the transmitted radar pulses. This is one of the main challenges in high-resolution SAR imaging. Even with modern state-of-the-art Global Positioning System (GPS) technology, unknown aircraft motion, or inho-

mogeneities in the ionosphere in the case of imaging from satellites, pose challenges in estimating the round-trip delays accurately enough, especially for radars with short wavelengths. To address the defocusing problem, numerous algorithms have been proposed that are referred to as autofocus algorithms. The majority of these algorithms in the literature are heuristic or rely on assumptions that are satisfied only in limited scenarios.

Recently, a linear-algebraic solution, called MultiChannel Autofocus (MCA), has been proposed by Morrison, et al. MCA was motivated by the observation that a portion of the underlying scene is weakly illuminated due to the spatially limited nature of the antenna footprint. As a result, it is expected that the reconstructed image will have low values in that same region. MCA exploits this fact and estimates the phase errors by formulating the problem as one of finding the minimizer of the energy in the presumed low-return region. Thus, the coordinates of the presumed low return region are fed into the algorithm as constraints. Naturally, the performance of MCA depends on the choice of these constraints. It is not known how to optimally choose the coordinates of the low-return constraints to provide the best restoration, but many choices can work well.

MCA is highly effective and performs well even for severely defocused images that other autofocus algorithms find difficult to focus. However, MCA assumes that the wavefronts are planar and that the defocusing effect is one-dimensional in the reconstructed image. Similar to many other autofocus algorithms that rely on these assumptions, MCA does not perform well when the assumptions are violated. For example, the assumptions break down when the data are collected over a wide range of look angles, or in a near-field imaging scenario. Fortunately, MCA has the potential to be adapted to a more general set of scenarios, because the collected data and the reconstructed image are still related via linear equations.

The goal of this research is threefold. The first is to improve the linear algebraic approach to the defocusing problem for realistic imaging scenarios. This involves settings where the data are collected on a polar (versus nearly Cartesian) grid or when the underlying terrain is not flat or the radar flight path is arbitrary. Using an accurate model formulation for such settings, we wish to develop an effective autofocus algorithm using an MCA-type approach. The second goal is to provide insight to the choice of low-return constraints for MCA and determine how different choices affect the restoration results. Our final goal is to study the performance of backprojection-based imaging algorithms when a Digital Elevation Model (DEM) of the terrain is known. The aim of this study is to understand the dependency of the image quality on geometric properties of the imaging scenarios under consideration and to determine how MCA might be modified to incorporate a DEM.

1.2 Outline and Contributions

The organization of this thesis is as follows. In Chapter 2, we begin with an overview of the tomographic formulation of SAR imaging and an introduction to the defocusing problem. This is followed by a summary of existing autofocus approaches with a particular emphasis on MCA.

In Chapter 3, we observe that MCA is far more sensitive to violation of the one-dimensional defocusing assumption compared to other methods. In fact, standard MCA is unsuitable for even fairly small data-collection angles, where the deviation of the polar Fourier grid from Cartesian is very small. Fortunately, this problem can be solved if we reverse the order of two steps in the image formation process and apply MCA in a domain where the defocusing effect is one-dimensional. The distorted version of the image, obtained by inverse Fourier transforming the polar-grid data without interpolation onto a Cartesian grid, also contains regions satisfying a low-return assumption, but the region of low return must be carefully specified for best performance. Simulation results show that the proposed method restores well-focused images for up to fairly large range of look angles. Issues in the selection of low-return constraints are discussed.

In Chapter 4, we study the impact of using different low-return constraints for MCA. MCA works best when the low-return region is known accurately. In practice, the returns from within the sidelobes of the antenna footprint are highly attenuated providing a region of highly probable low returns. However, scene-dependent features like strong reflectors in the highly attenuated region may violate the assumptions underlying MCA, resulting in performance degradation. We consider such a scenario and propose scene-independent, random selection methods of the low-return constraints. Simulation results show that a well-focused image can be obtained within a few trials, even when the number of anomalies is moderately large. Also, we discuss whether a particular geometry of the low-return region is beneficial or detrimental for MCA.

In Chapter 5, we present a theoretical study that considers whether filtering is necessary in backprojection for SAR imaging. Backprojection-based SAR imaging methods are especially well suited for the near-field case where the SAR data are no longer a 2-D Fourier transform of the underlying image. However, there is no known exact filter for the near-field backprojection case, where a spatially variant, and thus computationally expensive filter is needed for a good reconstruction. In practice, it is thought that filtering is not as important in SAR imaging as it is in medical imaging, and so sometimes the filtering step is omitted during the imaging process. Our analysis in this chapter shows that the bandwidth-to-center-frequency ratio of the radar is the key parameter that determines the importance of filtering. Simulation results demonstrate that omission of the filtering step does not change the image quality significantly for most practical ranges of radar parameters and amounts of wavefront curvature. However, the effect of filtering is less negligible for the near-field and wide-band cases. We provide a guideline for assessing the importance of the

filtering step, based on the effect of filtering on point target resolution.

In Chapter 6, we study imaging and autofocus algorithms for the scenario when a DEM is known. Backprojection-based imaging can be extended to correctly account for the terrain elevations and wavefront curvature by backprojecting along correct curves. We study the dependency of the image quality on various geometric parameters by analyzing point target resolution. Such parameters include the terrain gradients, the radar elevation, and the amount of wavefront curvature. Based on this analysis, we discuss the importance of using the correct DEM within a one-step imaging process. Furthermore, we extend the use of MCA to scenarios with non-flat terrain or near-field imaging geometries by directly incorporating the DEM into formulation of the autofocus optimization problem. We then present simulation results for this extended MCA for various DEMs and amounts of wavefront curvature.

Finally, in Chapter 7 we summarize this thesis and present possible future research topics.

CHAPTER 2

Background

2.1 Tomographic Formulation of Spotlight-Mode SAR

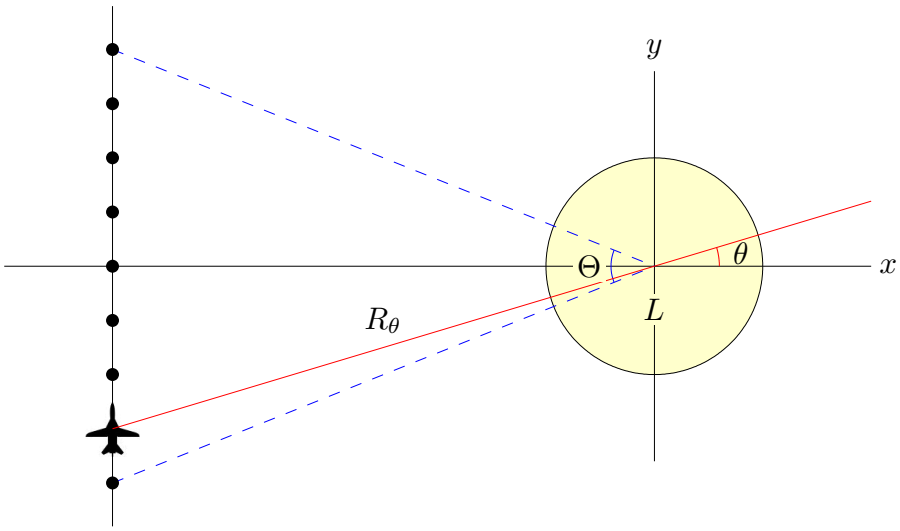

Figure 2.1: Geometry of data collection in spotlight-mode SAR.

In our development, we consider spotlight-mode SAR because this high-resolution form of SAR ordinarily uses short wavelengths, where the need for autofocus is most pressing. In spotlight mode, the radar pulses are transmitted toward a fixed reference point on the scene of interest. The geometry of a spotlight-mode imaging scenario is shown in Fig. 2.1. The patch to be imaged is depicted as the shaded circular region of diameter L, and the radar is at distance R_θ from the center of the scene when the look angle is θ. The radar platform illuminates the terrain patch and collects the backscattered pulses, which are acquired for look angles θ_l: $\theta_{\min} \le \theta_l \le \theta_{\max}$, $l = 1, 2, \ldots, N_\theta$, where $\Theta = \theta_{\max} - \theta_{\min}$ is the range of look angles. The direction of the flight path is referred to as the cross-range or azimuth direction and the direction perpendicular to the flight path is referred to as the range direction. x and y denote the range and cross-range coordinates, respectively. Here, the goal is to reconstruct the complex-valued reflectivity $g(x,y)$ of the ground patch.

A linear Frequency Modulation (FM) chirp is a waveform commonly employed in imaging radars due to its ability to obtain high range resolution. It is described by $\mathrm{Re}\{s(t)\}$, with

$$s(t) = \mathrm{e}^{j(\omega_0 t + \alpha t^2)}, \quad t \in [-T/2, T/2], \tag{2.1}$$

where ω_0 is the center frequency, 2α is the chirp rate, and T is the pulse duration. Returns from each look angle are processed using knowledge of the round-trip delay $2R_\theta/c$. The process, referred to as quadrature demodulation, is done by mixing the return with in-phase and quadrature versions of the chrip, followed by low-pass filtering [1]. By ignoring the quadratic phase term, the demodulated data from each look angle can be interpreted as 1-D Fourier transforms of the projections of g. Here, the projections are taken along equidistant lines/arcs onto the line of pulse transmission.

When the radar is operating in the far field, i.e. when $R_\theta \gg L$, the data for look angle θ are also a slice of the 2-D Fourier transform of g taken at angle θ by the projection-slice theorem [1]. That is, the data for look angle θ are

$$G(\rho\cos\theta, \rho\sin\theta), \quad \frac{1}{\pi c_0}(\omega_0 - \alpha T) \le \rho \le \frac{1}{\pi c_0}(\omega_0 + \alpha T), \tag{2.2}$$

where $G(f_X, f_Y)$ is the 2-D Fourier transform of $g(x,y)$ and c_0 is the speed of light. The demodulated data are available for a limited range of spatial frequencies. Since $\omega_0 > \alpha T$ in general, the region of support of the acquired Fourier data is on a polar annulus, offset from the origin. The angular extent of the demodulated data is the same as the range of data collection angles.

The demodulated data are sampled to form a discrete set of SAR data

$$G_p[l,k] = G(f_R[k]\cos\theta_l, f_R[k]\sin\theta_l), \quad k = 1,\ldots,N_\rho,\ l = 1,\ldots,N_\theta, \tag{2.3}$$

where $\{f_R[k]\}$ are the radial samples of the Fourier data. In practice, due to the limited and tapered support of the radar antenna beam, the demodulated returns correspond to the Fourier transforms of the weighted reflectivity $g(x,y)w(x,y)$, where $w(x,y)$ is the antenna beam pattern. The support of $w(x,y)$ is nearly limited to a particular region in space, so some region in the scene may be weakly illuminated.

In this chapter, we only consider far-field imaging and also assume that the elevations of the radar and the scene are zero for simplicity. In Chapter 5, notation and formulas will be re-introduced for a more general case of near-field imaging. Furthermore, SAR imaging with an arbitrary terrain and elevated radar will be introduced with 3-D collection geometry in Chapter 6.

2.2 SAR Imaging Methods for Far-Field Imaging

2.2.1 Polar Formatting Algorithm

Since the SAR data are samples of the 2-D Fourier transform of g, a popular means of image formation, termed Polar Formatting Algorithm (PFA), uses 2-D inverse Fourier transformation [1]. To utilize fast algorithms for Fourier transformation, the polar-grid data usually is first interpolated onto a Cartesian grid. The interpolated SAR data can be described by

$$G_c[l',k'] = \sum_{l=1}^{N_\theta} \sum_{k=1}^{N_\rho} G_p[l,k]\Psi_{PC}[l',k';l,k], \tag{2.4}$$

where Ψ_{PC} is a polar-to-Cartesian interpolation kernel, and l' and k' are indices corresponding to sample points in the range and cross-range spatial frequencies, respectively. By taking a 2-D inverse Discrete Fourier Transform (DFT) of G_c, we obtain the image $g_c[m,n] = DFT^{-1}_{l',k'}\{G_c[l',k']\}$.

2.2.2 Filtered Back-Projection

Filtered Back-Projection (FBP) is another tomographic reconstruction method that can be used for SAR imaging. With a filter Q in the Fourier domain, the reconstruction at location (x,y) can be described as

$$g_{\text{FBP}}(x,y) = \sum_{l=1}^{N_\theta} \sum_{k=1}^{N_\rho} G_p[l,k]Q[k]\mathrm{e}^{j2\pi f_R[k](x\cos\theta_l + y\sin\theta_l)}. \tag{2.5}$$

Since we are given the Fourier transformations of a band-pass data at an offset frequency range $[\omega_0 - \alpha T, \omega_0 + \alpha T]/(\pi c_0)$, accurate processing (which includes interpolation) is greatly simplified via demodulation by the carrier frequency [2]. In practice, FBP is done by using interpolation and FFT and the computational cost is dominated by the cost of back-projection. A straightforward implementation of back-projection is computationally more expensive ($O(N^3)$ for an N-by-N image) than PFA, but, as noted earlier, fast algorithms have been developed [3–5] that have a computational cost equivalent to that of PFA ($O(N^2 \log N)$).

2.3 Existing Autofocus Approaches for Far-Field Imaging

2.3.1 SAR Defocusing Problem

An accurate reconstruction of the image requires precise knowledge of any variation in the round-trip distances, $2R_\theta$, which may be difficult to measure within a small fraction of a wavelength.

As a result, each of the demodulated returns is contaminated with an unknown phase shift. The contaminated returns can be described by

$$\tilde{G}_p[l,k] = G_p[l,k]\, e^{j\phi_l}, \quad \forall\, l,k, \tag{2.6}$$

where ϕ_l is the unknown phase shift corresponding to the return from look angle θ_l [6]. Generally, the measurement errors are different for each return, and the resulting phase errors are considered to be a one-dimensional function of the look angle. In the presence of phase errors, the reconstructed image becomes improperly focused, and the resulting challenge is referred to as the SAR defocusing problem.

The aim of SAR autofocus is to restore a properly focused image given the set of contaminated SAR data $\{\tilde{G}_p[l,k]\}$ and assumptions about characteristics of the underlying scene. A common assumption is that the range of look angles Θ is small so that the polar data grid in the Fourier domain is nearly Cartesian. Then, the contaminated data on a Cartesian grid are approximated as

$$\tilde{G}_c[l',k'] = G_c[l',k']\, e^{j\phi_{1D}[l']}, \quad \forall\, l',k', \tag{2.7}$$

where ϕ_{1D} is a 1-D phase-error function depending only on the cross-range index l'. Since the resulting image under this model is blurred only in one spatial direction, the small-angle assumption is also known as the one-dimensional defocusing assumption. The 1-D error model, Eq. (2.7), is frequently used since it greatly simplifies the defocusing problem.

2.3.2 1-D Autofocus Methods

Existing efficient autofocus methods estimate the phase-error function ϕ_{1D} under the 1-D defocusing assumption along with other reasonable assumptions.

For example, the inverse filtering method assumes that there is a well-isolated point reflector in the scene. The phase errors are estimated by interpreting the neighborhood pixel values of the point reflector as the blurring function of the phase errors. This method only works for scenes with at least one strong reflector and is highly sensitive to noise [6]. Map drift [7] is a parametric method that models the phase errors with a low-order polynomial. Images formed with only a subset of aperture are assumed to be a "drifted" version of other sub-aperture images, where the amount of drift is determined by the relative phase shift of the sub-aperture. Map drift uses cross-correlations of the sub-aperture images to find the relative drift, and consequently, the phase errors. However, the method only works with low-order phase error functions.

Phase Gradient Autofocus (PGA) [8] implicitly assumes that several strong reflectors exist at various ranges in the scene. Furthermore, the clutters around strong reflectors are assumed to

follow a Gaussian noise model [9] to admit a maximum-likelihood estimation. The phase errors are estimated and refined through iterative corrections. PGA is widely employed in practice. However, the performance is deteriorated when there are insufficient number of strong reflectors, or when the phase errors are rapidly varying across look angles, or even when each phase error independently follows a uniform distribution between $-\pi$ and π.

Metric-based autofocus methods [10–17] assume the suitability of a particular image focus metric, such as intensity-squared [10, 11], image contrast [13], or image entropy [15–17]. These algorithms use iterative optimization approaches to estimate the phase errors. Generally, they show good performance when the underlying images comply with the employed focus metric. Image entropy is one of the widely used metrics since its relation to autofocus parameters facilitates numerical optimization [14] and there is extensive literature on blind deconvolution using entropy [18–20]. Entropy of an image g is defined as:

$$-\sum_{m,n} |\bar{g}[m,n]|^2 \ln(|\bar{g}[m,n]|^2), \tag{2.8}$$

where $\bar{g}[m,n] = g[m,n]/(\sum_{m,n}|g[m,n]|^2)$ is the power-normalized image. Image entropy measures the concentration of energy so that images with highly localized intensity have low entropy and are considered to be focused. Note that we will use image entropy as a performance measure of autofocus algorithms throughout this thesis.

2.3.3 Multichannel Autofocus

Like most autofocus methods, MCA was developed under the 1-D defocusing assumption [21]. MCA additionally assumes that a small portion of the perfectly-focused image is zero-valued, or least nearly zero-valued. This assumption of a low-return region is satisfied in practice due to the spatial limitation of the antenna footprint.

In matrix notation, MCA describes the autofocused image $\hat{\mathbf{g}} \in \mathbb{C}^{N_Y \times N_X}$ in terms of the contaminated Cartesian-grid Fourier data $\tilde{\mathbf{G}}_\mathbf{c} \in \mathbb{C}^{N_Y \times N_X}$ and phase compensations $\hat{\boldsymbol{\phi}} \in \mathbb{C}^{N_Y}$ as:

$$\hat{g}[m,n] = \boldsymbol{\Phi}_{\text{MCA},\{[m,n]\}} \mathbf{e}^{-j\hat{\boldsymbol{\phi}}}, \qquad \forall\ m,n \tag{2.9}$$

where $\mathbf{e}^{-j\hat{\boldsymbol{\phi}}}$ is an $N_Y \times 1$ vector with entries $\mathrm{e}^{-j\hat{\phi}_l}$, $l = 1,\ldots,N_Y$, and $\boldsymbol{\Phi}_{\text{MCA},\{[m,n]\}}$ is a $1 \times N_Y$ vector with its l'-th entry being the 1-D DFT of $\tilde{\mathbf{G}}_\mathbf{c}$:

$$\Phi^{(l')}_{\text{MCA},\{[m,n]\}} = \sum_{k'=1}^{N_X} \tilde{G}_c[l',k']\, \mathrm{e}^{j2\pi\left(\frac{nk'}{N_X}+\frac{ml'}{N_Y}\right)}. \tag{2.10}$$

(Note that this formula is different from the one in [21]; however, they are equivalent descriptions.)

Now, let $\Omega \subset [1 : N_Y] \times [1 : N_X]$ denote the set of discrete indices corresponding to the presumed low-return region, i.e.,

$$|\hat{g}[m,n]| \approx 0, \quad \forall\, [m,n] \in \Omega. \tag{2.11}$$

The samples of the phase-compensated image that correspond to the presumed low-return region can be concatenated into a vector: $\hat{\mathbf{g}}_\Omega = \mathbf{\Phi}_{\text{MCA},\Omega}\, \mathrm{e}^{-j\hat{\boldsymbol{\phi}}}$, where $\mathbf{\Phi}_{\text{MCA},\Omega}$ is a $|\Omega| \times M$ matrix, composed of row vectors $\{\mathbf{\Phi}_{\text{MCA},\{[m,n]\}} : [m,n] \in \Omega\}$. MCA aims to find the phase compensations $\hat{\boldsymbol{\phi}}$ that minimize $\|\hat{\mathbf{g}}_\Omega\|_2$ and estimates the phase errors by

$$\hat{\boldsymbol{\phi}}_{MCA} = -\angle\left\{\text{argmin}_{\|\mathbf{v}\|_2=1} \|\mathbf{\Phi}_{\text{MCA},\Omega}\mathbf{v}\|_2\right\}. \tag{2.12}$$

Here, the all-pass condition for the correction filter $\mathrm{e}^{-j\hat{\boldsymbol{\phi}}}$ is relaxed and a general filter $\mathbf{v}$ is used to create a linear framework [22].

When the presumed low returns are exactly zero and $\mathbf{\Phi}_{\text{MCA},\Omega}$ has rank $N_Y - 1$, MCA recovers the focused image exactly. However, the restoration is not guaranteed to be exact in most other cases. The accuracy of the estimate is greatly related to the choice of low-return pixels and their values; thus, the low-return constraints must be chosen carefully.

CHAPTER 3

Overcoming Polar-Format Issues in SAR Multichannel Autofocus

3.1 Introduction

SAR is a microwave imaging system that achieves a narrow effective beam, and thus high cross-range resolution, by synthetically increasing the size of the aperture. The aperture synthesis is accomplished by translating a small antenna across the desired aperture, collecting data from multiple vantage angles, and using post-processing of the data afterwards. In the tomographic formulation of spotlight-mode SAR, the demodulated data corresponding to a vantage angle θ are essentially a slice of the 2-D Fourier transform of the reflectivity at angle θ [1]. Thus, SAR data lies on a polar grid in the Fourier domain, and a natural means of image formation is to apply two-dimensional inverse Fourier transformation after interpolating the data onto a Cartesian grid.

Perfect demodulation requires accurate knowledge of the distance between the center of the image patch and the radar platform for each vantage angle. Although modern GPS-equipped SAR systems can estimate the distance with fair accuracy, for high frequency SARs it is difficult to measure the distance within a small fraction of the wavelength from a moving platform, as needed. As a result, the demodulated data typically is contaminated with unknown phase shifts. When imaging from space, unknown phase shifts also can be imparted by spatially-varying and time-varying properties of the ionosphere. The phase errors are modeled as dependent on the vantage angle only, and hence are one-dimensional. In the presence of the phase errors, the resulting image is improperly focused [6].

In recent decades, a number of solutions to the defocusing problem, referred to as *autofocus* methods, have been proposed and studied [8–10, 16, 17, 21]. Most autofocus algorithms are well-motivated, but heuristic. But, a more recently proposed autofocus method, named MCA is a subspace-based approach that directly solves for the correction filter [21]. Unlike other methods,

[0]This chapter includes research conducted jointly with David C. Munson, Jr. [23, 24].

MCA does not assume anything about the underlying scene, such as strong point scatterers or the suitability of image focus metrics. Instead, MCA assumes that a small portion of the perfectly focused image is zero-valued, or at least nearly zero-valued, which is satisfied in practice due to the spatial limit of the antenna beam. Under the image support constraint, in principle, MCA can provide a better or even perfect restoration of the focused image, compared to other methods. Furthermore, unlike most autofocus methods, the performance of MCA does not depend heavily on the nature of the phase error.

MCA and other efficient autofocus algorithms estimate the phase errors based on the assumption that the effect of defocusing on the image is one-dimensional. This assumption is nearly satisfied when the range of data collection angles is small, so that the polar raster for the acquired Fourier data does not deviate much from a Cartesian grid. However, as the range of angles becomes wider, the blurring kernel no longer can be approximated as a one-dimensional function in the cross-range direction, and so the algorithms fail to focus the image properly. Although many SAR applications use a narrow range of data collection angles (a few degrees), there are applications, such as bistatic SAR imaging and imaging using Unmanned Aerial Vehicles (UAVs), that require a wider range of data collection angles (up to tens of degrees). As we shall show, MCA is particularly sensitive to the one-dimensional defocusing assumption.

In [23], we proposed to improve the MCA approach by interchanging the interpolation step and the autofocus step; instead of applying MCA to a defocused image, we apply it to the corrupted *inverse-polar data*, which is obtained by inverse Fourier transforming the polar-grid data without interpolation. By interchanging the steps, the defocusing effect is one-dimensional, and thus we can obtain better estimates of the phase errors using the subspace-based technique. However, we must account for how the low-return region changes in the inverse-polar data. By using modified low-return constraints, this method, which we refer to as Reversed-step MultiChannel Autofocus (RMCA), gives near-perfect restoration in many cases. We give a complete and updated account of the preliminary work in [24].

The organization of the chapter is as follows. In Section 3.2, we study the performance of MCA as the range of look angles Θ becomes larger and the two-dimensional defocusing effect induced from the interpolation step becomes more severe. The conditions that make the performance poorer are discussed as well. The reversed-step reconstruction and the modified low-return constraints are studied in Section 3.3. For analytical purposes, we consider a continuous version of the inverse-polar domain and study point target responses. The analysis provides a guideline for determining the low-return constraint for the alternative reconstruction. In Section 3.4, simulation results are presented for different ranges of look angles and different choices of low-return constraints. Some practical issues also are discussed.

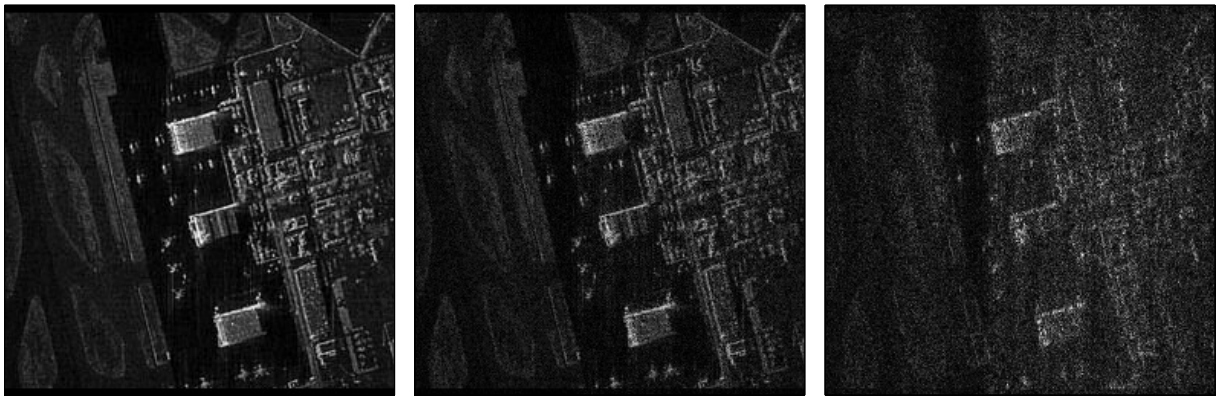

(a) Focused image, $\Theta = 0.1^o$ (b) MCA restoration, $\Theta = 0.1^o$ (c) MCA restoration, $\Theta = 1^o$

Figure 3.1: Performance of MCA as the polar data grid deviates from a Cartesian grid: (a) perfectly focused image, where the outermost 10 rows correspond to a zero-return region, (b) MCA restoration for $\Theta = 0.1^o$, and (c) MCA restoration for $\Theta = 1^o$. The defocused images corresponding to (b) and (c) were formed from the polar-grid data corrupted by a white phase error function.

3.2 Polar-Format Data and MCA

3.2.1 Defocusing Model for Polar-Format Data and MCA

MCA is based on the 1-D defocusing model described by (2.7), and essentially considers the demodulated Fourier data to lie on a Cartesian grid. In reality, the actual Fourier data lies on a polar grid and the phase errors are a 1-D function of the angular index as described in (2.6). The corrupted Cartesian-grid data are then described as

$$\tilde{G}_c[l',k'] = \sum_{l=1}^{N_\theta} \sum_{k=1}^{N_\rho} G_p[l,k] \Psi_{PC}[l',k';l,k] \, \mathrm{e}^{j\phi[l]}, \tag{3.1}$$

and are not related to the uncorrupted data $G_c[l',k']$ by multiplicative 1-D phase errors. Although MCA is based on an erroneous model, the amount of deviation from the 1-D defocusing model has been assumed to be small when the polar data grid is nearly Cartesian, i.e. when the range of look angles Θ is small, so that the effect on the performance of MCA would be correspondingly small. However, the modeling error may grow very fast as the polar grid deviates from a Cartesian grid, and so the performance of MCA can be much poorer than expected.

Fig. 3.1 illustrates how the performance of MCA may change as the range of look angles changes, i.e. as the polar grid deviates from a Cartesian grid. For this simulation, a SAR image from Sandia National Laboratories [25] was used to model the magnitude of the reflectivity, and the spatial phases were driven from an i.i.d. uniform random distribution with range $-\pi$ to π. To provide an ideal low-return region for MCA, the antenna footprint $w(x,y)$ was modeled by a

rect function. The SAR data are computed from the attenuated reflectivity model and we reconstruct images from the synthetic data via PFA. The resulting perfectly-focused image is shown in Fig. 3.1(a), where the outermost 10 rows of the 256-by-256 image correspond to the zero-return region of the rect function. A white phase error function was used to model severe defocusing, and MCA was applied to the defocused images using the zero-return constraints. Fig. 3.1(b) and (c) show MCA restorations for $\Theta = 0.1^o$ and $\Theta = 1^o$, respectively. Although both ranges of look angles are very narrow and the polar data grids are nearly Cartesian, the restorations are not perfect, and the performance of MCA quickly starts to degrade as the range of angles gets wider. Note that if we had synthesized the demodulated data on a Cartesian grid instead, MCA would have perfectly restored the focused image.

3.2.2 Sensitivity to Departure from the 1-D Defocusing Assumption

In this section, we compare the dependence of the performance of MCA, on the departure from a 1-D phase error, with that of two other 1-D autofocus methods: PGA and minimum entropy autofocus.

We first provide a simulation result showing how the phase errors in the corrupted Cartesian-grid data deviate from a 1-D error model when the SAR data is collected on a polar grid. For this purpose, assume for now that we have full knowledge of the uncorrupted Cartesian grid data $\mathbf{G_c}$ and let $\boldsymbol{\phi}^*$ denote a 1-D phase error function that best approximates the 2-D phase error in $\tilde{\mathbf{G}}_\mathbf{c}$. Specifically, define

$$\boldsymbol{\phi}^* \triangleq \min_{\boldsymbol{\phi}} \sum_{l',k'} \left| G_c[l',k']\, \mathrm{e}^{j\phi[l']} - \tilde{G}_c[l',k'] \right|^2 . \tag{3.2}$$

With this definition, for each fixed l', the optimizer is $\phi^*[l'] = \angle\{\sum_{k'} \tilde{G}_c[l',k']\overline{G_c[l',k']}\}$, the angle between the two complex-valued data.[1] The deviation between the 2-D phase errors and the best 1-D error model is

$$\omega_\phi[l',k'] = \angle\left\{\tilde{G}_c[l',k']\right\} - \angle\left\{G_c[l',k']\, \mathrm{e}^{j\phi^*[l']}\right\}. \tag{3.3}$$

When the range of look angles is small and the phase errors are nearly one-dimensional, we expect the values of ω_ϕ to be small.

Due to the various factors that affect the deviation ω_ϕ, it is difficult to construct a simple model for the 2-D phase errors in $\tilde{G}_c$; the phase errors are not 1-D in any Cartesian coordinate, and even the magnitude of $\tilde{G}_c$ are different from those of G_c. However, we have observed that the phase errors can deviate considerably from a one-dimensional model, even for a relatively small

[1] Let $\mathbf{w}$ and $\mathbf{z}$ be vectors of equal length and $\psi \in \mathbb{R}$. Since $\|\mathbf{w}\mathrm{e}^{j\psi} - \mathbf{z}\|_2^2 = \|\mathbf{w}\|_2^2 + \|\mathbf{z}\|_2^2 - 2\mathrm{Re}\{\mathrm{e}^{j\psi}\langle\mathbf{w},\mathbf{z}\rangle\}$ and $\langle\mathbf{w},\mathbf{z}\rangle = |\langle\mathbf{w},\mathbf{z}\rangle|\mathrm{e}^{j\angle\langle\mathbf{w},\mathbf{z}\rangle}$, we have $\psi^* \triangleq \mathrm{argmin}_\psi \|\mathbf{w}\mathrm{e}^{j\psi} - \mathbf{z}\|_2^2 = \mathrm{argmax}_\psi \mathrm{Re}\{\mathrm{e}^{j(\psi+\angle\langle\mathbf{w},\mathbf{z}\rangle)}\} = \mathrm{argmax}_\psi \cos(\psi + \angle\langle\mathbf{w},\mathbf{z}\rangle) = -\angle\langle\mathbf{w},\mathbf{z}\rangle = \angle\langle\mathbf{z},\mathbf{w}\rangle$.

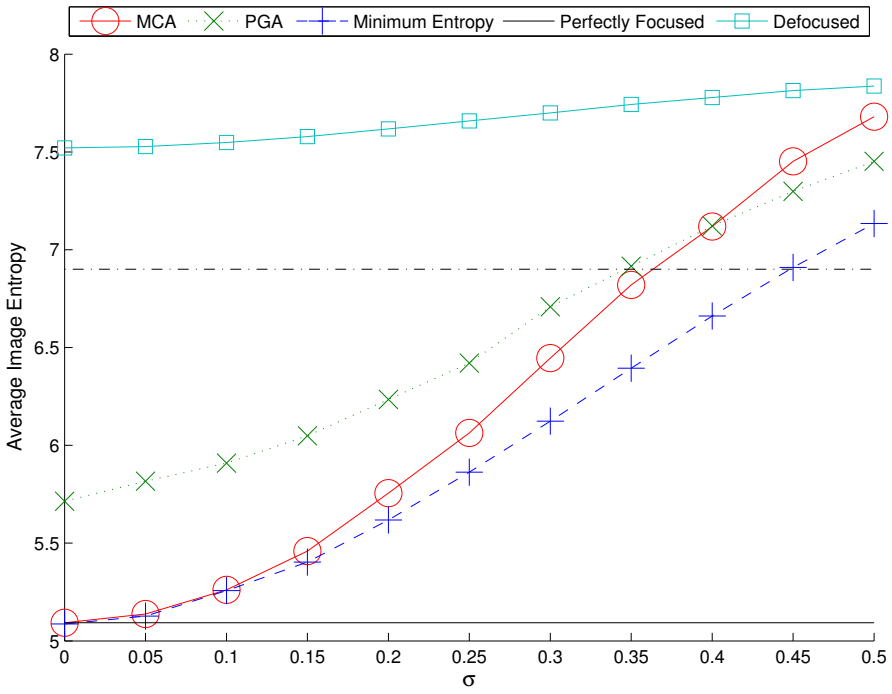

Figure 3.2: Performance of 1-D autofocus methods as a function of departure from a 1-D phase error. The performance is measured by image entropy averaged over 50 realizations, where large entropy corresponds to poor performance. σ represents the amount of deviation from a 1-D phase error assumption.

range of look angles when the phase errors are highly uncorrelated. To study the effect of the 2-D phase error function on the performance of MCA, we use our observation and assume a simple perturbation model

$$\tilde{G}_c[l',k'] = G_c[l',k']\,\mathrm{e}^{j(\phi_{1D}[l']+\omega_{2D}[l',k'])}, \tag{3.4}$$

where ϕ_{1D} is modeled as a white phase error function on the range $[-\pi,\pi)$, and ω_{2D} is modeled by an i.i.d. uniform random distribution ranging from $-\sigma\pi$ to $\sigma\pi$, where $\sigma \in [0,1]$ is used as a measure of deviation from the 1-D defocusing assumption. That is, $\sigma = 0$ represents the case where SAR data are collected on a Cartesian grid. The case with data collected on a polar grid and a wide range of look angles is crudely modeled with a large σ.

Figure 3.2 shows simulation results of the performance of three autofocus algorithms versus the deviation from a 1-D phase error model. A 64-by-64 image consisting of 64 point reflectors at random locations on a random clutter background was used as the model for a SAR scene, and the outermost 10 rows of the image were set to zero to provide an ideal low-return constraint for MCA. As a measure of performance, the image entropies of the restored images were averaged over 50 realizations of the phase errors, locations of the point reflectors, and the random clutter background. The circles, x's, and crosses in Fig. 3.2 correspond to the entropy of MCA, PGA, and minimum entropy autofocus restorations, respectively. The solid line and the squares correspond to

the entropy of the perfectly-focused and defocused images, respectively. Furthermore, the dotted line represents the maximum entropy value, corresponding to a well-focused image where all 64 point reflectors easily can be distinguished from the clutter. As expected, all three algorithms show degradation in performance as the amount of deviation σ becomes larger. Moreover, the figure shows that the different autofocus methods have different levels of sensitivity to the 1-D defocusing assumption; although MCA exhibits outstanding performance when the defocusing effect is truly one-dimensional, it degrades the most rapidly as σ becomes larger. A possible reason for the high sensitivity of MCA to the departure from the 1-D defocusing model is that individual singular vectors of a matrix may be unstable, i.e. small perturbations in data can result in a considerably different set of singular vectors [26].

Even if the phase errors in $\tilde{G}_c$ are truly one-dimensional, the error in the magnitude of $\tilde{G}_c$ may also affect the performance of MCA. The role of Fourier magnitude in image reconstruction is known to be much less important than that of the phase [27], and a similar observation has been made for SAR data [28]. However, an error at a single Fourier sample point affects the entire image [29] and uncorrelated errors in Fourier magnitude may introduce uncorrelated errors in the reconstructed image, resulting in loss of contrast [30]. Thus, the errors in the Fourier magnitude affect the region of low return, which is especially problematic when the contrast of the original scene is low, and resulting in the poor performance of MCA. Although not presented in this chapter, simulation results showed that the amount of magnitude error in the interpolated Fourier data is large when the phase errors are uncorrelated, and, as expected, the average energy in the presumed low-return region increased as the range of look angles became wider. However, the amount of degradation in the performance of MCA due to the magnitude errors was much smaller than that caused by the 2-D phase errors.

3.3 Reversed-step MCA

3.3.1 The Basic Idea

Because MCA suffers from inaccuracy of the 1-D phase assumption in the Cartesian domain, it is reasonable to try estimating the phase errors before applying polar-to-Cartesian interpolation. For a given polar data grid in the 2-D Fourier space, we define the *inverse-polar* data $\mathbf{g_p}$ of an image g_a as

$$g_p[m,n] = \sum_{l=1}^{N_\theta} \sum_{k=1}^{N_\rho} G_p[l,k]\, \mathrm{e}^{j2\pi\left(\frac{ml}{N_\theta}+\frac{nk}{N_\rho}\right)}, \tag{3.5}$$

where $\{\mathbf{G}_p\}$ is the Fourier transformation of g_a collected on a polar grid. We call the space of inverse-polar data the *inverse-polar* domain. (Note that we use this more accurate terminology

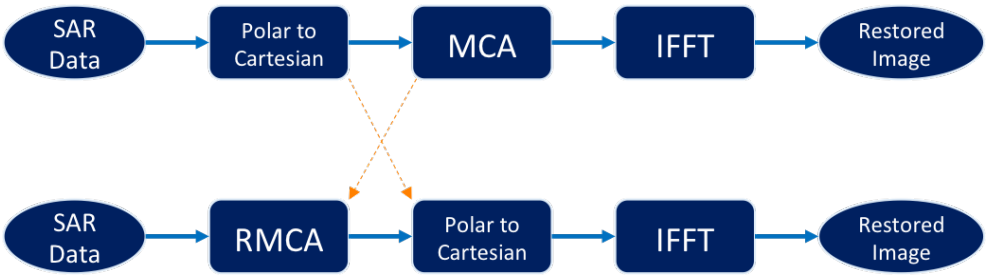

Figure 3.3: Comparison of MCA and RMCA approaches. The interpolation and autofocus steps are in reverse order.

rather than "warped-domain data" and "warped domain" as in our preliminary work [23].)

Clearly, the inverse-polar data are corrupted by a 1-D blurring kernel, regardless of the range of look angles. Because the inverse-polar data truly follows the defocusing model that MCA assumes, we can expect better performance in estimating the blurring kernel so long as we can identify an appropriate low-return region in the inverse-polar domain. Then, using the phase estimates obtained from applying MCA to the inverse-polar data, we can correct the errors in $\{\tilde{\mathbf{G}}_p\}$ and obtain the autofocused image by the usual PFA (polar-to-Cartesian interpolation followed by a 2-D Fast Fourier Transform (FFT)). We call our method Reversed-step MCA since the order of interpolation and autofocus are reversed, as shown in Fig. 3.3.

3.3.2 Impulse Response in the Inverse-Polar Domain

Since a low-return region is naturally provided by the antenna footprint in practice, the low-return constraints for MCA are straightforward to choose. The low-return region in the inverse-polar domain also depends on the shape of the antenna footprint, but in a less straightforward way. To gain insight into what the inverse-polar data might look like, we derive impulse responses for a continuous-version of the inverse-polar domain. Although we make assumptions in deriving the formula, for the tractability of our analysis, the result will help us understand where the low-return regions are in the inverse-polar domain.

Instead of having a discrete set of Fourier samples $\{G_p[l,k]\}$, assume that we have access to the Fourier data $G(f_R\cos\theta, f_R\sin\theta) = G_p(f_R,\theta)$ for $f_R \in [f_0-\Delta_f/2, f_0+\Delta_f/2]$ and $\theta \in [-\Theta/2, \Theta/2]$. Consequently, the coordinates form a wedge shape in the 2-D spatial-frequency domain. For this fixed range of coordinates, the continuous inverse-polar data $g_p(x_p,y_p)$ can be defined as:

$$g_p(x_p,y_p) \triangleq \int_{-\Theta/2}^{\Theta/2}\int_{f_0-\Delta_f/2}^{f_0+\Delta_f/2} G_p(f_R,\theta)\, \mathrm{e}^{j2\pi(x_p f_R + f_0 y_p \theta)} df_R\, d\theta. \tag{3.6}$$

Now, suppose we have an impulse at location $(r_0\cos\theta_0, r_0\sin\theta_0)$ in the spatial domain, where

we assume that $r_0 > 0$. (The impulse response of a target at the origin is straightforward.) Then, the inverse-polar data corresponding to the impulse is

$$h_p(x_p, y_p) = \int_{-\Theta/2}^{\Theta/2} \int_{f_0-\Delta_f/2}^{f_0+\Delta_f/2} \mathrm{e}^{-j2\pi r_0 f_R \cos(\theta_0-\theta)} \mathrm{e}^{j2\pi(x_p f_R + f_0 y_p \theta)} df_R \, d\theta \tag{3.7}$$

$$= \Delta_f \mathrm{e}^{j2\pi f_0 x_p} \int_{-\Theta/2}^{\Theta/2} A(x_p, \theta) \, \mathrm{e}^{-j\omega(y_p,\theta)} d\theta \tag{3.8}$$

where $A(x_p, \theta) = \mathrm{sinc}\left[\Delta_f \left\{x_p - r_0 \cos(\theta_0 - \theta)\right\}\right]$ and $\omega(y_p, \theta) = 2\pi f_0 \left\{r_0 \cos(\theta_0 - \theta) - y_p \theta\right\}$. The explicit formula for h_p is difficult to derive, but we can proceed acknowledging that the center frequency, f_0, is high in practice. It follows that ω is rapidly varying as a function of θ, whereas A is relatively slowly varying. By the principle of stationary phase, $|h_p|$ will have relatively large values if stationary phase is realized within the range of integration [31]. For a fixed y-coordinate y_p, stationary phase is realized at $\theta^*(y_p) = \theta_0 - \arcsin\left(y_p / r_0\right)$. If $\theta^*(y_p) \in [-\frac{\Theta}{2}, \frac{\Theta}{2}]$, i.e. if $y_p \in \left\{r_0 \sin(\theta_0 - \theta) : \theta \in [-\frac{\Theta}{2}, \frac{\Theta}{2}]\right\}$, then (3.7) can be approximated as

$$h_p(x_p, y_p) \approx \frac{\Delta_f A(x_p, \theta^*(y_p)) \mathrm{e}^{i\{2\pi f_0 x_p - \omega(y_p, \theta^*(y_p))\}}}{\sqrt{-j f_0 r_0 \cos\left\{\theta_0 - \theta^*(y_p)\right\}}} \tag{3.9}$$

by using a second-order Taylor-series expansion of ω about the stationary point. From the approximation, we can see that $|h_p|$ will have large values near x-coordinate $x_p = r_0 \cos\{\theta_0 - \theta^*(y_p)\}$ for a fixed y_p. Having assumed that the stationary phase point is within the range of integration, the impulse response in the inverse-polar domain will have large values near an arc described by $(r_0 \cos\theta, r_0 \sin\theta)$, $\theta \in [\theta_0 - \frac{\Theta}{2}, \theta_0 + \frac{\Theta}{2}]$. Note that the arc becomes longer as the range of look angles and distance of the point target from the center of scene get larger.

Fig. 3.4 shows simulated inverse-polar data for a scene consisting of 25 point reflectors of equal reflectivity and equal spacing in both directions. The simulation results agree with the above analysis, which was done for the continuous-version of the inverse-polar domain, showing impulse responses having arc-like features. Also, the sharp responses are smoothed as the range of look angles becomes wider and as the distance from the origin of the scene increases, as suggested by the analysis.

3.3.3 Low-Return Constraints for RMCA

The direction of arcs for the impulse responses suggests a region of low return in the inverse-polar domain. For circular or rectangular antenna patterns, the outermost corners of the inverse-polar domain are likely to have low returns, as shown in Fig. 3.5. Since the Fourier data lies on an

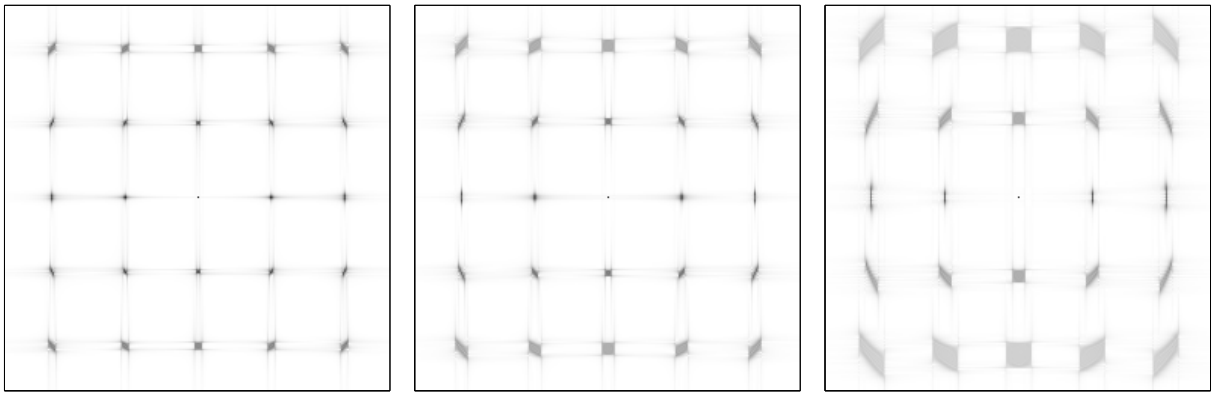

(a) $\Theta = 3^o$ (b) $\Theta = 5^o$ (c) $\Theta = 10^o$

Figure 3.4: Inverse-polar data corresponding to a scene consisting of 25 point reflectors for different ranges of look angles. Amplitude is plotted on a logarithmic scale.

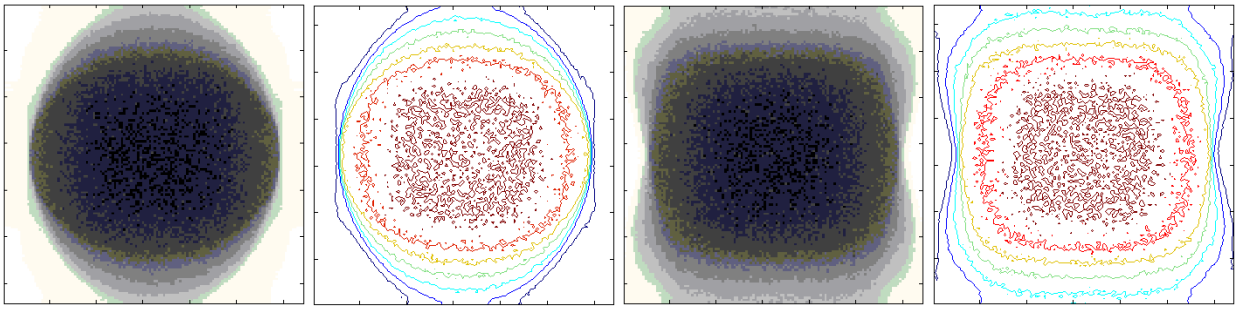

(a) g_p of a circle (b) Contours for (a) (c) g_p of a square (d) Contours of (c)

Figure 3.5: Inverse-polar data corresponding to different antenna patterns for $\Theta = 30°$: (a) inverse-polar data corresponding to a circular antenna footprint, (b) contours of (a), (c) inverse-polar data corresponding to a rectangular antenna footprint, and (d) contours of (c).

offset polar grid, we apply random spatial phases to model the complex reflectivity so that we can properly reconstruct the image [28]. The inverse-polar data is noisy due to the random phases applied; thus, here we have presented the average of the inverse-polar data over 100 realizations of random spatial phases. For larger Θ, additional simulations showed that the shape of the contours deviates more from the circular or rectangular shape and the low-return regions at the corners become narrower in the horizontal direction.

When the low returns are not exactly zero or when the transition from the low-return region to the non-low-return region is smooth, the solution of MCA highly depends on the set of low-return constraints, even when the Fourier data is acquired on a Cartesian grid. Unfortunately, the inverse-polar data do not contain zero-valued pixels in practice, and the transition from the low-return region to the non-low-return region becomes smoother as the range of look angles becomes wider. Thus, the RMCA solution often is not accurate enough if the low return region is estimated

based only on knowledge of the antenna pattern. Moreover, bright reflectors could be located in the highly-attenuated region of the scene and so the assumed low-return region might contain a few high values. A simple way of overcoming this issue is to apply RMCA with several sets of low-return constraints chosen randomly within the assumed low-return region [32]. Typically, the number of exceedingly bright reflectors is small and we can obtain a well-focused image using only a small number of trials.

3.4 Simulation Results

3.4.1 Simulation with 2-D Separable Sinc Antenna Footprint

Figure 3.6(a) shows a realistic SAR scene, which was obtained by applying an antenna pattern to a SAR image made available by Sandia National Laboratories [25]. A 2-D separable sinc function was used to model the attenuation by the antenna, where the main lobe of each sinc function covered half the width of the scene. The white square in the figure inscribes the main lobe of the sinc, and later will be used as the borderline of a reduced Field Of View (FOV) for the restored images. To model complex-valued reflectivities, spatial phases were driven independently from a uniform distribution ranging from $-\pi$ to π and applied to the image. SAR data were then synthesized on a polar grid in the Fourier domain. Furthermore, a white phase error function was applied in the angular direction to the polar-format data to model a severe defocusing effect. We used PFA for SAR image formation, with the resolution and FOV being equal to that of the scene shown in Fig. 3.6(a). Figure 3.6(b) shows a defocused image for $\Theta = 0.1^o$, along with the square indicating the reduced FOV. Although we formed an image with a wide FOV as in this figure, henceforth we will show only the region within the reduced FOV, since we generally are interested in imaging only the region that is strongly illuminated by the antenna. Forming an image of a larger size than will be viewed and later truncating it provides a better set of low return constraints for MCA. Figure 3.6(c) shows a perfectly focused image formed in this manner from uncorrupted (no phase error) SAR data with $\Theta = 0.1^o$.

The low-return constraints for MCA were specified in a straightforward manner by selecting pixels corresponding to the lowest values of the antenna footprint. We applied MCA to the defocused image several times for different numbers of constraints. In this set of simulations, the number of low-return constraints was linearly increased from the number of cross-range indices in the defocused image to 24 times that minimum number. Among the restored images, the one with the lowest entropy measure was selected as the "best" MCA restoration. The cross-hatched region in Fig. 3.6(d) shows the presumed low-return region that yielded the "best" MCA restoration for $\Theta = 0.1^o$. Figure 3.6(e) shows the MCA restoration with the lowest entropy measure for $\Theta = 0.1^o$.

(a) SAR scene

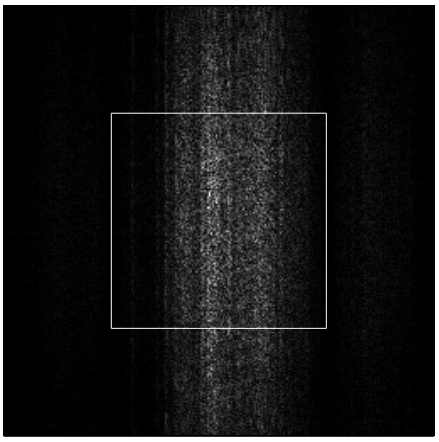

(b) Defocused image for $\Theta = 0.1^o$

(c) Perfectly-focused image for $\Theta = 0.1^o$

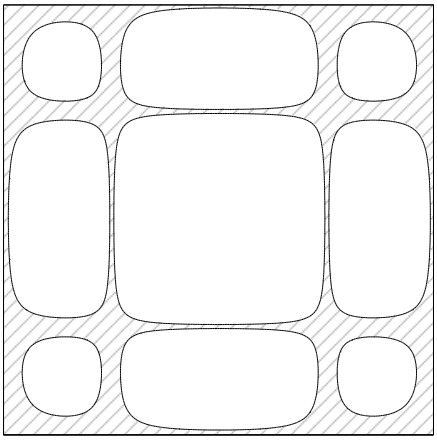

(d) Low-return region in spatial domain

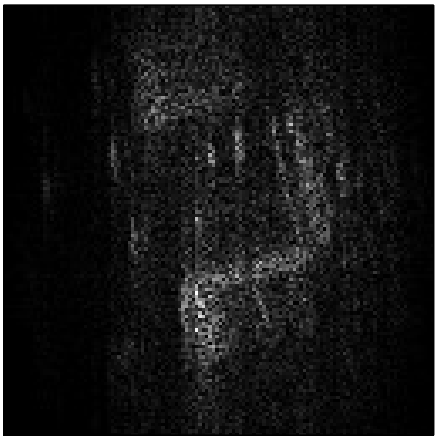

(e) MCA restoration for $\Theta = 0.1^o$

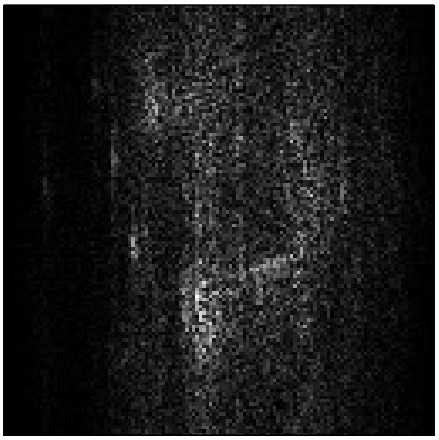

(f) MCA restoration for $\Theta = 1^o$

Figure 3.6: A realistic simulation of SAR imaging and MCA. (a) SAR scene modeled by a 256-by-256 image with a 2-D separable sinc window applied, (b) image defocused by a white phase error function, (c) perfectly-focused image of size 128-by-128, formed in the absence of phase errors, (d) low-return region presumed in use of MCA for $\Theta = 0.1^o$, (e) MCA restoration for $\Theta = 0.1^o$, and (f) MCA restoration for $\Theta = 1^o$. The squares in (a) and (b) indicate the reduced FOV corresponding to the region of interest. Entropy of the images: (b) 8.6948 (within the reduced FOV), (c) 7.6028, (e) 8.2562, and (f) 8.5056. The number of low-return constraints for MCA: (e) 5376, and (f) 2048.

MCA works to some extent in this challenging scenario and we can see some features in this image; however, it is not nearly as sharp as the perfectly-focused image even though the polar data grid is nearly Cartesian. As discussed earlier, the restoration quality of MCA drastically decreases as the range of look angles becomes wider. This is illustrated in Fig. 3.6(f) where the MCA restoration for $\Theta = 1^o$ is poorly focused even though the data collection angle is still narrow. The performance of MCA becomes even worse as the angle Θ gets wider. Restorations for Θ larger than about 3^o are not distinguishable from the defocused image.

To specify the low-return region for RMCA, attenuation windows corresponding to the antenna pattern were computed in the inverse-polar domain as described in Sec. 3.3.3. Here, we averaged 50 inverse-polar data sets corresponding to different realizations of random spatial phases. The low-return constraints were chosen based on the inverse-polar domain attenuation window for different numbers of constraints, ranging from the number of angular samples to 24 times the minimum number. Again, RMCA was applied multiple times, and the image with the lowest entropy measure was selected as the "best" RMCA restoration. Some simulation results for RMCA are shown in Fig. 3.7. The contours of the inverse-polar domain attenuation windows are shown in Figs. 3.7(a), (c), and (e) for $\Theta = 0.1^o$, $\Theta = 1^o$, and $\Theta = 5^o$, respectively. They each show contours of the antenna footprint at three levels, each corresponding to different sets of low-return constraints; the three levels of the contours are the thresholds corresponding to the low-return constraints of 1) the smallest size, 2) the "best" RMCA restoration, and 3) the largest size simulated. For a very narrow angle of $\Theta = 0.1^o$, the shapes of the low-return regions in the inverse-polar domain are very close to those in the spatial domain. Accordingly, the low-return constraints for RMCA remain similar to the spatial-domain low-return constraints for MCA, yet, RMCA performs much better than MCA and produces a nearly perfect image, as shown in Fig. 3.7(b). The improvement in the restoration quality is due to applying autofocus in the inverse-polar domain where the defocus truly is 1-D. As the range of look angles becomes wider, the inverse-polar domain attenuation windows become less similar to a 2-D separable sinc function. The shape of the low-return region changes, and furthermore, the low-return pixel values of the attenuation windows becomes higher. Consequently, RMCA restorations are less focused for larger values of Θ, although the degradation in RMCA performance is not nearly so severe as for MCA. Figure 3.7(d) and (f) show the corresponding RMCA restorations. The restorations show degradation in focus, but, the restoration for $\Theta = 5^o$ still clearly shows most of the details in the scene. RMCA successfully restores reasonably well-focused images even for fairly wide angles of $10 \sim 20$ degrees, and the extremely challenging white phase error used in these simulations.

Figure 3.8 shows how the performance of the multichannel autofocus algorithms relates to the range of look angles and the number of low-return constraints. The x's and crosses represent MCA for $\Theta = 0.1^o$ and $\Theta = 1^o$, respectively, and the dots, stars, and pentagrams represent RMCA

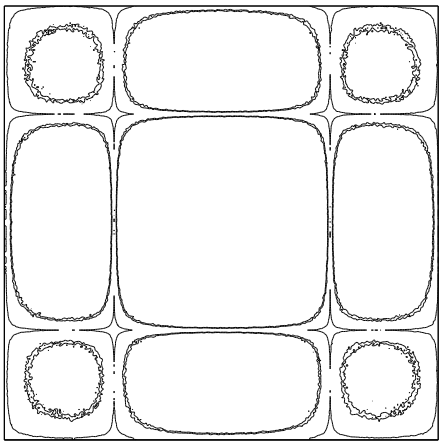

(a) Contours of the window, $\Theta = 0.1^o$

(b) RMCA restoration for $\Theta = 0.1^o$

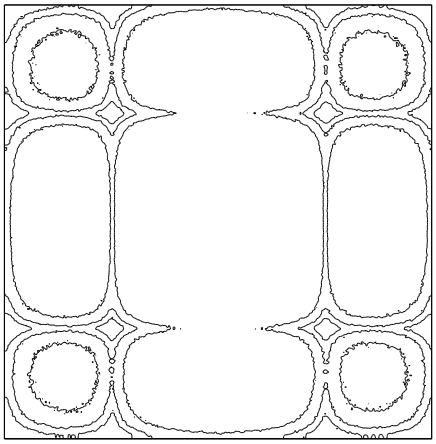

(c) Contours of the window, $\Theta = 1^o$

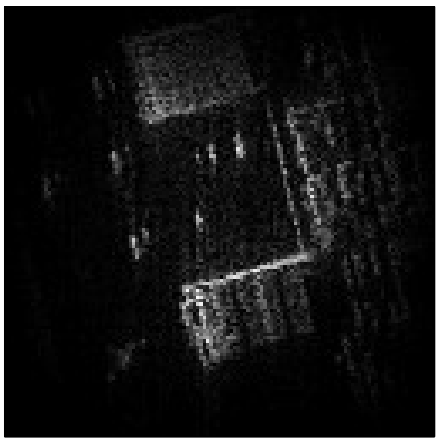

(d) RMCA restoration for $\Theta = 1^o$

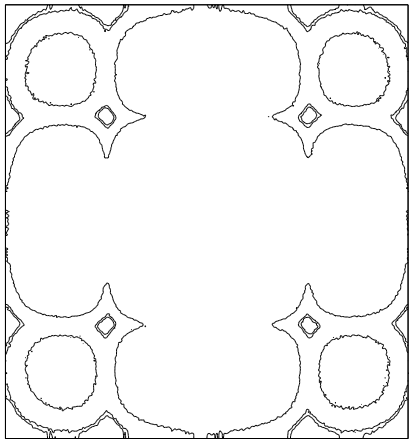

(e) Contours of the window, $\Theta = 5^o$

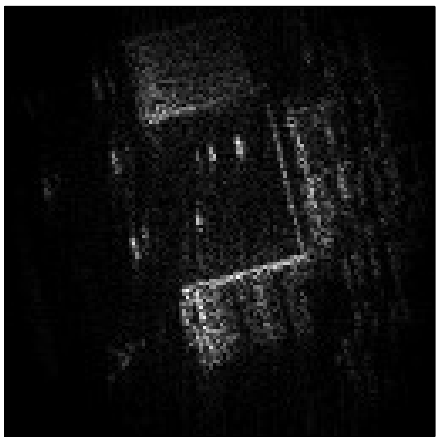

(f) RMCA restoration for $\Theta = 5^o$

Figure 3.7: A simulation of RMCA. (a), (c), and (e) show contours of the inverse-polar domain attenuation window. The three contour levels of each figure correspond to three different sets of low-return constraints for RMCA. (b), (d), (f) are RMCA restorations with the lowest entropy measure. Entropy of the images: (b) 7.5708, (d) 7.5914, and (f) 7.6335. The number of low-return constraints for RMCA restorations: (b) 5160, (d) 1572, and (f) 840.

for $\Theta = 0.1^o$, $\Theta = 1^o$, and $\Theta = 5^o$, respectively. Among the different set of constraints, the ones corresponding to the lowest image entropy are marked with circles for each set of simulations. Figure 3.8(a) shows image entropies as a function of the number of low-return constraints, where the image corresponding to (number of constraints) = 0 is the defocused image. The performance shows clear degradation as the range of look angles becomes wider, yet the correlation between the performance and the number of constraints is not obvious from the plot. Regardless of the number of the constraints, MCA is not effective for either angle and RMCA shows excellent performance for $\Theta = 0.1^o$. However, for a wider range of look angles, RMCA needs a proper number of low-return constraints to achieve good performance. In general, the performance of RMCA tends to improve as the number of constraints increases from zero, and the number of constraints needs to exceed the number of phase errors to achieve best performance. However, a larger number of constraints is not always beneficial.

Normalized Root-Mean-Squared Error (NRMSE) also can be a good indicator of performance in simulations, although we cannot compute NRMSE in real situations because we do not have knowledge of the perfectly focused image. Figure 3.8(b) presents NRMSE for the restored images, where the behavior of the performance measured by NRMSE is similar to the one measured by entropy. The restorations corresponding to the smallest NRMSE are marked with squares in Fig. 3.8(b). Although entropy and NRMSE are both good measures of performance, the restorations with the smallest entropy measure does not always have the smallest NRMSE, and vise versa.

3.4.2 Remarks

Because we are considering the challenging case with an i.i.d. phase error, which can occur in practice, we have not presented autofocus examples in this chapter using the well-known PGA algorithm. For the i.i.d. phase error case, PGA generally does not produce properly focused images for typical data collection angles used in practice [33]. However, when only a small amount of turbulence causes moderate demodulation timing errors, or for low-frequency (long wavelength) radars, the phase errors can be fairly smooth and PGA can be a very good choice.

We presented simulation results and discussed the quality of multichannel autofocus restorations for an attenuation function modeled by a 2-D separable sinc. We also have produced simulation results for other antenna footprints. MCA and RMCA can be more effective in situations where the attenuation function has a steeper fall-off or where the attenuation function is weighted with a tapering function such as Hamming window to suppress the signal outside the mainlobe. The extreme case is when the attenuation is modeled by a rect function, in which case the performance could be nearly perfect, even for MCA when the range of look angles is small.

As we presented in [32], the geometry of the low-return region also infuences the performance.

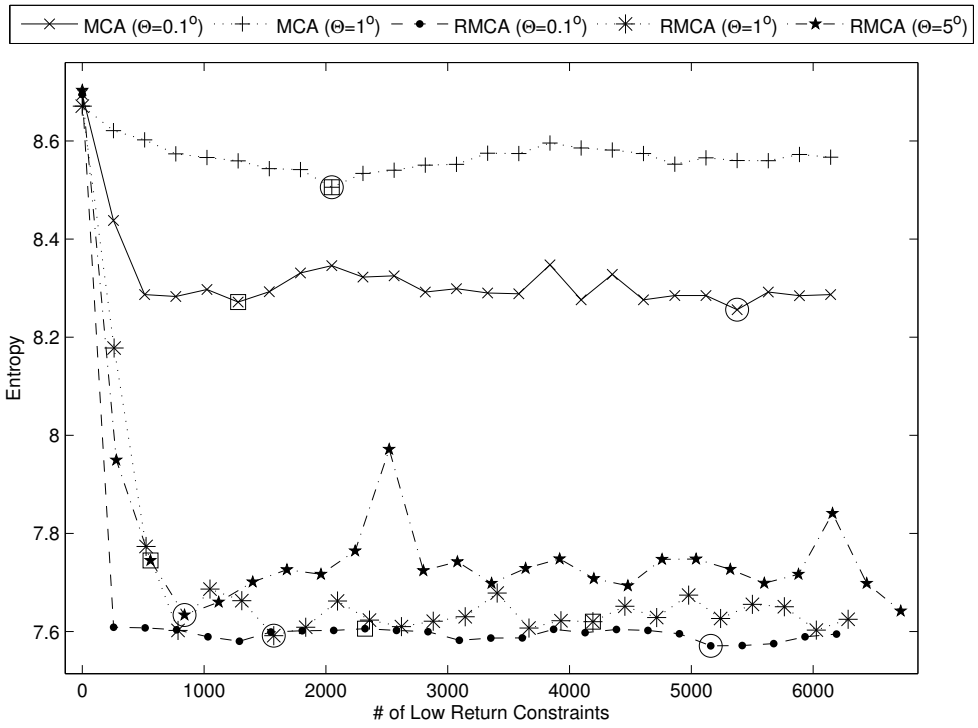

(a)

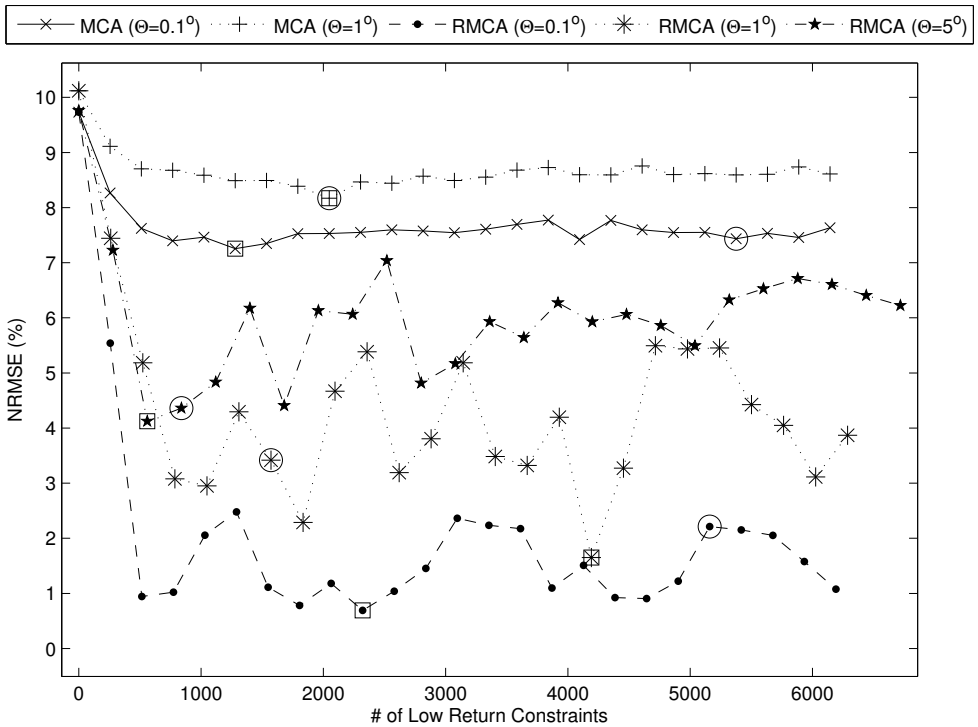

(b)

Figure 3.8: Performance of the multichannel autofocus algorithms for different numbers of low-return constraints. (a) and (b) show the entropy and the NRMSE (in percentage) of the restored images, respectively. Circles indicate the restorations with the lowest entropy measure and squares indicate the restorations with the smallest NRMSE for each set of simulations.

The effect of the geometry is not completely understood, but certain guidelines for choosing effective low-return constraints are intuitive. For example, zero-return columns in a perfectly-focused image (in the spatial domain for MCA, and in the inverse-polar domain for RMCA) are not useful at all as low-return constraints. This is because the corresponding columns in any image formed by filtering the defocused image with a 1-D kernel are zero-valued, and trying to minimize the energy in such a region is useless. Although zero-return columns are not likely to be encountered, there are columns of low returns in some realistic attenuation windows, and they may be ineffective by a similar argument.

The sampling intervals of the Fourier data also affect the performance. When using PFA to form images, we resampled onto a dense Cartesian grid so that the FOV of the formed image is larger than the scene of interest. This was to provide more low-return pixels near the nulls of the sinc in the spatial domain, so that MCA could utilize the near-zero pixels as the low-return constraints. Since the performance of multichannel autofocus algorithms strongly depend on the level of the low-return region, over-sampling in the Fourier domain is a key to achieving better performance. Similarly, the sampling intervals of the polar data grid should be dense enough to provide a decent set of low-return pixels in the inverse-polar domain. In our simulations, the polar-grid sampling intervals were chosen so that the maximum range and cross-range distances between the samples do not exceed the range and cross-range sampling intervals of the over-sampled Cartesian grid, respectively. However, the sampling rates were not optimized in any sense, and adequate sampling rates could differ for other antenna footprints. Thus, MCA and RMCA could achieve better performance than presented here if we had used denser Fourier data grids, and more importantly, they will not achieve the quality as discussed if the Fourier grids are not sufficiently dense.

The reader might assume that a wider range of look angles in our simulations corresponds to more angular samples and higher-resolution images; however, this is not the case. Rather than fixing the radar center frequency for all simulations, the center frequency was changed for different ranges of look angles so that the amount of Fourier coverage remained almost the same. The resolution of restored images and the sizes of the Fourier region covered by the Cartesian grids were fixed for all ranges of look angles, and the polar data grids were chosen so that they inscribed the Cartesian grids. Thus, the polar grid with a small range of look angles was located further away from the origin in Fourier space. We used this formulation for our simulations to avoid possibly misleading results; if the center frequency was fixed instead of the resolution, restorations for wider range of look angles would have had higher resolution and it would have been difficult to fairly compare the performances of MCA and RMCA for various angles.

As mentioned earlier, the performance of RMCA degrades as the range of look angles gets wider. Another recently developed multichannel autofocus algorithm, termed Fourier-domain MultiChannel Autofocus (FMCA) [33] can be applied to a wider range of look angles than RMCA.

However, FMCA also shows some degradation in performance as the angle becomes wider, since the polar-to-Cartesian interpolation used in the implementation induces more error as the spacing on the polar grid becomes more nonuniform. The performance of RMCA and FMCA are comparable for fairly small ranges of look angles, but the computational cost for FMCA is much higher because of the need for sophisticated interpolation required to estimate the blurring kernel.

CHAPTER 4

Using Multiple Low-Return Constraints for MCA

4.1 Introduction

SAR is widely used to acquire microwave images with both high cross-range and range resolution. In the tomographic formulation of spotlight-mode SAR, the post-processed data are the Fourier transform of the underlying reflectivity, sampled on a polar grid [1]. Thus, in principle, the original image can be reconstructed by applying an inverse Fourier transform. In practice, the Fourier data often are contaminated with unknown phase shifts due to demodulation timing errors, which cause the resulting image to be improperly focused.

In extensive literature on the SAR defocusing problem [6] a number of well-motivated *auto-focus* algorithms have been proposed. However, many of these algorithms are iterative in nature and their theoretical justification is mostly heuristic. MCA algorithm, proposed in [22], is a non-iterative algorithm developed under two key assumptions: i) the 1-D defocusing assumption and ii) the low-return assumption. When these assumptions are satisfied, it was shown that MCA recovers a near-perfect solution. However, the 1-D defocusing model does not apply exactly in reality since the phase error is a function of the polar angular variable, rather than the Cartesian Fourier coordinate. It so happens that MCA is very sensitive to the departure from the 1-D assumption. Thus, a modified version of MCA, termed Reversed-step MCA (RMCA), was proposed in [23] to account for this sensitivity.

The low-return assumption refers to the region of low return in the perfectly focused data that results from the attenuation provided by the antenna pattern. The low-return region, along with the defocused data, defines a linear solution space for the phase error, and the performance of both MCA and RMCA depends highly on the choice of the low-return constraints. In practice, the scene-dependent nature of the low-return region may make it difficult or even impossible to accurately identify the low-return region, especially in the presence of strong reflectors in the antenna sidelobes. Furthermore, when the image pixel values exhibit a smooth transition from

[0]This chapter includes research conducted jointly with David C. Munson, Jr. [32].

high to low returns, the line of demarcation between the two regions may not be so obvious to draw.

Analytical or data-dependent estimation of the true low-return region seems difficult, so we consider a rather simple way to solve this problem. Although the presumed low-return region, based on the antenna pattern, may contain some pixels with significant magnitude, it is highly likely the presumed low-return region will have far lower magnitude than elsewhere. Thus, we assume that the true low-return region is a subset of a possibly oversized, presumed low-return region.

The organization of this chapter is as follows. In Sec. 4.2, we discuss the effect of anomalies in the low-return region on the performance of RMCA and suggest a random subregion approach. Then, we demonstrate this method through simulations in Sec. 4.3. We study the performance of RMCA for three different random geometries of the subregion and with different numbers of anomalies in the presumed low-return region.

4.2 Overcoming Anomalies in the Low-Return Region

4.2.1 Anomalies in the Presumed Low-Return Region and RMCA

The inverse-polar data satisfy a low-return assumption in practice, but the region of low returns must be carefully specified since the solution highly depends on the set of low-return indices Ω when the low-return values are not exactly zero. However, the low-return region only can be evaluated using the knowledge of the antenna pattern and the sampling grids in the Fourier domain. Since the actual low-return region also depends on the scene itself, the pre-specified low-return region may not be accurate enough to yield a well-focused image in the case where bright reflectors are located in a highly-attenuated region of the scene.

In the presence of anomalies in the low-return region, the inverse-polar data can be expressed as:

$$\mathbf{g_p} = \mathbf{g_{p_0}} + \mathbf{n_p}, \tag{4.1}$$

where $\mathbf{g_{p_0}}$ corresponds to a scene without any anomaly and $\mathbf{n_p}$ corresponds to a scene composed of anomalies. Then, the defocused inverse-polar data $\tilde{\mathbf{g}}_\mathbf{p}$ also can be expressed as a summation of the anomaly-free term $\tilde{\mathbf{g}}_{\mathbf{p}0}$ and $\tilde{\mathbf{n}}_\mathbf{p}$ that corresponds to the anomalies. Furthermore, the matrix $\mathbf{\Phi_\Omega}$ also can be expressed as a summation:

$$\mathbf{\Phi_\Omega} = \mathbf{\Phi_{\Omega 0}} + \mathbf{N_\Omega}, \tag{4.2}$$

where $\mathbf{\Phi_{\Omega 0}}$ and $\mathbf{N_\Omega}$ correspond to $\mathbf{g_{p0}}$ and $\mathbf{n_p}$, respectively. The RMCA solution $\hat{\mathbf{v}}$ is given by the

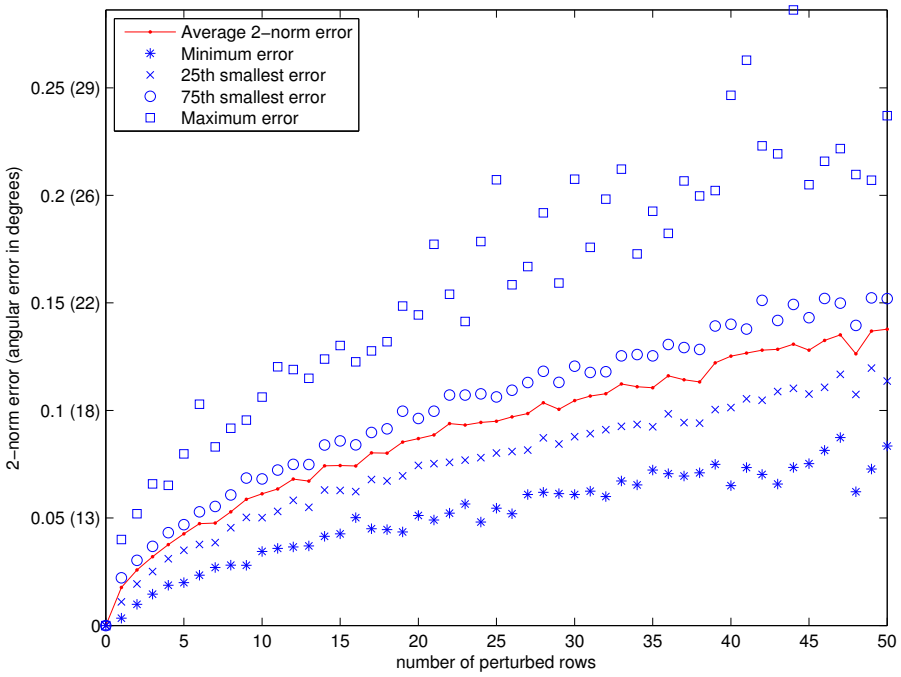

Figure 4.1: The amount of errors in the rightmost right singular vector of a perturbed matrix for different numbers of perturbed rows. A random complex-valued 100-by-40 matrix is perturbed by addition of random complex-valued rows. The 2-norm of the error in the rightmost right singular vector due to the perturbation is measured for 100 instances of perturbation rows. Several values of the angular error of the rightmost right singular vector are shown (in parenthesis) in the labels of the y-axis, next to the corresponding 2-norm errors.

rightmost right singular vector (right singular vector corresponding to the smallest singular value) of $\mathbf{\Phi}_{\mathbf{\Omega}0} + \mathbf{N}_{\mathbf{\Omega}}$, whereas a more desirable solution would be the right singular vector of $\hat{\mathbf{v}}_0$ of $\mathbf{\Phi}_{\mathbf{\Omega}0}$.

When the number of indices in Ω that are affected by the anomalies is small, $\mathbf{N}_{\mathbf{\Omega}}$ is a sparse matrix with most rows being zeros. In such case, we might expect that the singular vectors of $\mathbf{\Phi}_{\mathbf{\Omega}0} + \mathbf{N}_{\mathbf{\Omega}}$ and $\mathbf{\Phi}_{\mathbf{\Omega}0}$ would be similar. However, according to the perturbation theory of SVD, it is not guaranteed that a small perturbation in a matrix will correspond to a small perturbation in the singular vectors, and even more, the singular vectors can be very different [26].

Figure 4.1 shows a simulation result on the rightmost right singular vector of a matrix perturbed by a sparse matrix. In the simulation, a matrix $\mathbf{A} \in \mathbb{C}^{100\times 40}$ is randomly generated, where the real and imaginary parts of each entry are driven independently from a uniform distribution ranging from -0.5 to 0.5. Several rows of $\mathbf{A}$ are perturbed by addition of random row vectors. The real and imaginary parts of each entry of the added rows are driven independently from a uniform distribution ranging from -0.05 to 0.05. Then, the 2-norm of the error in the rightmost right singular vector due to the perturbation is measured for 100 random generations of the random rows. The red line in Fig. 4.1 shows the average of the 2-norm errors for different numbers of perturbed rows. The asterisks, crosses, circles, and squares correspond to the minimum, 25th

smallest, 75th smallest, and the maximum of the 2-norm errors over the 100 instances. Along with the 2-norm error, the corresponding angular error (in degrees) of the rightmost right singular vector is also shown in parenthesis in the labels of the y-axis. The angular error is the angle between the rightmost singular vector of the perturbed matrix and that of the unperturbed matrix, and is related to the 2-norm error ϵ by $\arccos(1-\epsilon/2)$.

As shown in Fig. 4.1, the 2-norm error increases as the number of perturbed rows increases. The error from an instance of perturbation is close to the average error in half the cases, which can be seen from the crosses and circles in the figure. However, the error can be much smaller (asterisks) than the average, and more importantly, much larger (squares) than the average. For example, when a moderately small number of 6 rows were perturbed, the maximum of the 2-norm errors was over 0.1, which corresponds to an angular error of 18^o. If the phase errors are estimated via RMCA from a vector suffering from such amount of errors, then the restored image would be improperly focused. Thus, it is important to avoid having multiple low-return constraints that correspond to anomalies in the highly attenuated region to achieve best performance of RMCA.

4.2.2 Random Subregion Approach

Since the actual low-return region depends somewhat on the scene, the presumed low-return region, Ω, provides only a superset of the most probable low-return pixels. Without further complicating the estimation process, we may apply RMCA to the same defocused data using several different random subsets of Ω as the low-return constraints. Then, given that the number and strength of anomalies in the presumed low-return region are small, it is possible to obtain a reasonably focused image within several trials, with high probability. Image focus quality can be evaluated by computing a sharpness measure, such as entropy, and we may choose the image with the highest sharpness measure.

The geometry of the low-return region is another factor that affects the performance of MCA. Extending the low-return region along the range direction introduces redundancies in the defocusing operator, while extending the region along the direction of blur forces the algorithm to reduce the mainlobe width of the blurring kernel. Thus, adding constraints that extend in both the range and cross-range directions may have a positive effect on the performance of the algorithm. Analytically solving for the best possible geometry of the low-return region is seemingly intractable. To get an idea of how different geometries affect RMCA performance, the next section provides simulation results for three different types of subregions: i) subregion consisting of randomly chosen pixels, ii) subregion consisting of randomly chosen vertical columns, and iii) subregion consisting of randomly chosen horizontal rows. Here, the horizontal coordinate represents the range dimension and the vertical coordinate represents cross-range.

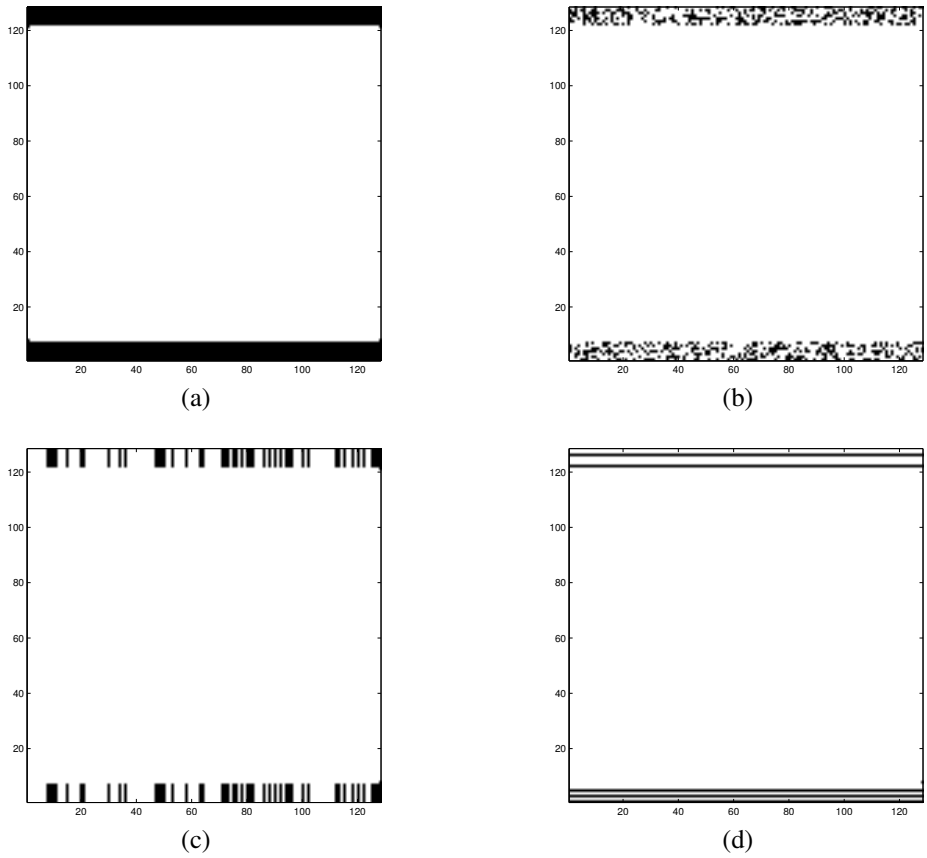

Figure 4.2: Example of a presumed low-return region and its random subregions in the inverse-polar domain for $\Theta = 3°$: (a) presumed low-return region, (b) i.i.d. random subregion, (c) random vertical subregion, and (d) random horizontal subregion.

Figure 4.2 shows an example of a presumed low-return region and three subregions with different geometries. The presumed low-return region depicted in Fig. 4.2(a) corresponds to an antenna pattern with uniform power and rectangular shape. The range of data-collection angles Θ is narrow, and the presumed low-return region in the inverse-polar domain resembles the antenna pattern in the spatial domain. Figures 4.2 (b), (c), and (d) are randomly chosen subregions of i.i.d. random, random vertical, and random horizontal geometries, respectively.

4.3 Simulation Results

4.3.1 Simulation of RMCA with random subregions

In this section, we present simulation results under a specific scenario, and then discuss generalization of the results. A SAR image from Sandia National Laboratories [25] was used to model the magnitude of the reflectivity, and the spatial phases were driven from an i.i.d. uniform distribution

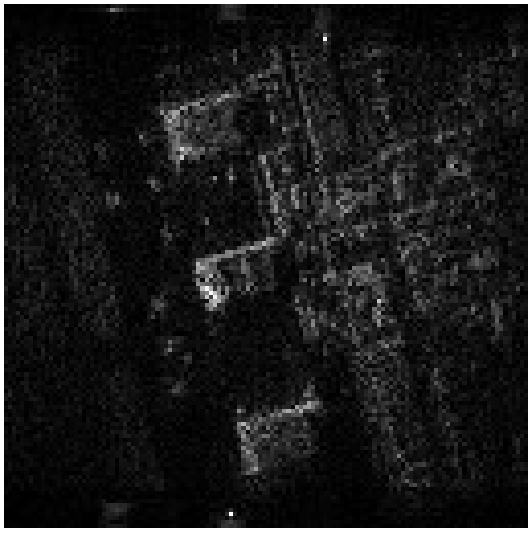

(a) Perfectly focused image

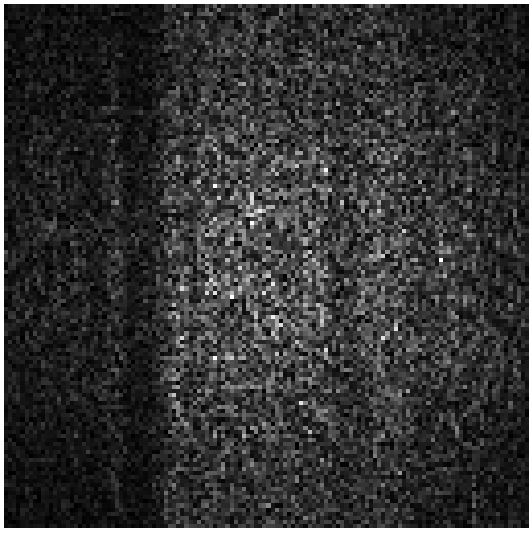

(b) Defocused image

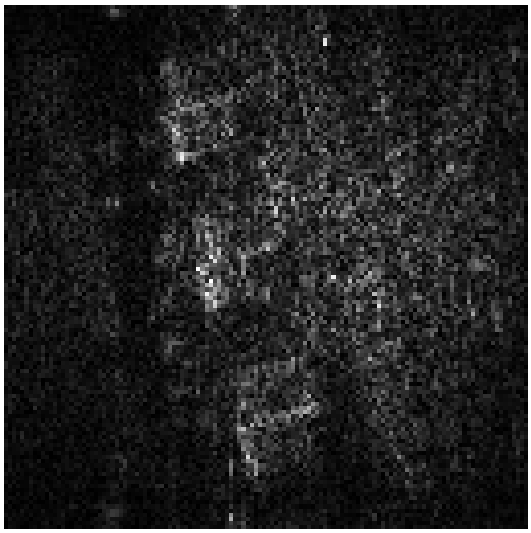

(c) RMCA restoration ♯1

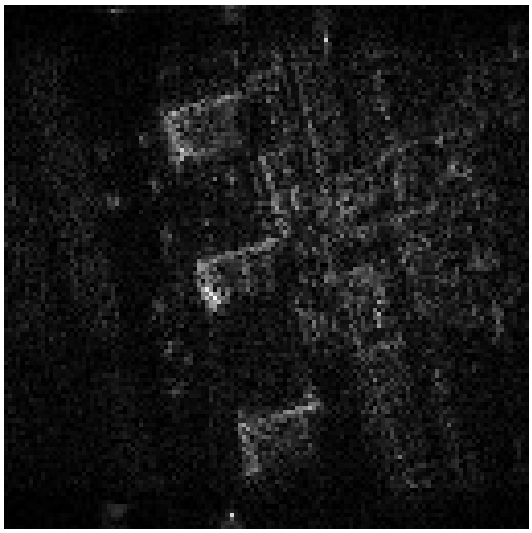

(d) RMCA restoration ♯2

Figure 4.3: Simulated SAR images for $\Theta = 3°$: (a) perfectly focused image with three anomalies in the zero-return rows, (b) defocused image, where a white phase-error function was applied, (c) RMCA restoration using the presumed low-return constraints, and (d) RMCA restoration using a randomly chosen subset of a larger set of presumed low-return constraints.

ranging from $-\pi$ to π. The reflectivity of the outermost 20 rows of the 128-by-128 image were set to zero, except for few anomalies. The magnitude of the anomalies were chosen to be three times larger than the maximum magnitude in the middle 108 rows. In practice, the relative magnitude of the anomalies is much lower in most situations. The Fourier data was synthesized on a polar-grid with a range of angles $\Theta = 3°$, and a white phase-error function was applied to model a severe defocusing effect. An example of a focused image is shown in Fig. 4.3(a), where three anomalies

are located in the presumed low-return region. Figure 4.3(b) shows the corresponding defocused image.

A presumed low-return region of a large size (1792 pixels) was identified, based on the antenna pattern and the Fourier data grid, and was used as the superset of the low-return constraints throughout the set of simulations. For each simulation of RMCA, we varied four parameters: i) the number of anomalies, ii) the location of anomalies, iii) the type of geometry of the subregion, and iv) the random constraints. For each number of anomalies, ranging from 0 to 10, we chose 50 different locations of the anomalies. Then for each of these 501 corrupted data sets, we applied RMCA with 50 different subregions (for each type of geometry discussed in Sec. 4.2.2) as the low-return constraints. Here, the size of the low-return constraints was chosen to be as close as possible to 640 pixels. Figures 4.3(c) and (d) both show images restored by RMCA from the same defocused data, Fig. 4.3(b), but with different low-return constraints. Figure 4.3(c) was obtained by using a presumed low-return region of size 640 as the constraints, and Fig. 4.3(d) was obtained by using a randomly chosen subset (of size 640) of a presumed low-return region of size 1792. Figure 4.3(d) had the fifth smallest entropy among the 50 restorations using different subregions of i.i.d. random geometry; it is neither the best nor the worst restoration obtainable by using the random-subregion approach.

Figure 4.4 shows three plots summarizing our simulation results. The plots show the average performance of RMCA as the number of anomalies get larger, where the performance is measured by the image entropy of the restored data. The connected circles in Figs. 4.4(a), (b), and (c) represent the averaged entropies of the restored images for i.i.d. random, random horizontal, and random vertical subregions, respectively. While all three types tend to show degradation in performance as the number of anomalies gets larger, several details should be noted.

First, close comparison of the three plots reveals that the average performance of i.i.d. random subregion is always between the average performance of the other two types. However, we believe that this behavior may be dependent on the scene and the geometry of the presumed low-return region. Second, except for the case where no anomaly exists, using the subregion approach with the random horizontal geometry shows the best average performance. Lastly, the random horizontal subregion shows poor performance when there is no anomaly at all. This may seem implausible at first sight, however, we offer a possible explanation at the end of this section.

The x's in the three plots represent the average entropies for fixed locations of anomalies, where only the minimum, maximum, the 33rd percentile, and the 67th percentile of the 50 locations are shown. The performance seems to be sensitive to the location of anomalies when there are only few of them, but is less affected by the location as the number of anomalies grows, as expected. Similarly, the dots represent the minimum, maximum, the 33rd percentile, and the 67th percentile of the average entropies corresponding to 50 different random subregions. For different random

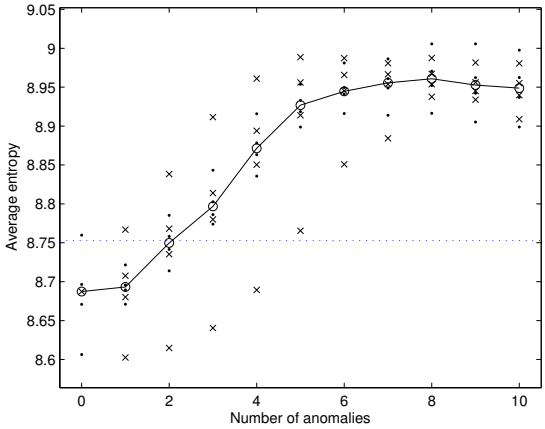

(a) i.i.d. random subregion

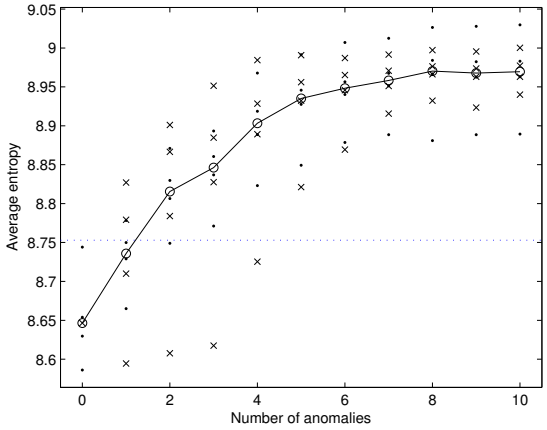

(b) Random vertical subregion

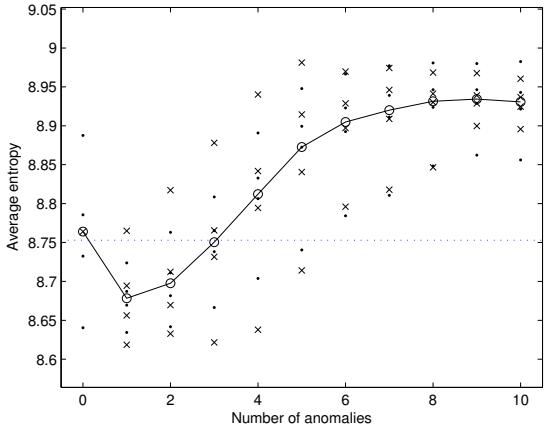

(c) Random horizontal subregion

Figure 4.4: Performance of RMCA using random-subregion constraints. The circles represent average entropies, and the x's and dots represent entropies corresponding to different locations of anomalies and different random low-return constraints, respectively.

subregions, the performance shows different level of sensitivity, where the i.i.d. random subregion shows the smallest range of deviation.

The horizontal dotted line in the three plots represents the average entropy corresponding to phase errors driven from a uniform distribution of zero mean and standard deviation equal to $\pi/6$. We consider restored images with entropy less than this value to be well focused. Using this as a criterion, Fig. 4.5 shows the percentage of image restorations that were well focused as a function of the number of anomalies. The circles, stars, and triangles correspond to i.i.d. random, random vertical, and random horizontal geometries, respectively. Notice that a modest number of restorations will, with high probability, produce one or more properly focused images. Furthermore, for a scenario where the anomalies are not so strong as those assumed in these simulations, the curves

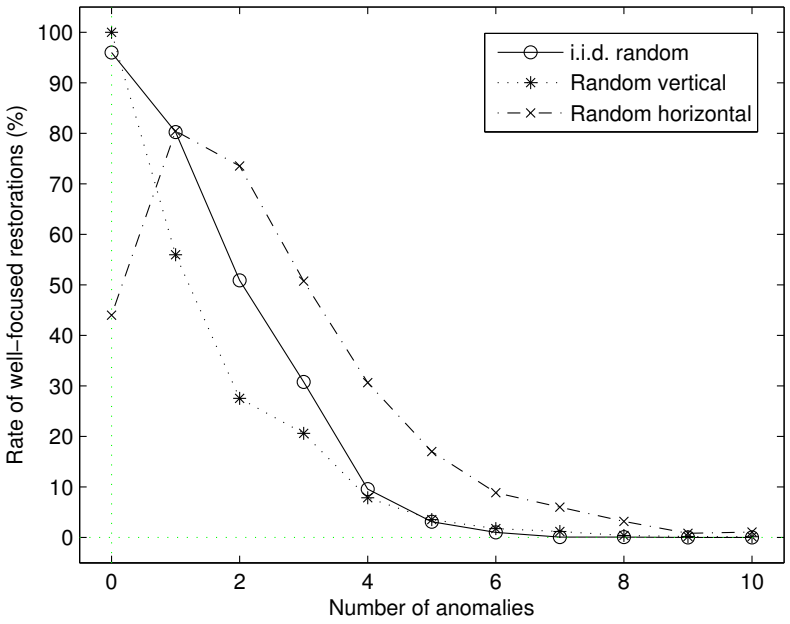

Figure 4.5: The percentage of RMCA restoring a well-focused image for different random subregions.

in Fig. 4.5 fall off far more slowly.

4.3.2 Remarks

Suppose RMCA is applied with the low-return constraints Ω_0, where $|\Omega_0| \geq N_\theta$. Let Ω_s denote the set of indices corresponding to the indices of Ω_0, circularly shifted by the amount s, i.e.,

$$\Omega_s = \Big\{(m,n) \in [1,\ldots,N_\theta] \times [1,\ldots,N_\rho] : ((m-s-1) \bmod N_\theta + 1, n) \in \Omega_0\Big\}, \tag{4.3}$$

for $s \in [1,\ldots,N_\theta - 1]$, where mod is the modulus operator. Let $\mathcal{S} = \{s \in [0,\ldots,N_\theta - 1] : g_p[m,n] = 0, \forall (m,n) \in \Omega_s\}$. Then, when $|\mathcal{S}| = 1$, RMCA restores the perfectly focused image, whether or not $0 \in \mathcal{S}$; that is, RMCA restores the perfectly focused image even when the low-return constraints are incorrect if there exists exactly one circularly-shifted version of the constraints that corresponds to zero returns. If $|\mathcal{S}| > 1$, then

$$\|\mathbf{\Phi}_{\Omega_0}\mathbf{v}\|_2 = 0, \quad \forall \mathbf{v} \in \{\mathbf{F}^*\mathbf{A}\mathbf{c} : \mathbf{c} \in \mathcal{C}\}, \tag{4.4}$$

where $\mathbf{A}$ is an $N_\theta \times |\mathcal{S}|$ matrix, composed of columns $\mathbf{e}^{-j\boldsymbol{\phi}_s} \in \mathbb{C}^{N_\theta \times 1}$, where $\phi_s[l] = \phi_l - 2\pi s l / N_\theta$. $\mathbf{F}$ is the 1-D DFT operator and $\mathcal{C} = \{\mathbf{c} \in \mathbb{C}^{|\mathcal{S}|\times 1} : \|\mathbf{A}\mathbf{c}\|_2 = 1\}$. In this case, any filter satisfying $\mathbf{v} = \mathbf{F}^*\mathbf{A}\mathbf{c}$ with $\mathbf{c} \in \mathcal{C}$ is a possible solution to the minimization problem (2.12), and it could be very different

from the true solution.

Therefore, the behavior in the performance of random horizontal geometry may be explained as follows. When no anomaly exists in the presumed low-return region, it is very probable that $|\mathcal{S}| > 1$ for random horizontal subregions. Thus, RMCA might show poor performance. On the other hand, as the number of anomalies increases, random horizontal geometry may show better performance compared to the other two types of random subregion since it is more probable that there is a nonzero s in $\mathcal{S}$ for the random horizontal geometry than for the other two.

CHAPTER 5

Elimination of Filtering in Filtered Back-Projection

5.1 Introduction

Using the tomographic formulation for spotlight-mode SAR, the demodulated data are samples of the Fourier transforms of projections across the underling scene [1]. For far-field imaging, the data furthermore can be interpreted as polar samples of the 2-D Fourier transform of the underlying image. The most popular means of image reconstruction is the Polar Reformatting Algorithm (PFA) [6], which forms the image by applying a 2-D FFT after resampling the data onto a Cartesian grid. An alternative reconstruction method under the tomographic paradigm is Filtered BackProjection (FBP) [2], where necessary modifications are made to FBP from medical imaging to accommodate the bandpass data available in SAR.

Although, historically, PFA has been preferred over conventional FBP, fast algorithms for FBP have been developed [3–5, 34], allowing the computational cost to be equivalent to that of PFA ($O(N^2 \log N)$) for an $N \times N$ scene. In some scenarios, FBP is preferred to PFA. For example, FBP can be more effective when 1) the polar-to-Cartesian interpolation in the Fourier domain is challenging, such as in wide-angle, bistatic, or multistatic SAR, 2) only a small portion of the image needs to be reconstructed, 3) imaging in the near-field, where the acquired data are no longer a 2-D Fourier transform of the scene, or 4) when back-projection is performed in parallel.

In near-field SAR imaging, the acquired data are Fourier transformations of projections along circular arcs, and the FBP algorithm easily can be modified to backproject along the corresponding curves [34]. However, there is no known exact filter for near-field FBP. So-called "optimal" filters must be derived under restrictive assumptions. Designing a good filter is a complicated process, and furthermore, a good filter will be spatially varying and therefore computationally complex. Thus, we wish to avoid filtering unless it offers a clear advantage in image quality. Fortunately, it has been thought that filtering is less important for SAR imaging than for medical imaging. This is because the ramp filter in FBP is roughly constant over the SAR data range in the Fourier domain. Although this observation holds only for far field, recently an image formation algorithm based on

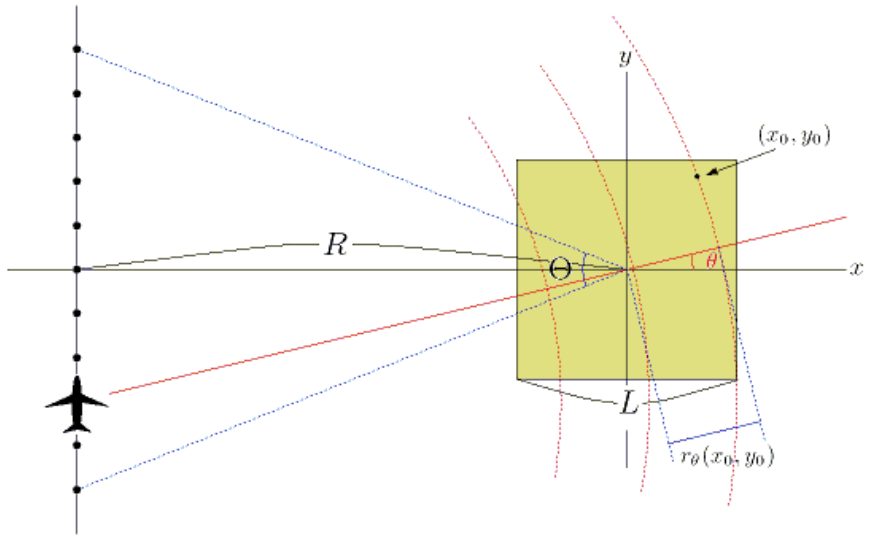

Figure 5.1: Data collection geometry of spotlight-mode SAR with circular wavefronts.

beamforming was developed and studied for the near-field [35] and bistatic [36] cases that is essentially the same as back-projecion without filtering. In this chapter, we examine this hypothesis, determining whether, why, and under what conditions, the filtering step can be eliminated.

The organization of this chapter is as follows. Section 5.2 introduces the imaging scenario we consider, the notation to be used, and the FBP algorithm. In Sec. 5.3, we present a simple simulation showing the difference in the importance of filtering for SAR imaging versus medical imaging. In Sec. 5.4, point target responses using FBP with and without filtering are analyzed for the far-field case, focusing on several image quality measures, as a function of the radar parameters. Section 5.5 studies the effect of filtering for the near-field case using simulations to show how filtering affects point target resolution.

5.2 Background

5.2.1 Tomographic Formulation of SAR Imaging

We consider spotlight-mode SAR and its tomographic formulation, where the geometry of the data collection process is depicted in Fig. 5.1. We assume zero depression angle, broadside collection, and a straight-line trajectory of the radar platform for simplicity. The radar transmits and collects pulses at points corresponding to look angles $\{\theta : |\theta| \leq \Theta/2\}$. We denote the range and cross-range coordinates as x and y, respectively, where the origin of the spatial coordinate system is set to be at the center of the ground patch we wish to image. The ground patch is of size L and the minimum

distance between the radar platform and the center of the image is denoted by R. The wavefronts are circular in general, but, they are assumed to be planar for far-field imaging, i.e. when $R \gg L$.

Let $g(x,y)$ denote the complex-valued reflectivity of the ground patch, and let p_θ be the projection of g along curves onto the line of sight at angle θ, i.e.,

$$p_\theta(u) = \int\int g(x,y)\,\delta\left(u - r_\theta(x,y)\right)\,dxdy, \tag{5.1}$$

where $r_\theta(x,y) = \{(x+R)^2 + (y+R\tan\theta)^2\}^{1/2} - R\sec\theta$. Note that $r_\theta(x,y)$ is replaced by $\bar{r}_\theta(x,y) = x\cos\theta + y\sin\theta$ under the far-field assumption.

In the tomographic formulation [1], the demodulated return from look angle θ can be expressed as

$$P_\theta\left(\frac{1}{c\pi}\{\omega_0 + 2\alpha(t - \frac{2R\sec\theta}{c})\}\right), \tag{5.2}$$

where P_θ is the Fourier transform of p_θ, c is the speed of light, and ω_0 and 2α are the center frequency and chirp rate of the transmitted linear FM pulse, respectively. Since the transmitted pulse has a limited duration T, $P_\theta(\rho)$ is available only within an interval of spatial frequencies denoted as $\left[\rho_0 - \frac{\Delta}{2}, \rho_0 + \frac{\Delta}{2}\right]$, where $\rho_0 = \omega_0/c\pi$ and $\Delta = 2\alpha T/c\pi$. That is, the demodulated data are Fourier transforms of the projected reflectivities, within limited angles and spatial frequencies.

5.2.2 FBP for Far-Field Imaging

When the wavefronts are assumed to be planar, the demodulated data are not only 1-D Fourier transformations of the line projections, but also slices of the 2-D Fourier transformation of the reflectivity, which follows from the projection-slice theorem [1]. While this has led to the popularity of PFA for SAR image reconstruction, the image also can be reconstructed by backprojecting onto the lines of projection, after filtering either in the spatial domain (convolution backprojection) or in the frequency domain (FBP). FBP reconstruction has been shown to be equivalent to PFA reconstruction when using a 2-D periodic sinc with Jacobian weighting as the polar-to-Cartesian interpolation kernel [37].

The FBP inversion formula is

$$\hat{g}_{\text{FF}}(x,y) = \int_{-\Theta/2}^{\Theta/2}\int_{\rho_0-\Delta/2}^{\rho_0+\Delta/2} |\rho|\,P_\theta(\rho)\,\mathrm{e}^{j2\pi\rho(x\cos\theta + y\sin\theta)}d\rho\,d\theta. \tag{5.3}$$

In practice, since we are given samples of the Fourier transformations only for an offset frequency range, i.e., band-pass data, accurate processing (including interpolation) is greatly simplified by first demodulating by the carrier frequency [2]. A conventional implementation of FBP is computationally more expensive ($O(N^3)$ for an N-by-N image) than PFA, but, as noted earlier, fast algo-

rithms have been developed that have a computational cost equivalent to that of PFA ($O(N^2 \log N)$).

5.2.3 Near-Field Imaging via Back-Projection

Fourier transformations of projections along curves cannot be interpreted in terms of the 2-D Fourier transformation of the reflectivity, and an image reconstructed via PFA will show distortion [38]. While traditional FBP also will not work properly for near-field imaging, backprojecting along curves (wavefronts), instead of lines, is an intuitively sensible approach. However, designing a good filter for near-field FBP is a complicated process, and there is no known filter that guarantees exact reconstruction. Perhaps the best known FBP formula for the near-field case was developed in [39], further studied in [40], and then extended to bistatic SAR in [41]. For the data collection geometry introduced in Sec. 5.2.1, the FBP formula can be written as follows[1]:

$$\hat{g}_{\text{NF}}(x,y;R) = \int_{-\Theta/2}^{\Theta/2} \frac{(x+R)R\sec^2\theta}{(x+R)^2+(y+R\tan\theta)^2} \int_{\rho_0-\Delta/2}^{\rho_0+\Delta/2} |\rho|\, P_\theta(\rho)\, \mathrm{e}^{j2\pi\rho\, r_\theta(x,y)} d\rho\, d\theta. \tag{5.4}$$

This formula reduces to Eq. (5.3) when $R \to \infty$. Note that the formula involves applying (x,y)-dependent weights to the ramp-filtered projections prior to backprojection. For an $N \times N$ scene with the number of projections proportional to N and the number of samples of each projection also proportional to N, Eq. (5.4) requires $O(N^4)$ computation. This exceeds the $O(N^3)$ computation for standard FBP, and the process can be a computational burden as the image size increases. It should also be noted that this formula is derived using the method of stationary phase, assuming that the employed radar frequencies are high.

5.3 Effect of Filtering in FBP

5.3.1 Simulation Setup

We first conduct a simple simulation to determine whether filtering in FBP seems to be less important in far-field SAR imaging than in Computed Tomography (CT). Since the two main differences between SAR and CT imaging are 1) the nature of the underlying image, i.e., whether it is complex or real valued, and 2) the location of the Fourier data grid, i.e. whether it is offset from or centered at the origin, we will assess the effect of filtering for the four associated cases.

Assume an underlying image that can be described by a discrete model:

$$g(x,y) = \sum_{m,n} f[m,n]\, \mathrm{e}^{j\phi[m,n]}\, h(x-n\Delta_x, y-m\Delta_y; \sigma_x, \sigma_y), \tag{5.5}$$

[1] See Appendix A.3 for derivation based on [40].

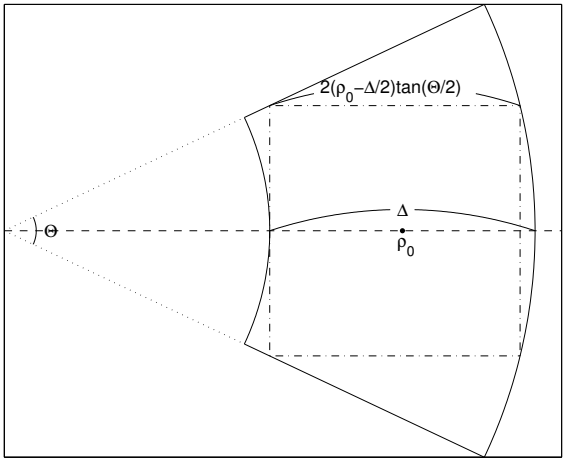

Figure 5.2: Polar data grid in 2-D Fourier domain for $\rho_0/\Delta = 1.5$. The polar data region circumscribes a square.

where f is a real-valued discrete-space image, ϕ is the spatial phase, and h is a kernel function whose 2-D Fourier transform is known analytically.[2] σ_x and σ_y are constants associated with the kernel function, and Δ_x and Δ_y are constants that associate the indices n and m of the discrete image with the spatial coordinates x and y, respectively. For a real-valued image g, we have $\phi[m,n] = 0$ for all (m,n)-pairs, and for a complex-valued image, we will assume the $\phi[m,n]$'s are drawn independently from a uniform distribution between $-\pi$ and π.

Then, the synthetic data are computed by

$$P[l,k] = \sum_{m,n} f[m,n]\, \mathrm{e}^{j\phi[m,n]}\, H(\rho[k], \theta[l]; n\Delta_x, m\Delta_y, \sigma_x, \sigma_y), \tag{5.6}$$

where $H(\rho,\theta; n\Delta_x, m\Delta_y, \sigma_x, \sigma_y) = \int\int h(x - n\Delta_x, y - m\Delta_y; \sigma_x, \sigma_y)\, \mathrm{e}^{-j2\pi\rho(x\cos\theta + y\sin\theta)} dxdy$, for spatial frequencies $\rho[k] \in \left[\rho_0 - \frac{\Delta}{2}, \rho_0 + \frac{\Delta}{2}\right]$ and angles $\theta[l] \in \left[-\frac{\Theta}{2}, \frac{\Theta}{2}\right]$. When the Fourier data are located offset from the origin, i.e. when $2\rho_0 \geq \Delta$, the range of angles Θ is chosen so that a square of width $2\left(\rho_0 - \frac{\Delta}{2}\right)\tan\left(\frac{\Theta}{2}\right)$ can be inscribed in the polar data region, as shown in Fig. 5.2. When the Fourier data are centered at the origin, i.e. when $\rho_0 = 0$, we have $\Theta = \pi$ and the data region forms a circular shape. From the synthesized Fourier data, we reconstruct the image by computing

$$\hat{g}[m',n'] = \sum_{l,k} P[l,k] Q[k]\, \mathrm{e}^{j2\pi\rho[k](n'\Delta'_x \cos\theta[l] + m'\Delta'_y \sin\theta[l])}, \tag{5.7}$$

where Q is a 1-D filter in the Fourier domain.

[2] Some examples of the kernel function are 1) impulse kernel $h(x,y;\sigma_x,\sigma_y) = \frac{1}{\sigma_x\sigma_y}\delta(\frac{x}{\sigma_x}, \frac{y}{\sigma_y})$, 2) rectangular kernel $h(x,y;\sigma_x,\sigma_y) = \frac{1}{\sigma_x\sigma_y}\,\mathrm{rect}(\frac{x}{\sigma_x}, \frac{y}{\sigma_y})$, and Gaussian kernel $h(x,y;\sigma_x,\sigma_y) = \frac{1}{2\pi\sigma_x\sigma_y}\exp\left(-\frac{x^2}{2\sigma_x^2} - \frac{y^2}{2\sigma_y^2}\right)$. The choice of kernel does not affect the observations made in this section.

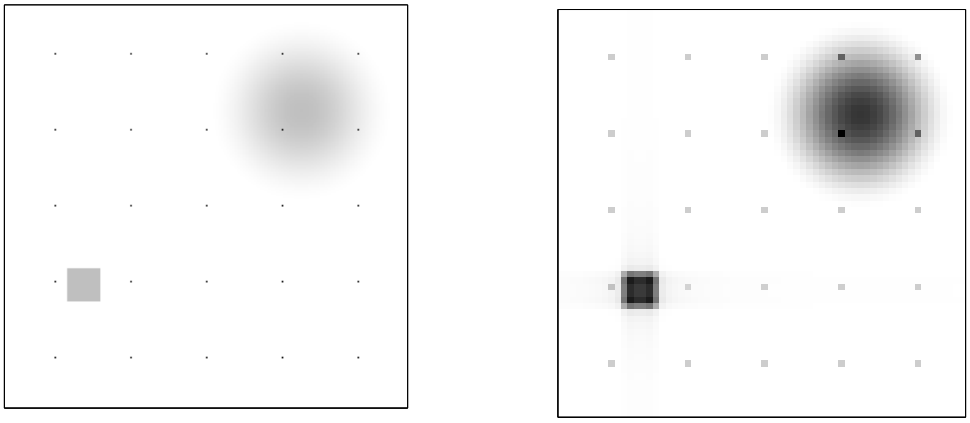

(a) (b)

Figure 5.3: Test image used to synthesize the Fourier data. (a) 256×256 image on a resolution cell of size $\Delta_x \times \Delta_y$, and (b) low-resolution version of the test image of size 64×64 with a four times coarser resolution in both directions.

To study the effect of filtering on various features in the image, we use a test image composed of isolated reflectors, a circular-shaped smooth object, and a square-shaped raised plateau, as shown in Fig. 5.3(a). Note that the resolutions Δ_x and Δ_y of the test image f are chosen to be four times denser than the spacings Δ'_x and Δ'_y of the reconstructed image so that Eq. (5.5), the underlying image model, can better represent continuous images. Figure 5.3(b) shows the test image reconstructed on the coarser grid, obtained by inverse Fourier transforming the Fourier data synthesized on a Cartesian grid. The isolated reflectors have lower intensity than other features in Fig. 5.3(b), since there is only one value in f that corresponds to each of the resolution cells representing an isolated reflector. Figure 5.3(b) will serve as a reference image for the FBP reconstructions shown in the next section since they have the same resolution.

5.3.2 Results

Figure 5.4 shows images reconstructed by FBP with and without filtering for the case where the Fourier data grid is centered at the origin. The top two images are reconstructions of the real-valued test image, and the bottom two are the averaged reconstructions for the complex-valued images over 100 realizations of the spatial phases. The left images correspond to FBP with ramp filtering, i.e., $Q[k] = |\rho[k]|$, and the right images correspond to backprojection without any filter applied. For the real-valued case, the image reconstructed by FBP is very similar to Fig. 5.3(b), the downsampled version of the test image; however, when the filtering was neglected, the reconstruction turned out to be blurry, as if it was low-pass filtered. A similar observation can be made for the complex-valued case. The averaged image without filtering looks like a smoothed version of the averaged FBP restoration, but the point targets still can be seen in Fig. 5.4(d). Note that the con-

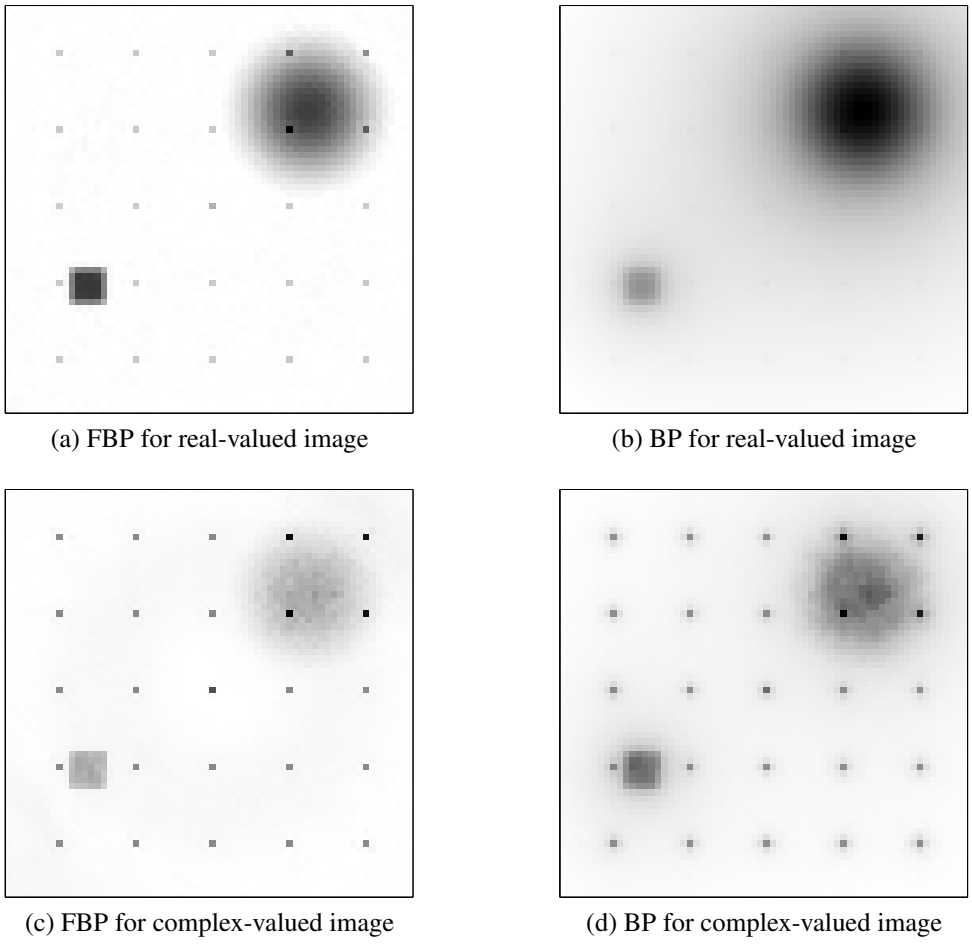

(a) FBP for real-valued image

(b) BP for real-valued image

(c) FBP for complex-valued image

(d) BP for complex-valued image

Figure 5.4: FBP restorations with and without the ramp filter for $\rho_0 = 0$. (a) FBP restoration of the real-valued image, (b) BP restoration of the real-valued image, (c) averaged FBP restoration of the complex-valued images, and (d) averaged BP restoration of the complex-valued images. Restorations for complex-valued images are averaged over 100 realizations of the spatial phases.

tinuous features have relatively lower magnitude than the isolated features in the complex-valued case due to destructive interference between neighboring pixel values in the test image [42].

Figure 5.5 shows a set of simulation results similar to those in Fig. 5.4, but for the case where the Fourier data are on an offset polar grid with $\rho_0/\Delta = 2$. For the real-valued case, the disk and most of the square are obscured in the reconstructed images since a major part of the low-frequency information was not provided, whereas point targets and vertical edges of the square can be seen. Vertical edges of the square are preserved due to the offset location of the Fourier data, as discussed in [42], despite the fact that we have the Fourier data in polar format and the images are reconstructed via backprojection. On the other hand, all features were well reconstructed for the complex-valued case, and the quality of the reconstruction remained similar to the case when there was no Fourier offset. Here, the interesting observation is that the images reconstructed with and

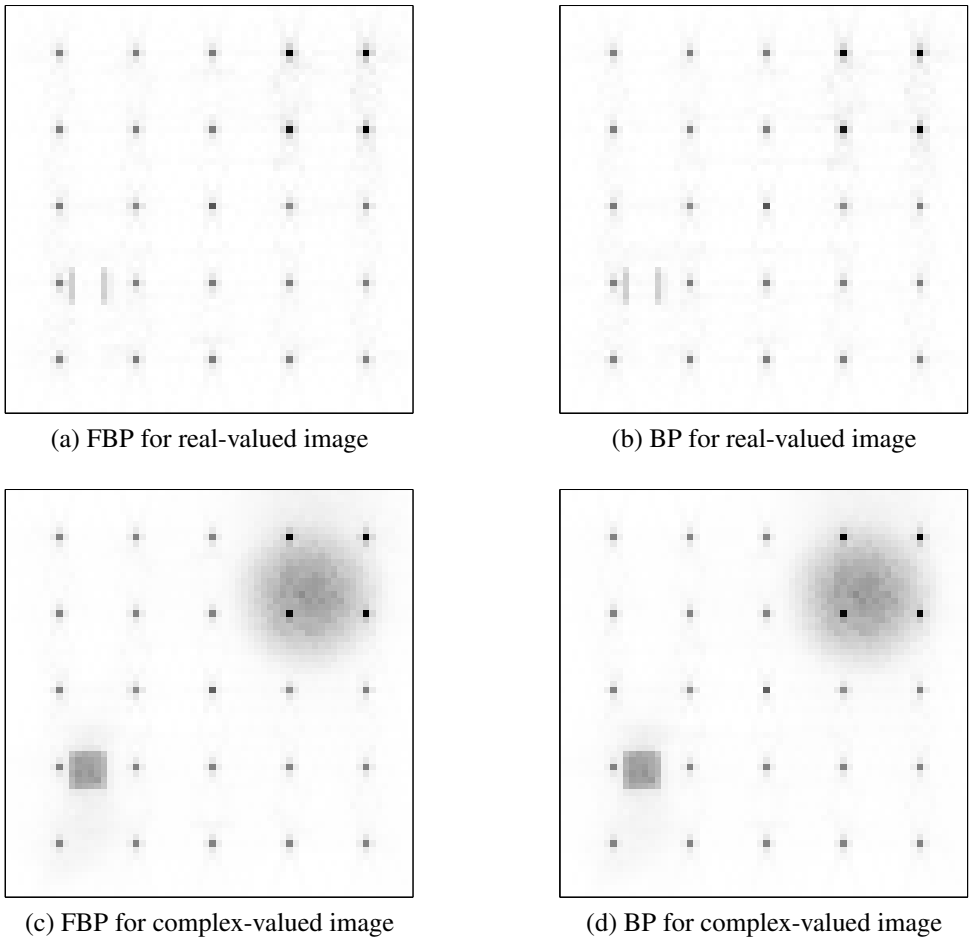

(a) FBP for real-valued image

(b) BP for real-valued image

(c) FBP for complex-valued image

(d) BP for complex-valued image

Figure 5.5: FBP restorations with and without the ramp filter for $\rho_0/\Delta = 2$. (a) FBP restoration of the real-valued image, (b) BP restoration of the real-valued image, (c) averaged FBP restoration of the complex-valued images, and (d) averaged BP restoration of the complex-valued images. Restorations for complex-valued images are averaged over 100 realizations of the spatial phases.

without filtering are nearly indistinguishable in both the real and complex-valued cases (although they are equally poor reconstructions for the real-valued case).

Considering both Figs. 5.4 and 5.5, the best reconstruction via backprojection without filtering was produced when the scene was complex valued (with uncorrelated spatial phases) and the Fourier data grid was located offset from the origin (Fig. 5.5(d)). However, if the question is, "When is the effect of filtering in FBP negligible?", the answer depends only on the location of the Fourier data grid.

5.4 Effect of Filtering on Point Target Responses

5.4.1 Point Target Responses for a Keystone-Shaped Data Region

In this section, we show how the Point Target Response (PTR) for FBP changes when the filtering step is omitted, and how the PTR is related to the amount of frequency offset and the range of look angles. For analytical tractability, we assume that the wavefronts are planar and that the SAR data are available within a keystone-shaped region rather than a polar region in the 2-D Fourier domain. Also, note that we analyze the PTRs in the continuous domain and consider only point targets at the center of the scene since the PTRs are spatially invariant.

Let μ and ν denote the range and cross-range spatial frequencies in the 2-D Fourier domain, respectively. The keystone-shaped data region is defined by

$$\left\{(\mu,\nu) \in \mathcal{R}^2 : |\nu| \le T_\Theta \mu \text{ and } |\mu - \mu_0| \le \Delta_\mu/2\right\},$$

where $T_\Theta = \tan\frac{\Theta}{2}$, and μ_0 and Δ_μ are positive constants satisfying $\mu_0 \ge \Delta_\mu/2$. The frequency offset ratio is defined by $K = 2\mu_0/\Delta_\mu$, where $K = 1$ corresponds to no offset. Although the range of look angles and the frequency range can be determined independently, they are often chosen so that the ranges of spatial frequencies in both directions are similar, thereby providing for similar resolution in the range and cross-range directions. Henceforth, unless otherwise stated, we choose the keystone region to circumscribe a square and the following holds:

$$\tan\left(\frac{\Theta}{2}\right) = \frac{1}{K-1}.$$

Some values of K and corresponding Θ are shown in Table 5.1, and an example of a keystone-shaped data region in the spatial frequency domain is shown in Fig. 5.6.

Table 5.1: Several values of the frequency offset ratio and the corresponding range of look angles.

K	1	2	4	8	16	32	64	128
Θ (degrees)	180	90	36.87	16.26	7.63	3.70	1.82	0.90

For the keystone-shaped data region and a point target at the origin, the PTRs for backprojection, with ramp filtering and without filtering, are given by

$$h_{rk}(x,y) \triangleq \int_{\mu_0-\Delta_\mu/2}^{\mu_0+\Delta_\mu/2} \int_{-T_\Theta\mu}^{T_\Theta\mu} \mathrm{e}^{j2\pi\{x\mu+y\nu\}} d\nu d\mu \tag{5.8}$$

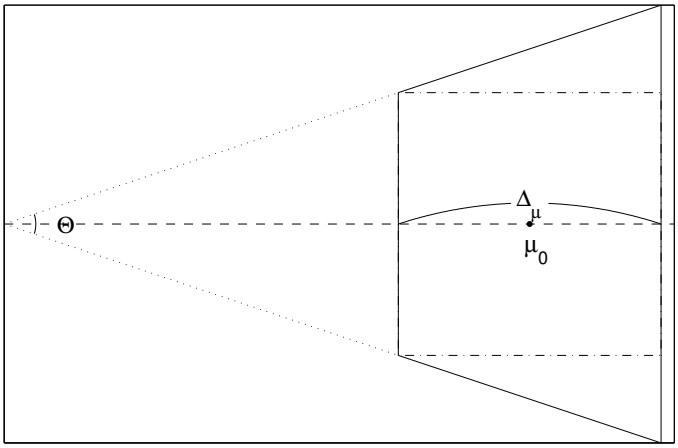

Figure 5.6: Keystone-shaped data region for $K = 4$. The solid lines define the keystone region which circumscribes a square indicated by the dash-dotted lines.

and

$$h_{0k}(x,y) \triangleq \int_{\mu_0-\Delta_\mu/2}^{\mu_0+\Delta_\mu/2} \int_{-T_\Theta\mu}^{T_\Theta\mu} \frac{1}{\sqrt{\mu^2+\nu^2}} \mathrm{e}^{j2\pi\{x\mu+y\nu\}} d\nu d\mu, \tag{5.9}$$

respectively. The subscripts r, k, and 0 of the PTRs stand for ramp filter, keystone, and 0 (no) filter, respectively.

5.4.2 1-D Analog of the Point Target Responses

The PTRs defined in the previous section cannot be expressed in closed form. Before comparing the two formulas, we will present a simpler analysis in 1-D to help learn what we can expect in the more complicated 2-D case. Although there is no concept of backprojection in 1-D, we will make an analog in 1-D to equations (5.8) and (5.9). Here, the inverse ramp filter $1/\sqrt{\mu^2+\nu^2}$ in 2-D will be replaced by a decreasing linear function. We define the 1-D functions analogous to the 2-D PTRs, with and without filtering, as

$$h_r(x) = \int_{f_0-\Delta/2}^{f_0+\Delta/2} \mathrm{e}^{j2\pi xf} df \tag{5.10}$$

and

$$h_0(x) = \int_{f_0-\Delta/2}^{f_0+\Delta/2} (-Af+B)\mathrm{e}^{j2\pi xf} df, \tag{5.11}$$

respectively. Here, $[f_0-\Delta/2, f_0+\Delta/2]$ is the data range in the 1-D Fourier domain, where $0 < \Delta \le 2f_0$, and the frequency offset ratio is $K = 2f_0/\Delta$. A and B are positive constants satisfying $-Af+B \approx 1/f$ for the frequencies f in the data range, where we chose $A = f_0^{-2}$ and $B = f_0^{-1}$ so that the line segment $-Af+B$ is tangent to $1/f$ at the center frequency $f = f_0$. Although there are

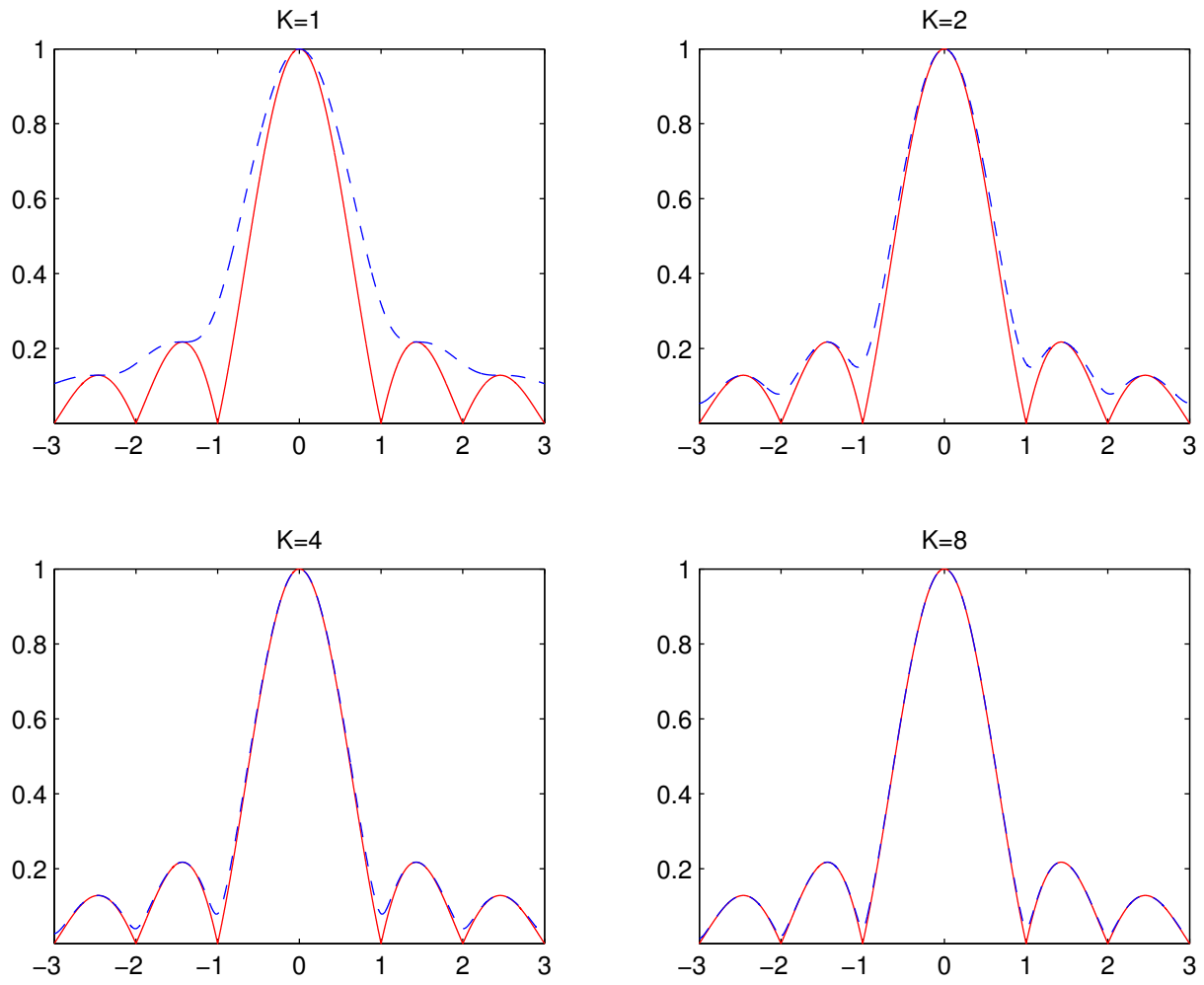

Figure 5.7: Plots of the functions $\bar{h}_r$ and $\bar{h}_0(;K)$ for different values of frequency offset ratio K. Red solid line and blue dotted line correspond to $\bar{h}_r$ and $\bar{h}_0(;K)$, respectively.

other choices of A and B that can make a good approximation, reasonable choices satisfy $A \propto f_0^{-2}$ and $B \propto f_0^{-1}$.

The closed-form formulae for the functions h_r and h_0, after appropriate normalization and change of variable, are

$$\bar{h}_r(z) = \mathrm{sinc}(z) \tag{5.12}$$

and

$$\bar{h}_0(z;K) = \mathrm{sinc}(z) + j\frac{1}{K}\frac{\cos(\pi z) - \mathrm{sinc}(z)}{\pi z}, \tag{5.13}$$

respectively. Here, the variable z corresponds to Δx. Figure 5.7 shows the two functions for 4 different values of frequency offset ratios. When there is no offset ($K = 1$), the functions are noticeably different, but the difference becomes negligible as K becomes larger.

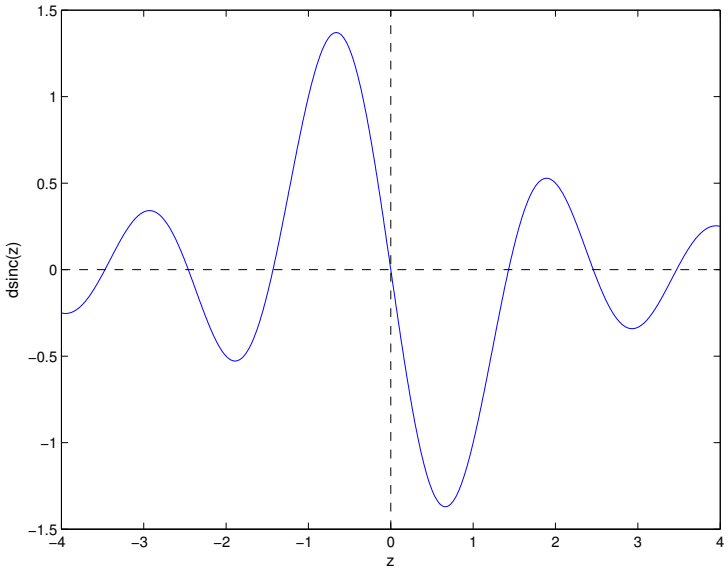

Figure 5.8: The derivative of sinc(z).

The difference between the two curves is

$$|\bar{h}_r(z) - \bar{h}_0(z;K)| = \frac{1}{\pi K}|\mathrm{dsinc}(z)|, \tag{5.14}$$

where

$$\mathrm{dsinc}(z) = \frac{\cos(\pi z) - \mathrm{sinc}(z)}{z} \tag{5.15}$$

is the derivative of sinc(z). A plot of the function dsinc is shown in Fig. 5.8, where the maximum of $\pi^{-1}|\mathrm{dsinc}(z)|$ is approximately 0.436182, occurring at $z \approx \pm 0.662586$. Equation (5.14) suggests that neglecting the filtering step introduces a small difference in the PTR, which is inversely proportional to the offset ratio K. The maximum difference is less than 10% of the peak value when $K > 4.362$.

We can make several observations on the difference of $\bar{h}_r$ compared to $\bar{h}_0$ in terms of the mainlobe and sidelobe characteristics. Simple mathematical analysis shows that the locations of the local maxima, peak values of sidelobes, and thus the Peak SideLobe Ratio (PSLR) are the same, which also can be observed from Fig. 5.7. However, the mainlobe width, -3dB resolution, and Integrated SideLobe Ratio (ISLR) change if we eliminate the filtering step, and as the value K changes.

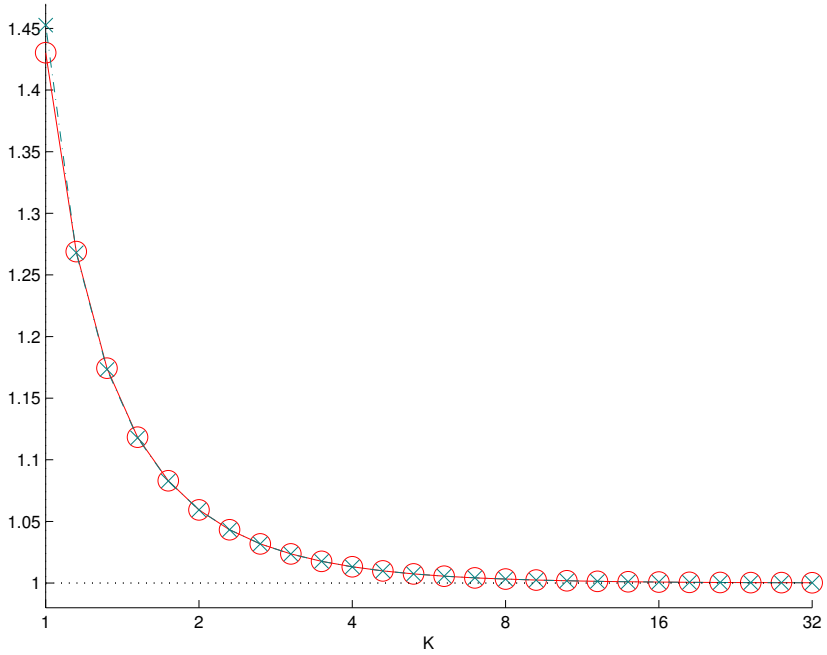

Figure 5.9: The half mainlobe width of $\bar{h}_0(;K)$ as a function of the frequency offset ratio K. The red circles represent the numerically computed values of the half mainlobe width and the green crosses represent the approximation, given by Eq. (5.18).

5.4.2.1 Mainlobe Width

The half mainlobe width of $\bar{h}_r$ is $z_{r,m} = 1$. Unlike $|\bar{h}_r|$, $|\bar{h}_0(;K)|$ does not have any nulls; instead, local minima occur at points satisfying the following equation:

$$\tan(\pi z) = \frac{2\pi z}{2 + \pi^2 (K^2 - 1)^2 z^2}. \tag{5.16}$$

Although we cannot derive a closed form expression for the half mainlobe width of $\bar{h}_0(;K)$, we can observe that the mainlobe is slightly widened when the filtering step is eliminated. The width is larger by only 6.7% when the frequency offset ratio is $K = 2$, and the widening becomes negligible as K becomes larger, as shown in Fig. 5.9 with red circles.

Let $z_{0,m}(K)$ denote the half mainlobe width of $\bar{h}_0(;K)$, i.e. the smallest z that satisfies Eq. (5.16). We derived[3] an upper bound for $z_{0,m}(K)$ given by

$$z_{0,m}(K) \leq 1 + \frac{2/\pi^2}{K^2 - 1}, \tag{5.17}$$

where the margin of the upper bound is less than about 0.01 when $K \geq 2$. From this upper bound, we see that $z_{0,m}(K) - z_{r,m} = O(K^{-2})$ as $K \to \infty$.

[3] See Appendix B for the derivation.

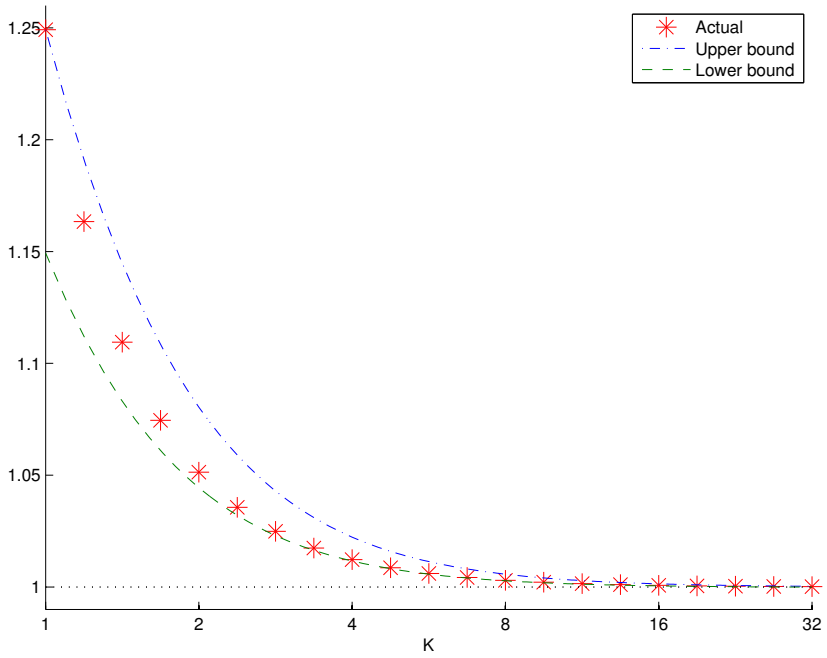

Figure 5.10: (HPHW of $\bar{h}_0(;K)$)/(HPHW of $\bar{h}_r$) and its upper and lower bounds given by Eq. (5.20).

We also derived[4] an approximation for the half mainlobe width:

$$z_{0,m}(K) \approx 1 + \frac{1-a}{4} \times \frac{2K^2 - a}{(2K^2-1)(K^2-a)}, \tag{5.18}$$

where $a = 1 - 8/\pi^2 \approx 0.18943$. The approximation to the half mainlobe width for $\bar{h}_0(z,K)$ is shown in Fig. 5.9 with green x's.

5.4.2.2 Half-Power Half-Width

Half-Power Half-Width (HPHW), also called -3dB resolution is the point where the power is half the maximum. The HPHW of the filtered impulse response is $z_{r,h} \approx 0.442946$, and the HPHW of $\bar{h}_0$ is z that satisfies

$$2\{\mathrm{sinc}(z) - \cos(\pi z)\}^2 = K^2\pi^2 z^2\{1 - 2\,\mathrm{sinc}^2(\pi z)\}. \tag{5.19}$$

The increase in HPHW of $\bar{h}_0(;K)$ with respect to $z_{r,h}$ is shown in Fig. 5.10 with red asterisks, where one can see that the difference becomes negligible for $K \geq 10$.

[4]See Appendix B for the derivation.

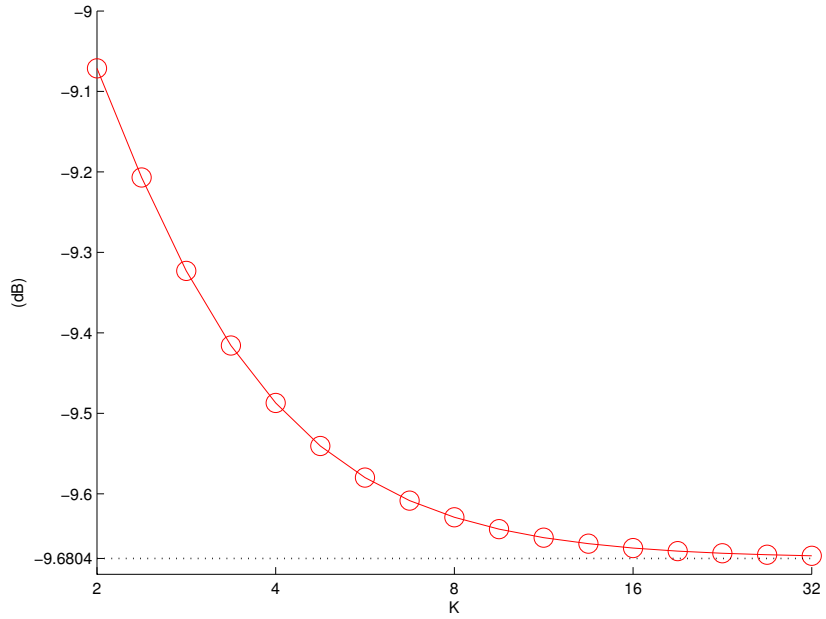

Figure 5.11: Integrated Sidelobe Ratio of $\bar{h}_0(;K)$. The dashed line corresponds to the ISLR of $\bar{h}_r$.

We have shown that $z_{0,h}(K)$, the HPHW of $\bar{h}_0$, satisfies[5]

$$b_1 + b_2\sqrt{1+\frac{b_3}{K^2}} \le z_{0,h}(K) \le c_1 + c_2\sqrt{1+\frac{c_3}{K^2}}, \tag{5.20}$$

where $b_1 = 1/3$, $b_2 \approx 0.1095$, $b_3 \approx 1.5752$, $c_1 \approx 0.3321$, $c_2 \approx 0.1108$, and $c_3 \approx 2.9845$. Figure 5.10 shows the upper and lower bounds in blue and green lines, respectively.

5.4.2.3 Integrated Sidelobe Ratio

The Integrated SideLobe Ratio (ISLR) is defined as the ratio of the energy in the sidelobes to the energy in the mainlobe. For $\bar{h}_r$, ISLR is[6] $\pi/\{2\,\mathrm{Si}(2\pi)\} - 1 \approx 0.107634$, where Si is the sine integral function: $\mathrm{Si}(x) = \int_0^x \frac{\sin(t)}{t} dt$. Measured in dB, the ISLR is $-9.68(dB)$. Without the filtering, we have shown that[6]

$$(\mathrm{ISLR})\{\bar{h}_0(;K)\} \approx \frac{\pi}{2}\left\{\mathrm{Si}\left(2\pi z_{0,m}(K)\right) - \frac{\sin^2\left(\pi z_{0,m}(K)\right)}{\pi z_{0,m}(K)}\right\}^{-1} - 1. \tag{5.21}$$

Figure 5.11 shows the ISLR of $\bar{h}_0(;K)$ as a function of the frequency offset ratio. The dash-dotted line indicates the ISLR of $\bar{h}_r$, which is a lower bound to the ISLR of $\bar{h}_0(;K)$.

[5] See Appendix C for the derivation.
[6] See Appendix D for the derivation.

5.4.2.4 Summary of Results

Table 5.2 summarizes the effect of eliminating filtering, in the 1-D analysis, for the various image focus measures.

Table 5.2: Amount of increase in image focus measures, due to elimination of filtering, from the 1-D analysis.

K (corresponding Θ)	Mainlobe Width	HPHW	ISLR	PSLR
$1\,(180^o)$	42.9 %	24.9 %	13.8 %	0 %
$2\,(90^o)$	5.9 %	5.1 %	15.0 %	0 %
$4\,(36.87^o)$	1.3 %	1.2 %	4.5 %	0 %
$8\,(16.26^o)$	0.3 %	0.3 %	1.2 %	0 %
$16\,(7.63^o)$	0.1 %	0.1 %	0.3 %	0 %

5.4.3 2-D Impulse Responses

Equation (5.8) can be expressed as

$$h_{rk}(x,y) = 2\mu_0\Delta_\mu T_\Theta e^{j2\pi\mu_0 x}\left[\operatorname{sinc}(2\mu_0 T_\Theta y)\frac{\operatorname{sinc}\left(\Delta_\mu(x+T_\Theta y)\right)+\operatorname{sinc}\left(\Delta_\mu(x-T_\Theta y)\right)}{2}\right.$$
$$\left. -j\frac{\cos(2\pi\mu_0 T_\Theta y)}{2\pi\mu_0 T_\Theta}\frac{\operatorname{sinc}\left(\Delta_\mu(x+T_\Theta y)\right)-\operatorname{sinc}\left(\Delta_\mu(x-T_\Theta y)\right)}{2y}\right]. \tag{5.22}$$

for $y \neq 0$. Equation (5.9) can be simplified to a single-variable integration:

$$h_{0k}(x,y) = \Delta_\mu e^{j2\pi\mu_0 x}\int_{-T_\Theta}^{T_\Theta}\frac{1}{\sqrt{1+t^2}}\operatorname{sinc}\{\Delta_\mu(x+yt)\}e^{j2\pi\mu_0 yt}dt, \tag{5.23}$$

but, a closed-form expression is difficult to derive. Hence, instead of comparing the 2-D impulse response functions h_{rk} and h_{0k} for all (x,y), we compare their cross-sections along the range and cross-range axii.

The slices of the impulse response of FBP using the ramp filter are

$$h_{rk}(x,0) = 2\mu_0\Delta_\mu T_\Theta e^{j2\pi\mu_0 x}\left\{\operatorname{sinc}(\Delta_\mu x) - j\frac{1}{\pi K}\operatorname{dsinc}(\Delta_\mu x)\right\}, \tag{5.24}$$

along the range axis, and

$$h_{rk}(0,y) = 2\mu_0\Delta_\mu T_\Theta\ \operatorname{sinc}(K\Delta_\mu T_\Theta y)\ \operatorname{sinc}\left(\Delta_\mu T_\Theta y\right) \tag{5.25}$$

along the cross-range axis, where $K = 2\mu_0/\Delta_\mu$ for 2-D keystone-grid data. The slices of the impulse response of backprojection without filtering are

$$h_{0k}(x,0) = 2\Delta_\mu \ln\left(\sqrt{1+T_\Theta^2}+T_\Theta\right) e^{j2\pi\mu_0 x}\,\mathrm{sinc}(\Delta_\mu x), \tag{5.26}$$

along the range axis, and

$$\begin{aligned}
h_{0k}(0,y) &= \frac{1}{j2\pi y}\int_{-T_\Theta}^{T_\Theta}\frac{1}{t\sqrt{1+t^2}}\left\{e^{j2\pi(\mu_0+\Delta_\mu/2)yt}-e^{j2\pi(\mu_0-\Delta_\mu/2)yt}\right\}dt && (5.27)\\
&\approx \frac{\ln\left(\sqrt{1+T_\Theta^2}+T_\Theta\right)}{j2\pi T_\Theta y}\int_{-T_\Theta}^{T_\Theta}\frac{1}{t}\left\{e^{j2\pi(\mu_0+\Delta_\mu/2)yt}-e^{j2\pi(\mu_0-\Delta_\mu/2)yt}\right\}dt && (5.28)\\
&= \frac{\ln\left(\sqrt{1+T_\Theta^2}+T_\Theta\right)}{\pi T_\Theta y}\int_{-1/K}^{1/K}\frac{\sin\{2\pi\mu_0 T_\Theta y(1+s)\}}{1+s}ds && (5.29)\\
&\approx \frac{\ln\left(\sqrt{1+T_\Theta^2}+T_\Theta\right)}{\pi T_\Theta\left\{1-(\Delta_\mu/2\mu_0)^2/3\right\}y}\int_{-1/K}^{1/K}(1-s)\sin\{2\pi\mu_0 T_\Theta y(1+s)\}\,ds && (5.30)\\
&= \frac{2\Delta_\mu\ln\left(\sqrt{1+T_\Theta^2}+T_\Theta\right)}{1-(1/K)^2/3}\Big\{\mathrm{sinc}(K\Delta_\mu T_\Theta y)\,\mathrm{sinc}(\Delta_\mu T_\Theta y)\\
&\qquad +\frac{1}{K^2}\cos(2\pi\mu_0 T_\Theta y)\frac{\mathrm{dsinc}(\Delta_\mu T_\Theta y)}{\pi\Delta_\mu T_\Theta y}\Big\} && (5.31)
\end{aligned}$$

along the cross-range axis. The first approximation, Eq. (5.28), holds when $T_\Theta \ll 1$, i.e. when $\Theta \ll 90^o$, and is very accurate for practical ranges of look angles. The second approximation, Eq. (5.30), holds when $\Delta_\mu/2\mu_0 \ll 1$.

Let $\bar{h}_{rk}$ and $\bar{h}_{0k}$ be the normalized impulse responses of h_{rk} and h_{0k}, respectively. The differences in the normalized impulse responses, when eliminating the filtering process in FBP, are

$$|\bar{h}_{0k}(x,0)-\bar{h}_{rk}(x,0)| = \frac{1}{K}\left|\mathrm{dsinc}(\Delta_\mu x)\right| \tag{5.32}$$

and

$$\begin{aligned}
|\bar{h}_{0k}(0,y)-\bar{h}_{rk}(0,y)| &\approx \frac{1}{3K^2-1}\times\\
&\left|\mathrm{sinc}(K\Delta_\mu T_\Theta y)\,\mathrm{sinc}(\Delta_\mu T_\Theta y)+3\cos(\pi K\Delta_\mu T_\Theta y)\frac{\mathrm{dsinc}(\Delta_\mu T_\Theta y)}{\pi\Delta_\mu T_\Theta y}\right|. && (5.33)
\end{aligned}$$

Since the function $\mathrm{dsinc}(x)$ has its minimum at $x \approx 0.6626$, the maximum difference in the normalized impulse responses along the range axis is $\frac{\sin(0.6626\pi)}{2K}$. That is, the effect of omitting the filtering

step on the impulse response along the range axis becomes negligible as the Fourier offset ratio K increases, and, more specifically, the maximum change in the function value is inversely proportional to K. Deriving a closed-form expression for the maximum value of the impulse response along the cross-range axis seems intractable; however, we simply observe from Eq. (5.33) and simulations that the peak value decreases faster as K increases than that of the impulse response along the range axis.

The difference between the normalized impulse responses $\bar{h}_{rk}$ and $\bar{h}_{0k}$ is shown in Fig. 5.12. Figure 5.12(a) is the slice along $y = 0$, and Fig. 5.12(b) is the slice along $x = 0$. As suggested by the formula, the differences diminish quickly as the frequency offset ratio increases, especially for the cross-section along the cross-range direction, in which the difference is small even for small frequency offset ratios.

5.5 Near-Field SAR Imaging via FBP and Filtering

5.5.1 Point Target Responses for Near-Field FBP

From the near-field FBP formula Eq. (5.4), the PTRs corresponding to a point target at (x_0, y_0) for near-field FBP, with and without filtering, are

$$h_{qp}(x,y;x_0,y_0) = \int_{-\Theta/2}^{\Theta/2} \frac{(x+R)R\sec^2\theta}{(x+R)^2+(y+R\tan\theta)^2} \int_{\rho_0-\Delta/2}^{\rho_0+\Delta/2} \rho\, \mathrm{e}^{j2\pi\rho\{r_\theta(x,y)-r_\theta(x_0,y_0)\}} d\rho\, d\theta \tag{5.34}$$

and

$$h_{0p}(x,y;x_0,y_0) = \int_{-\Theta/2}^{\Theta/2} \int_{\rho_0-\Delta/2}^{\rho_0+\Delta/2} \mathrm{e}^{j2\pi\rho\{r_\theta(x,y)-r_\theta(x_0,y_0)\}} d\rho\, d\theta, \tag{5.35}$$

respectively. Since the PTRs cannot be expressed in closed form and are difficult to analyze, we will examine the effect of filtering via simulation. Fortunately, the PTRs can be reduced to single-variate integrals, and we can simply use numerical evaluation of the integrals to form 2-D images of the PTRs.

The reduced forms are

$$h_{qp}(x,y;x_0,y_0) = \rho_0\Delta \int_{-\Theta/2}^{\Theta/2} \frac{(x+R)R\sec^2\theta}{(x+R)^2+(y+R\tan\theta)^2} \left\{\mathrm{sinc}(D_\theta) - \frac{j}{\pi K}\,\mathrm{dsinc}(D_\theta)\right\} \mathrm{e}^{j\pi K D_\theta} d\theta \tag{5.36}$$

and

$$h_{0p}(x,y;x_0,y_0) = \Delta \int_{-\Theta/2}^{\Theta/2} \mathrm{sinc}(D_\theta)\mathrm{e}^{j\pi K D_\theta} d\theta, \tag{5.37}$$

where D_θ is shorthand notation for $\Delta\{r_\theta(x,y) - r_\theta(x_0,y_0)\}$ and $K = \rho_0/\Delta$ for 2-D polar-grid data. Note that $h_{qp}(x_0,y_0;x_0,y_0)$ has different values for different point target locations, and so the corre-

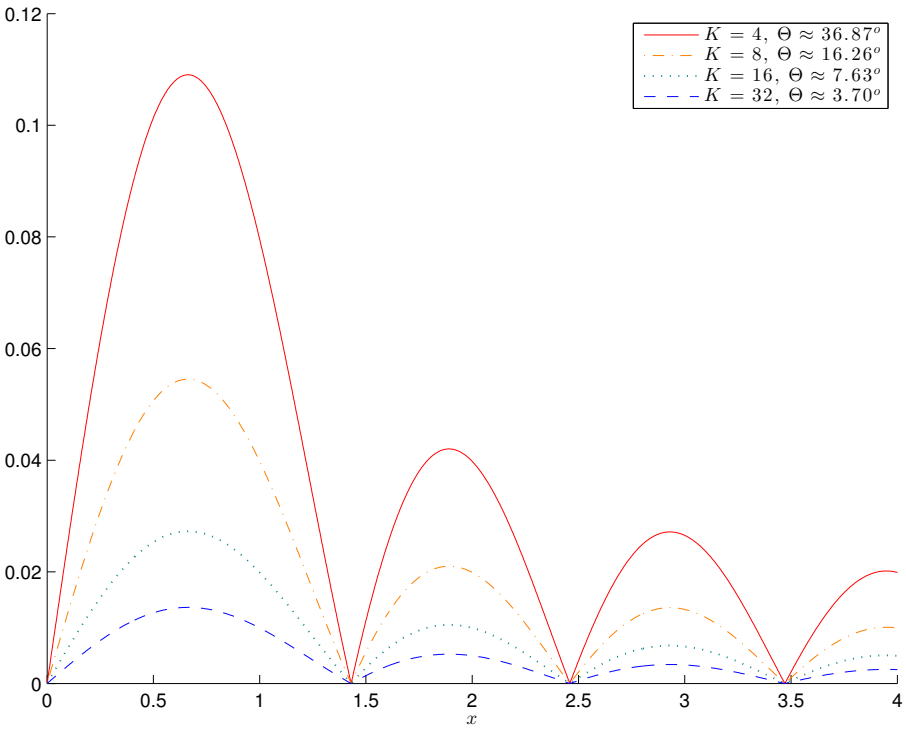

(a)

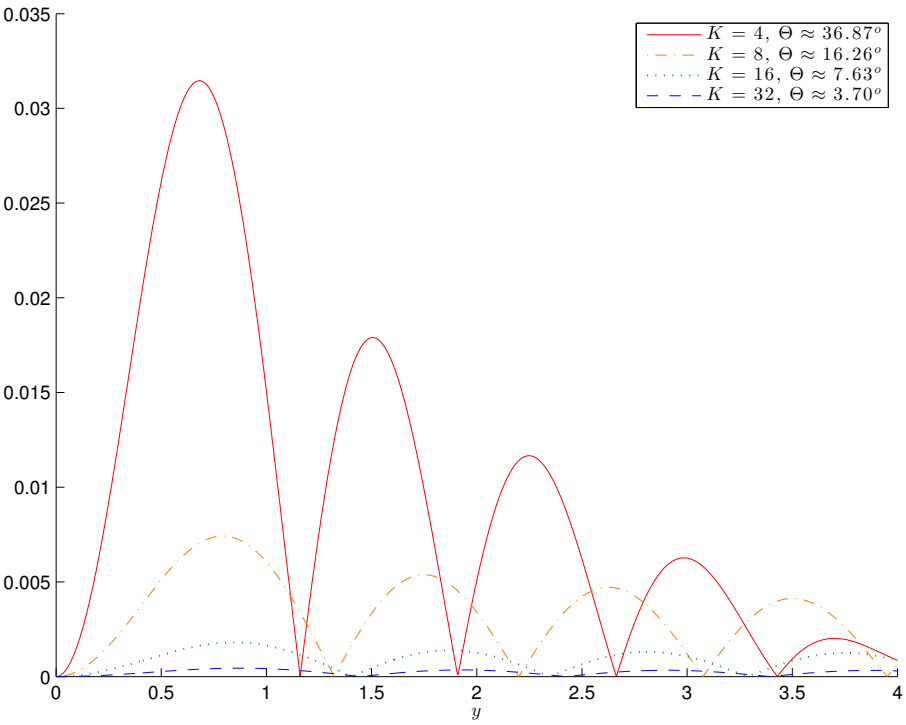

(b)

Figure 5.12: Slices of $|\bar{h}_{0k}(x,y) - \bar{h}_{rk}(x,y)|$ for different frequency offset ratios and $\Delta_\mu = 1$. (a) $|\bar{h}_{0k}(x,0) - \bar{h}_{rk}(x,0)|$ and (b) $|\bar{h}_{0k}(0,y) - \bar{h}_{rk}(0,y)|$. Note that both are even functions and values only in the positive range are shown.

sponding FBP reconstruction for the near-field case needs to be normalized with a spatially-variant factor to account for this. Throughout our simulations of PTRs, we use normalization factors that make the maximum value of the PTRs equal to one. That is, we normalize h_{qp} by dividing it by

$$h_{qp}(x_0, y_0; x_0, y_0) = \rho_0 \Delta \int_{-\Theta/2}^{\Theta/2} \frac{(x_0 + R) R \sec^2 \theta}{(x_0 + R)^2 + (y_0 + R\tan\theta)^2} d\theta \tag{5.38}$$

$$= \rho_0 \Delta \left\{ \tan^{-1}\left(\frac{y_0 + R\tan(\frac{\Theta}{2})}{x_0 + R} \right) - \tan^{-1}\left(\frac{y_0 - R\tan(\frac{\Theta}{2})}{x_0 + R} \right) \right\}. \tag{5.39}$$

Figures 5.13 and 5.14 show contours of the PTRs computed via numerical integration. The calculation for Fig. 5.13 is done for an extreme near-field case where $R = 20$, i.e. the center of the flight path is located at $(-20, 0)$ in the image coordinates of each subfigure. The width of the scene is 25. Figure 5.14 shows calculated results for a moderate near-field case with $R = 100$. The left and the right columns correspond to FBP with and without filtering, respectively, and the first, second, and third rows correspond to different frequency offset ratios of $K = 2$, $K = 4$, and $K = 8$. Each subfigure is composed of PTRs at 25 different locations, where the borders of the calculated PTRs are marked with dotted lines. (Each of the 25 PTRs was computed separately for a small region surrounding the point target location, and is shown only within that region.) Each of the PTRs is normalized, and the contour levels are $0.1, 0.2, \ldots, 0.9$. The frequency bandwidth Δ was set equal to one.

As shown in Fig. 5.13, the PTRs do not look ideal, whether we apply filtering or not, when there is significant wavefront curvature across the imaged scene. Furthermore, the PTRs have different shape and resolution depending on the location of the point target. The nonideal features are due to the inexactness of the inverse formula for such an extreme near-field scenario. The tilted shape and the space-variant resolution can be partly explained by examining the geometry of backprojection. A more detailed explanation of the nonideal features is provided in Appendix E. Here, we will focus on the difference the filtering step makes.

Filtering does not produce perfect reconstructions, but, filtered backprojection does create slightly sharper PTRs than does backprojection without filtering. The difference between the filtered and unfiltered backprojections is apparent when $K = 2$, but the difference becomes less noticeable as K increases. This remains true when there is less wavefront curvature and the non-ideal features are less observable, as shown in Fig. 5.14. However, it is challenging to evaluate the importance of the filtering step in the near field compared to the far-field case from the 2-D figures, since the PTRs rely on multiple parameters, such as the location of the point targets, radar parameters, and wavefront curvature.

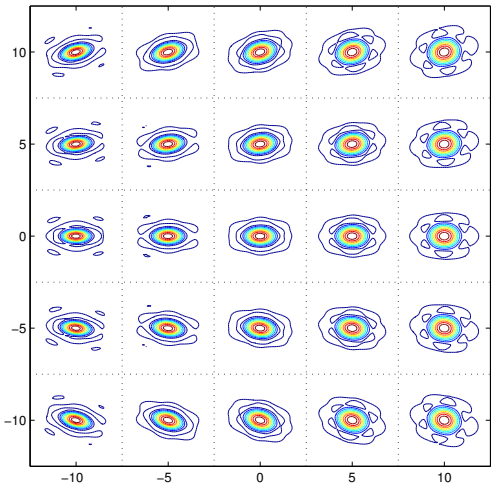

(a) Filtered BP: $K = 2, \Theta = 85.6^o$

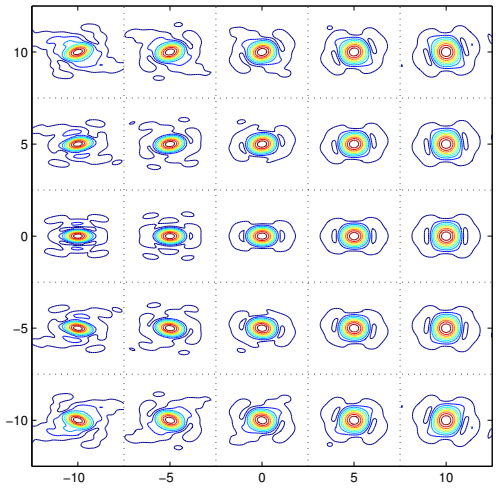

(b) BP: $K = 2, \Theta = 85.6^o$

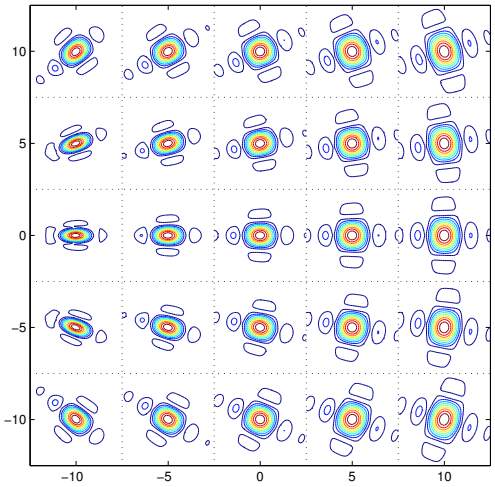

(c) Filtered BP: $K = 4, \Theta = 35.3^o$

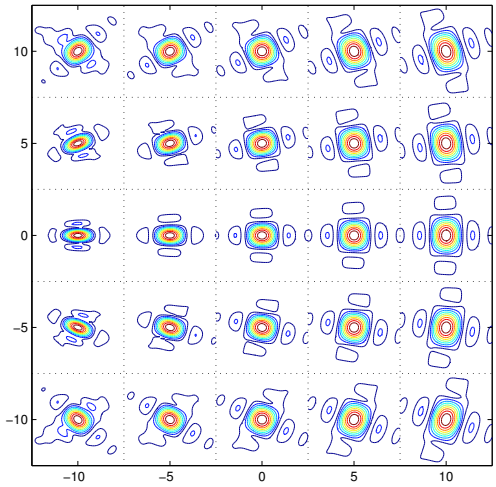

(d) BP: $K = 4, \Theta = 35.3^o$

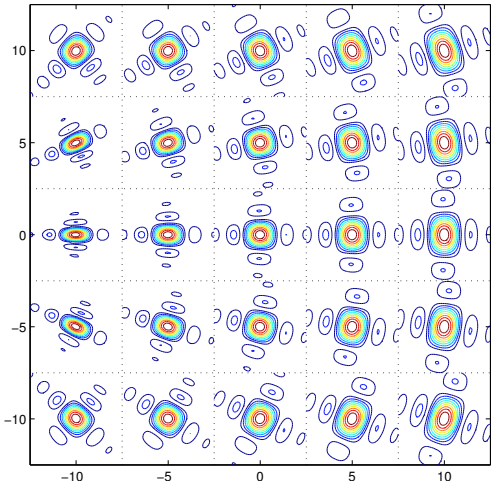

(e) Filtered BP: $K = 8, \Theta = 15.8^o$

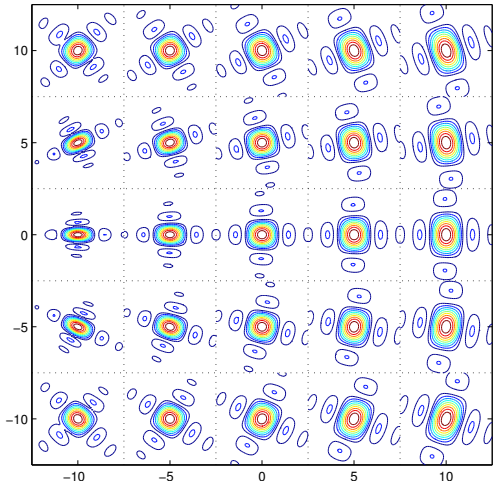

(f) BP: $K = 8, \Theta = 15.8^o$

Figure 5.13: Contours of the PTRs of backprojection with and without filtering for $R = 20$. (a), (c), and (e) are filtered backprojections and (b), (d), and (f) are backprojections without filtering.

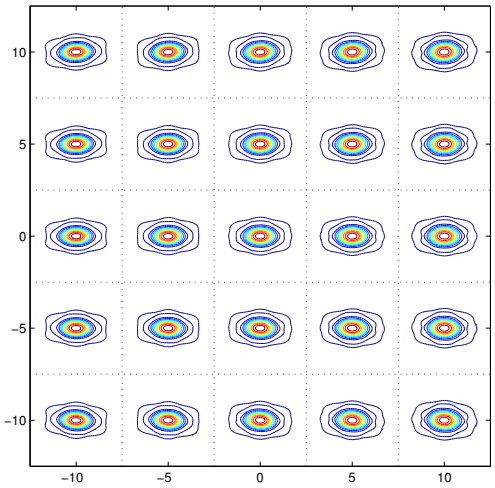

(a) Filtered BP: $K = 2, \Theta = 85.6^o$

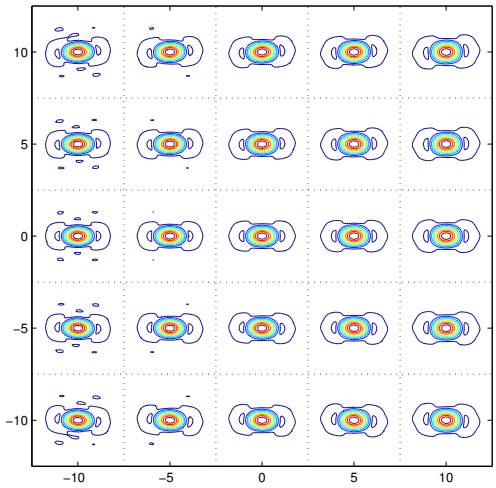

(b) BP: $K = 2, \Theta = 85.6^o$

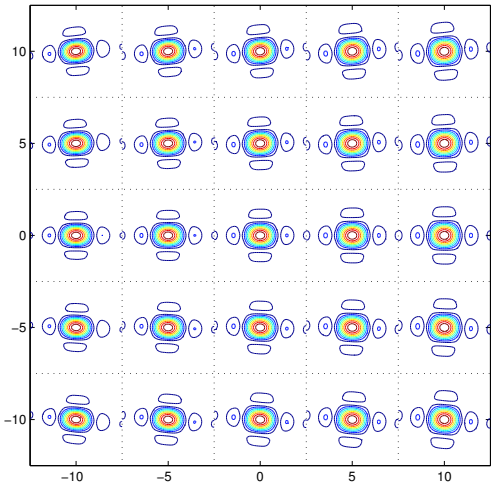

(c) Filtered BP: $K = 4, \Theta = 35.3^o$

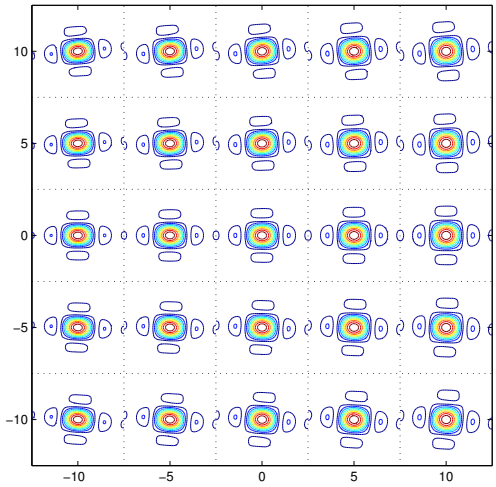

(d) BP: $K = 4, \Theta = 35.3^o$

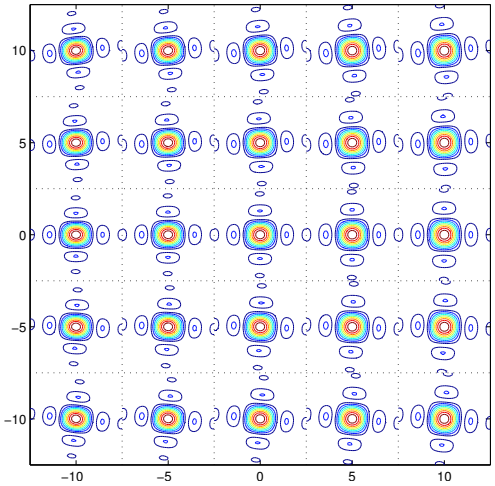

(e) Filtered BP: $K = 8, \Theta = 15.8^o$

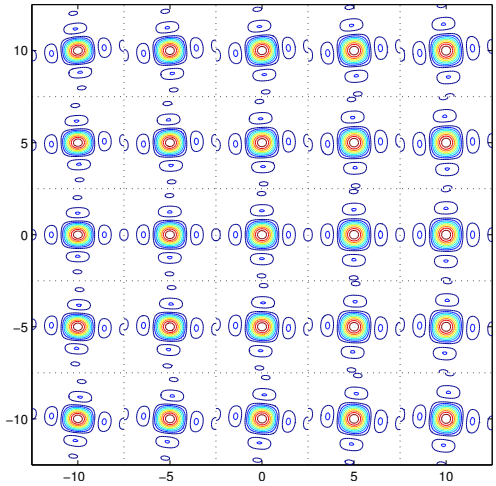

(f) BP: $K = 8, \Theta = 15.8^o$

Figure 5.14: Contours of the PTRs of backprojection with and without filtering for $R = 100$. (a), (c), and (e) are filtered backprojections and (b), (d), and (f) are backprojections without filtering.

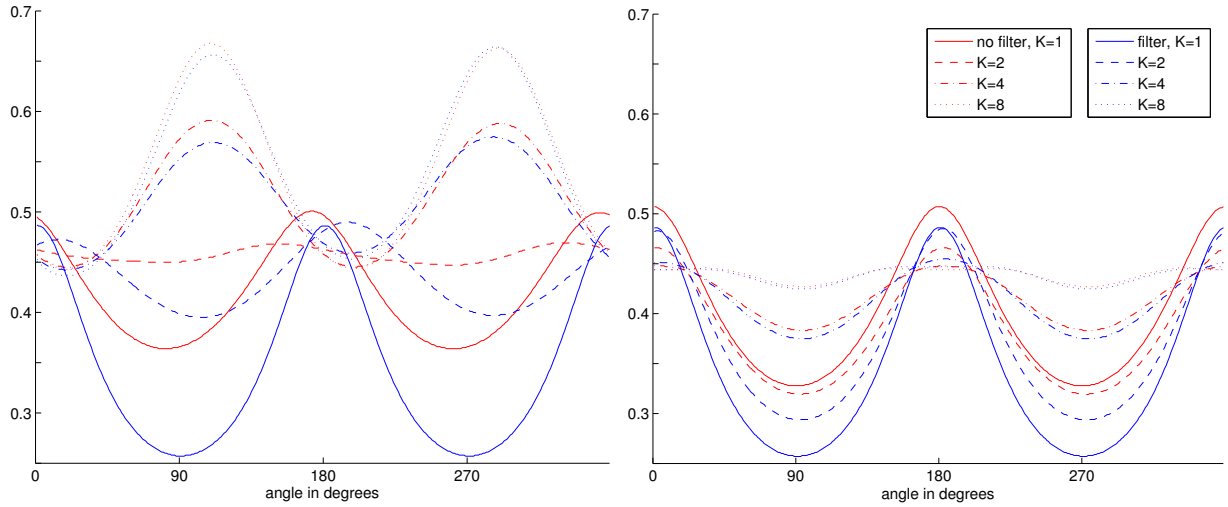

(a) $R = 20$ (b) $R = 160$

Figure 5.15: HPHW as a function of angle from the point target location: $(10, 10)$. (a) For $R = 20$ and (b) for $R = 160$.

5.5.2 When can we omit filtering?

We will use HPHW of the PTRs as the measure of image quality to provide a guideline for whether the filtering step can be omitted for the near field case. Since the PTRs are 2-D functions, HPHW can be defined for all angular directions at the point target location. Figure 5.15 shows HPHW as a function of angular direction for a point target located at $(x_0, y_0) = (10, 10)$. The red lines and the blue lines correspond to the PTRs for FBP without and with the filtering step, respectively, and the solid, dashed, dash-dot, and dotted lines correspond to frequency offset ratios of 1, 2, 4, and 8, respectively. Figure 5.15 (a) shows the calculated result for $R = 20$. The filtering and no-filtering cases do not show much resemblance to each other for smaller values of K, but they become very similar as K increases. For a larger value of R, the red and blue lines become more similar to each other, as shown in Fig. 5.15(b). However, since HPHW increases as filtering is omitted for some angular directions, and decreases for others, it is difficult to assess from this figure whether filtering improves image quality.

Figure 5.16 shows the increase in average HPHW of the PTR when filtering is omitted. That is, the HPHW of the backprojection without filtering is averaged over all angular directions and compared to that of FBP. The increase in average HPHW serves as a measure of the effectiveness of filtering, where a larger value indicates more degradation in image quality when the filtering step is omitted. As shown in the figure, regardless of the values of R and K, omitting the filtering step results in lower resolution. However, the positive effect of filtering diminishes quickly as the frequency offset ratio increases. (Note that the vertical axis is plotted on a logarithmic scale.) Increased wavefront curvature also increases average HPHW, however, by only a small amount.

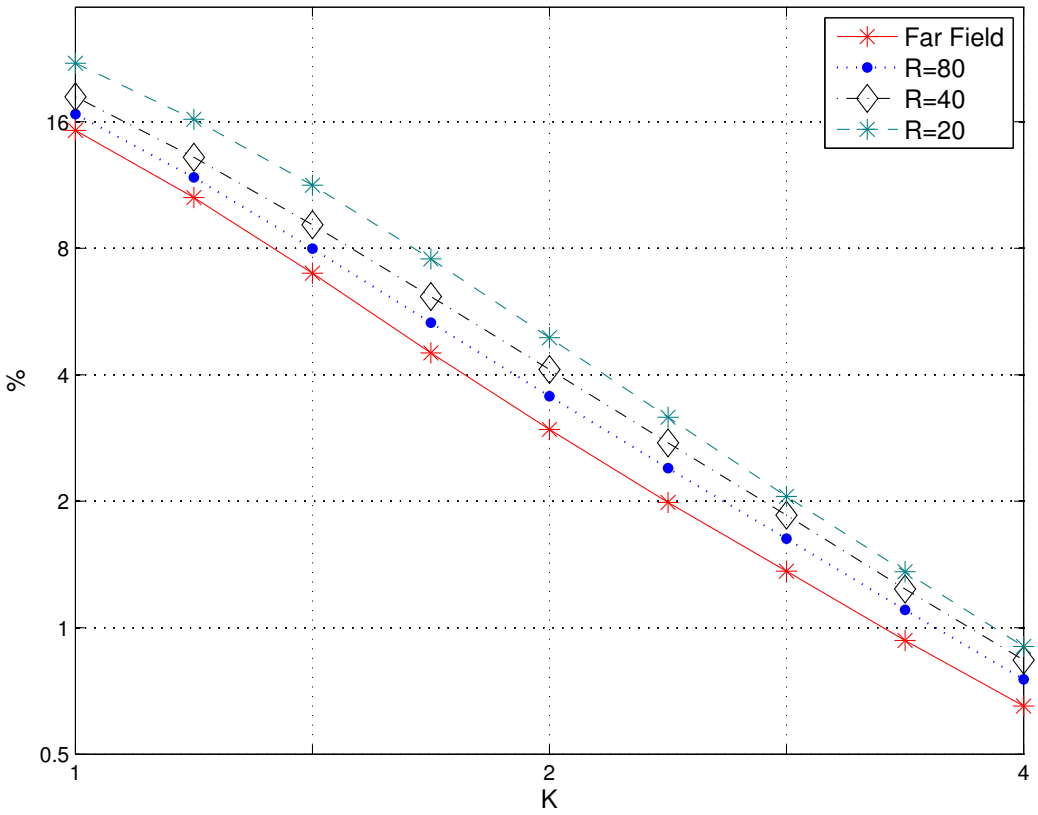

Figure 5.16: Increase in average HPHW of the point target response when filtering is omitted, for a point target located at $(10, 10)$. Note that both the axes are in logarithmic scale.

For a frequency offset ratio of $K \geq 4$, filtering makes 1% or less change in the average HPHW, regardless of the amount of wavefront curvature.

CHAPTER 6

Imaging onto a Known DEM: Back-Projection and Autofocus

6.1 Introduction

This chapter considers the SAR imaging and defocusing problem when a DEM of the scene terrain is known. Terrain elevation can obtained through lidar [44], photogrammetry [45], interferometric SAR [46], or surveying drones [47], and many datasets are openly available, e.g., USGS DEMs [48]. Traditional tomographic imaging methodologies [1,49] assume that the radar operates far from the scene where the scene terrain can be viewed as nearly flat and the wavefronts of the radar reaching the scene almost planar. However, generally speaking, the SAR scene is on non-flat terrain, and negligence of wavefront curvature and elevation of scatterers induces defocus and even results in displacement or layover of prominent structures in the reconstructed image.

The degradation in image quality can be avoided by taking into account a pre-existing DEM and wavefront curvature in the reconstruction step. Several post-processing steps for the widely used PFA for SAR imaging have been proposed to remove distortions from both elevation-induced defocusing effects and wavefront curvature [6, 38]. However, the SAR defocusing problem formulated as a result of phase errors in the demodulated data is difficult to solve in conjuction with several post-processing steps after PFA. In contrast, backprojection-based imaging techniques are easily modified to directly integrate the non-flat DEM and curved wavefronts into the algorithm. A few papers have suggested the extension of back-projection to non-flat terrain or near-field scenarios using different rationale, based on microlocal analysis [40], analogy to delay-and-sum beamforming [35], and intuition [50]. All of these algorithms can be viewed as members of a larger class of algorithms that we call Filtered Back-Projection along Curves (FBPC), essentially differing only in the employed filters.

Mathematically speaking, FBPC is an elegant extension of Filtered Back-Projection (FBP).

[0]This chapter includes research conducted jointly with David C. Munson, Jr. [43].

However, the proposed FBPC algorithms in the literature are not able to perfectly recover the underlying image of interest. This is due to the fact that the filters employed in FBPC are derived through approximations, and, usually, these approximations break down for the most challenging of scenarios. The quality of the images reconstructed by FBPC has not been studied in depth. Little is known about what data collection geometry, radar parameters, and terrain geometry limit and affect the image quality. Furthermore, the effect of incorrect information of the DEM on the FBPC reconstruction has not been analyzed. In this chapter, we study the performance of FBPC with a focus on the image resolution for varying geometric parameters. We also discuss the importance of using the correct DEM within the one-step imaging process.

FBPC has the potential to provide simple solutions to the defocusing problem for a general set of SAR scenarios. However, utilization of FBPC in autofocus algorithms has not received much attention until recently. Only a handful of autofocus algorithms have been proposed using FBPC with a known DEM. [51] extends the use of the widely employed PGA algorithm through approximations. [52] proposes a metric-based solution that uses intensity squared as the image sharpness metric. [53] formulates the problem as a parameterized optimization problem and proposes to solve it with an iterative solver. In this chapter, we propose an autofocus algorithm that is an extension of the MCA algorithm [21], where the DEM is directly integrated into the linear algebraic framework of MCA.

The organization of this chapter is as follows. In Section 6.2, the SAR imaging scenario with non-flat terrain is introduced and notation is established. Existing methods for imaging onto a known DEM are reviewed, and the formula for FBPC is presented. In Section 6.3, we suggest the use of a spatially-variant normalization constant and derive expressions for the resolution of FBPC from the PTR. Simulation results are shown to validate the analytical results. Section 6.4 considers the defocusing problem and extends the use of MCA to the scenario with a known DEM. Performance of extended MCA is assessed via simulation results.

6.2 Background

6.2.1 Problem Setting and Notation

We consider a SAR imaging scenario where the DEM of a 3-D scene is known and the radar is operating in spotlight mode. The radar energy is assumed to be non-penetrating and the pulse returns are collected over a single pass. Assuming that there is no occlusion between the radar and the scene, we can reconstruct an image on a nonflat terrain. For simplicity, we assume that the radar flight path is straight and level and that the modality is *broadside*. In broadside collection, the center pulse is transmitted in the direction perpendicular to the flight path. The data collection

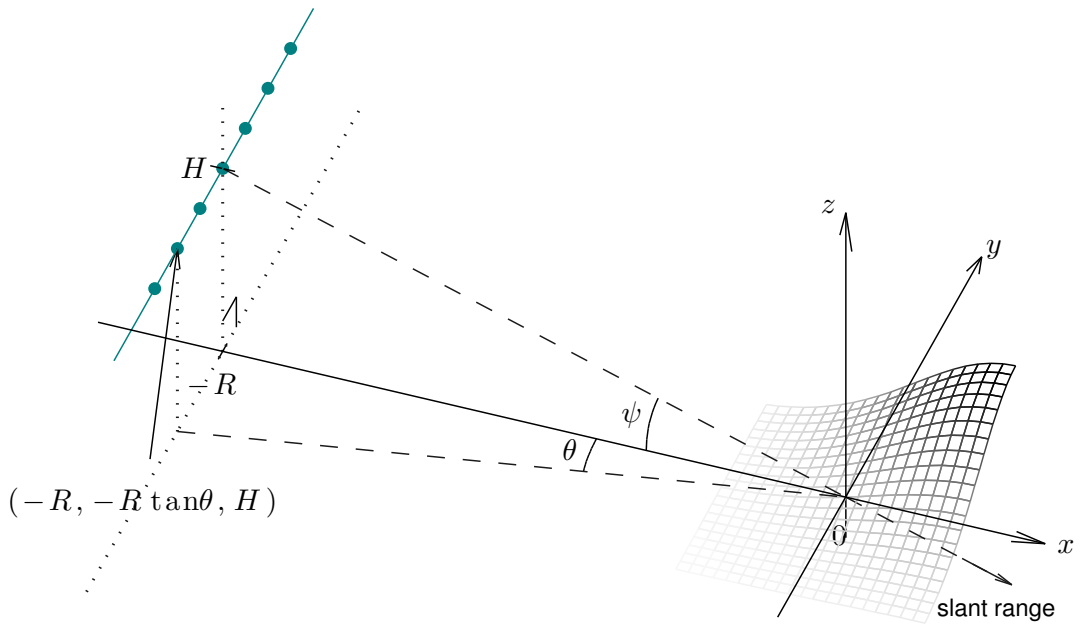

Figure 6.1: Collection geometry of SAR imaging for a straight-line, level, broadside acquisition. x and y denote the range and cross-range, respectively, and z denotes the direction orthogonal to the ground plane (x-y plane). Radar pulses are transmitted and received at elevated points indicated by the green dots, which are at a constant elevation $z = H$ and standoff range $x = -R$. The cross-range coordinate of the radar is $-R\tan\theta$ for a look angle θ. In spotlight mode, the radar antenna is constantly steered towards a fixed reference point $(0,0,0)$ of the underlying scene. In broadside collection, the center pulse is transmitted at look angle $\theta = 0$. ψ denotes the grazing angle from the center of the synthetic aperture.

geometry is shown in Fig. 6.1, where the scene of interest lies on a terrain shown on the bottom right.

The direction of the flight path defines the *cross-range direction* and the direction of the center pulse defines the *slant-range direction*, where the two dimensions determine a plane called the *slant plane*. We generally want to form an image in coordinates matching that of the ground plane. The *range direction* is defined by the direction perpendicular to the cross-range direction on the ground plane. The range and cross-range coordinates are denoted by x and y, respectively, and the coordinate corresponding to the elevation is denoted by z. Without loss of generality, we define the origin of the 3-D coordinate system to be at center of the scene, and describe the radar flight path by $\{(-R, -R\tan\theta, H) : \theta \in [-\Theta/2, \Theta/2]\}$, where $R > 0$ is the *standoff range*, $H > 0$ is the elevation of the radar, θ is the *look angle*, and $\Theta > 0$ is *the range of look angles*. The grazing angle (of the center pulse) is denoted by $\psi = \text{atan}^{-1}(H/R)$. The elevation of the terrain is defined by $z = h(x,y)$, where h is continuous and its first derivatives exist for the scene of interest.

The objective is to image the 2-D complex-valued reflectivity $g(x,y)$ on the terrain $\{(x,y,h(x,y))\}$

in 3-D. A linear FM chirp, described by Re$\{s(t)\}$, with

$$s(t) = e^{j(\omega_0 t + \alpha t^2)}, \quad t \in [-T/2, T/2], \tag{6.1}$$

is transmitted and the return is collected and processed through a quadrature demodulator as in [1]. The resulting demodulated data is given by

$$P_\theta(\rho) = \int g(x,y)\, e^{j2\pi\rho r_\theta(x,y)} dxdy, \quad \rho \in \left[\rho_0 - \frac{\Delta}{2}, \rho_0 + \frac{\Delta}{2}\right], \tag{6.2}$$

where $\rho_0 = \omega_0/c\pi$, $\Delta = 2\alpha T/c\pi$, and c is the speed of light. Also, $r_\theta(x,y) = d_\theta(x,y) - d_\theta(0,0)$, where

$$d_\theta(x,y) = \sqrt{(x+R)^2 + (y + R\tan\theta)^2 + (h(x,y) - H)^2} \tag{6.3}$$

is the distance between the point on the terrain at (x,y) and the radar platform at look angle θ.

The *SAR defocusing problem* arises when there are errors in the estimated round-trip delay $2d_\theta(0,0)/c$ used in the quadrature demodulator, which result in phase errors in the demodulated data. The phase errors are constant for each return, but generally vary across look angle and can be highly uncorrelated. The image reconstructed from such erroneous data are defocused, and the phase errors need to be corrected through the use of *autofocus* algorithms. Our objective is to propose a robust autofocus algorithm for SAR images on a known DEM and study its performance and limitation for various scenarios.

6.2.2 Existing Approaches Using a Known DEM

Since autofocus algorithms are coupled to the imaging algorithms, we will first review the existing 3-D SAR imaging algorithms onto a hyperplane and how they are modified when the DEM is non-flat and known. Then, we will introduce and discuss the limitations of some existing autofocus algorithms that exploit the known DEM.

The tomographic formulation under the far-field assumption allows us to interpret the demodulated SAR data as samples of Fourier transformations of the reflectivity function. Each demodulated return from an aperture position corresponds to a line segment in the 3D Fourier domain, where the radial extent of the line segment is determined by the frequencies employed by the radar pulse. Also, the angular coordinates of the line segment in a spherical coordinate system are determined by the angular coordinates of the aperture position in the 3-D spatial domain. This is according to the linear trace version of the projection-slice theorem [6]. Hence, the collection of the demodulated data lies on a possibly non-planar surface in 3-D Fourier space, in general.

For straight-line and level aperture motion, the collection surface is planar and the SAR data

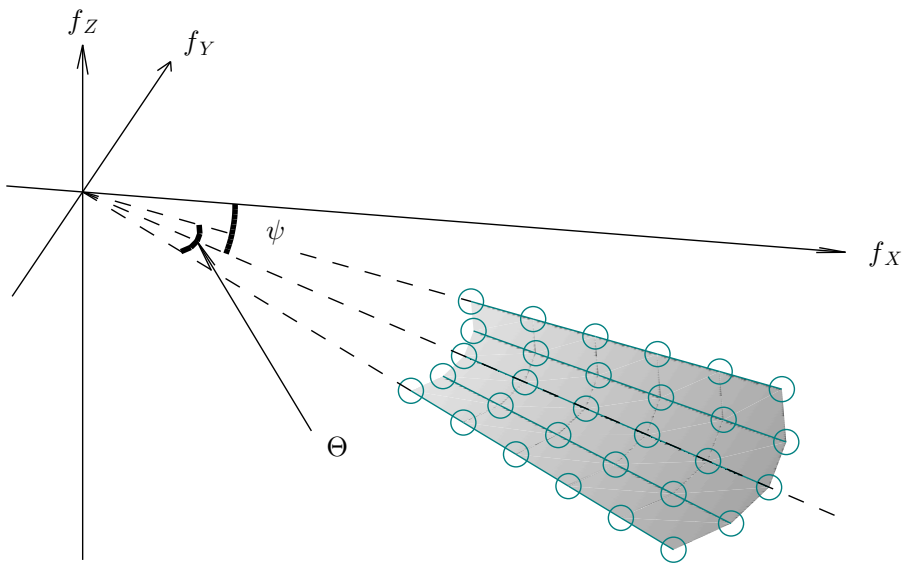

Figure 6.2: SAR data collected on a slant plane in 3-D spatial frequency domain for a straight-line level flight path in far field. f_X, f_Y, and f_Z denote the spatial frequencies in the range, cross-range, and elevation direction, respectively. Each group of green circles connected with a line correspond to SAR data acquired from a single look angle. Note that the collection surface in the spatial frequency domain is described with the same angular arguments ψ and Θ as the triangle defined by the radar flight path and the reference point in the spatial domain. For an arbitrary flight path, the collection surface is not flat in general.

are collected on a polar raster on the slant plane. This is illustrated in Fig. 6.2. The slant plane in the spatial frequency domain is the f_X-f_Y plane rotated around the f_Y-axis by the radar grazing angle ψ, where f_X and f_Y are the spatial frequencies in the range and cross-range directions, respectively. The most popular image formation method, termed the Polar Formatting Algorithm (PFA), resamples the polar-grid data onto a Cartesian grid and then utilizes an inverse 2-D FFT to form a slant-plane image. According to the planar slice theorem [6], the slant-plane image is a projection of the 3-D scene onto the slant plane in the spatial domain, which is a plane that includes the synthetic aperture and the scene center.

In general, however, it is desired to form a SAR image in the ground plane instead of the slant plane. The ground-plane image resembles the 3-D scene projected onto the ground-plane, but in the direction normal to the slant plane (not normal to the ground plane) due to the nature of the collection geometry. One way to produce a ground-plane image is to warp the slant-plane image onto the corresponding ground-plane coordinates. Another way is to project the SAR data onto the ground plane (f_X-f_Y plane) in the 3-D Fourier domain, resample, and then inverse Fourier transform. The difference between the two methods is clear only when the radar is in squint mode (antenna pointed ahead of or behind broadside), where the point target responses in the former method exhibits skewed sidelobes [6].

When the terrain is not flat and the topography is not known, elevated scatterers in the scene

are projected in the direction normal to the slant plane and onto the ground plane, resulting in height-proportional displacement. This is referred to as the "layover" phenomenon, whether or not the scatterers are displaced or actually laid over other objects. The layover phenomenon is unavoidable in both the ground-plane and the slant-plane images when the terrain elevation is unknown, in which case the images produced cannot be viewed as projections of the scene from any direction. Thus, pre-existing knowledge of the DEM is essential to produce an orthographically correct image. When the DEM is known, warping of the slant-plane image onto the known terrain can help remove the layover effect.

In case the collection surface is curved and not planar, the SAR data first are first projected onto the plane of interest in the direction orthogonal to the ground plane prior to using PFA. However, the elevated scatterers become defocused by an amount that depends on the amount of deviation from a planar collection surface and also the elevation. This error cannot be corrected by simply warping the image onto the known DEM.

Furthermore, since the wavefronts are spherical rather than exactly planar, the demodulated data are not exactly Fourier transforms of the reflectivity. The effect of the wavefront curvature can be approximated by a geometric distortion and spatially-variant defocusing in the image, which can be diminished by warping and filtering, respectively, the image afterwards [38]. Removing spatially-variant defocusing through filtering is computationally demanding and inaccurate for low-frequency radars or near-field imaging, but the computational burden can be lifted by using spatially-invariant filtering for neighboring pixels for high-frequency radars operating at a large standoff range.

In short, even in the simplest case of a straight-line, level acquisition path in the far field, the conventional method to produce an image on a known DEM is a two-step process, where knowledge of the DEM is used only in the second step. Also, a computationally expensive third step should be added to remove wavefront curvature effects when there is considerable amount of wavefront curvature. Moreover, this approach is not suitable for a more general set of scenarios involving arbitrary flight paths, low-frequency radars, or extreme near-field imaging.

Fortunately, there is another family of SAR imaging algorithms arising from the tomographic formulation that can be modified in a straightforward manner to directly compute the image on a known DEM. Such algorithms use FBPC, where the Beam Forming Algorithm (BFA) [35] and the inversion formula proposed by Nolan and Cheney [40] are the best known. Although PFA has been widely preferred over backprojection until recently due to computational efficiency, developments in fast algorithms for backprojection [3–5, 50, 53] have made the computational cost comparable. This allows us to contemplate the advantages of backprojection over PFA, which are apparent in scenarios where the terrain is not flat and the DEM is known. These algorithms can eliminate the layover effect in many cases, account for wavefront curvature and an arbitrary flight path, and can

be adapted for squint mode.

The SAR defocusing problem mostly has been studied under the far-field assumption, relying on the Fourier relationship between SAR data and the image. Thus, most existing autofocus algorithms are not suitable for a non-flat terrain, and only a few methodologies exploit the knowledge of a DEM in the defocusing problem. Jakowatz et al. proposed a way to apply Phase Gradient Autofocus (PGA), a well-known autofocus algorithm developed under the far-field assumption, in situations with a known DEM by employing the fact that BFA can produce an image on an arbitrary grid [51]. However, the image on the suggested grid is related to SAR data via Fourier transformation only through an approximation, and extended PGA is expected to perform well only under certain conditions. Ash uses FBP in the development of a metric-based autofocus algorithm that maximizes intensity squared [52], and Torgrimsson et al. proposed a parametric optimization using Fast Factorized Back-Projection (FFBP) [53]. Although the adoption of a known DEM into their formulations are straightforward, use of DEM is not the focus of their papers and is not studied in depth.

In this chapter, we focus on 3-D imaging onto a DEM, and the objective is to develop a robust autofocus methodology and study the performance in wide range of scenarios. The proposed algorithm relies on FBP along curves, where we explicitly use the filter proposed by Nolan and Cheney, although any reasonable filter can be used in the formula. There are two reasons why we use the Nolan-Cheney filter; first, we want to provide an explicit formulation of the solution and also to analyze the performance for varying parameters, and second, the analysis easily can be modified to use BFA instead, since BFA is a simplification and approximation of the Nolan-Cheney inversion formula.

6.2.3 Filtered Back-Projection along Curves Using the Known DEM

FBPC takes the form of

$$\hat{g}(x,y) = \int_{-\Theta/2}^{\Theta/2} \int_{\rho_0-\Delta/2}^{\rho_0+\Delta/2} F(x,y,\rho,\theta) P_\theta(\rho)\, \mathrm{e}^{j2\pi r_\theta(x,y)\rho}\, d\rho d\theta, \tag{6.4}$$

where F is a filter and $\hat{g}$ is the reconstructed image. By using the Nolan-Cheney filter for the scenario described in Sec. 6.2.1, the image reconstruction formula becomes[1]

$$\hat{g}(x,y) = f_1(x,y) \int_{-\Theta/2}^{\Theta/2} f_2(x,y;\theta) \int_{\rho_0-\Delta/2}^{\rho_0+\Delta/2} |\rho| P_\theta(\rho)\, \mathrm{e}^{j2\pi r_\theta(x,y)\rho}\, d\rho d\theta, \tag{6.5}$$

[1] See appendix A for details on reformatting the inversion formula from [40].

where

$$f_1(x,y) = \left| \left(1 + \frac{x}{R}\right) + \frac{h(x,y) - H}{R} \frac{\partial h}{\partial x}(x,y) \right| \tag{6.6}$$

and

$$f_2(x,y;\theta) = \frac{R^2 \sec^2\theta |\{d_\theta(x,y)\}^2 + (y + R\tan\theta - 1)(h(x,y) - H)\frac{\partial h}{\partial y}(x,y)|}{\{d_\theta(x,y)\}^4} \tag{6.7}$$

are spatially-variant weights. Note that Eq. (6.5) is a generalization of the FBPC formula in Eq. (5.4) in Chapter 5. The filter was derived based on microlocal analysis [54], which focuses on the reconstruction of singularities, e.g. edges and boundaries. The derivation also used the method of stationary phase [31,55], in which the radar frequencies and the standoff range were assumed to be large; thus, the filter works best for high-frequency radars and far-field imaging. Note that BFA is backprojection along curves without the filtering step, i.e. $F(x,y,\rho,\theta) = 1$, and is not a perfect inversion formula either.

6.3 Filtered Backprojection onto the Known DEM

As stated in the previous section, FBPC is not able to perfectly recover the underlying image and the reconstruction quality depends on various parameters. In this section, we study how the image quality depends on the amount of wavefront curvature, terrain gradient, radar grazing angle, and the use of DEM.

6.3.1 Spatially-Variant Normalization and the Normalized FBPC

We first look at the PTR and show how FBPC should be normalized to produce even strength for point scatterers over different locations within the scene. Let $h(x,y;x_0,y_0)$ be the PTR corresponding to a point target located at (x_0,y_0). Since the demodulated data corresponding to the point target at (x_0,y_0) are $P_\theta(\rho) = \mathrm{e}^{-j2\pi r_\theta(x_0,y_0)\rho}$, the PTR is

$$h(x,y;x_0,y_0) = \rho_0 \Delta f_1(x,y) \int_{-\Theta/2}^{\Theta/2} f_2(x,y;\theta) \left\{ \mathrm{sinc}(\Delta q_\theta) - j\frac{1}{\pi K}\mathrm{dsinc}(\Delta q_\theta) \right\} \mathrm{e}^{j\pi K \Delta q_\theta}\, d\theta, \tag{6.8}$$

where q_θ is shorthand notation for $r_\theta(x,y) - r_\theta(x_0,y_0)$ and $K = 2\rho_0/\Delta$ is the *frequency offset ratio*. Here, dsinc is the derivative of the sinc function which was defined in Eq. (5.15). The point target response at the center of the point target is $\rho_0 \Delta f_1(x_0,y_0) \int f_2(x_0,y_0;\theta) d\theta$, whose value clearly depends on the location (x_0,y_0). This suggests that the FBPC formula is not an exact inverse, and moreover, that a spatially-variant normalization is required to make each point target to have a unit response at its center location.

The FBPC reconstruction with proper normalization is then given by

$$\bar{g}(x,y) = \frac{1}{\rho_0 \Delta}\left\{\int_{-\Theta/2}^{\Theta/2} f_2(x,y;\theta)d\theta\right\}^{-1} \int_{-\Theta/2}^{\Theta/2} f_2(x,y;\theta) \int_{\rho_0-\Delta/2}^{\rho_0+\Delta/2} |\rho| P_\theta(\rho)\, \mathrm{e}^{j2\pi r_\theta(x,y)\rho}\, d\rho d\theta, \qquad (6.9)$$

where the spatially-variant weight f_2 is given in Eq. (6.7). Note that the weight f_2 and the normalization constant both depend on the geometry of the terrain around the imaging point. Although the normalization constant seems to be a fairly complicated integral, it is possible to compute an explicit formula. We derived[2] an explicit formula for the case where the numerator of f_2 is positive for all look angles, i.e., for (x,y) satisfying

$$\{d_\theta(x,y)\}^2 + (y + R\tan\theta - 1)(h(x,y) - H)\frac{\partial h}{\partial y}(x,y) > 0, \quad \forall\theta. \qquad (6.10)$$

When the radar is not illuminating the ground from a nearly top-down viewpoint, the above condition is satisfied for most (x,y)-locations where the terrain is not too steep in the cross-range direction. Since large grazing angles are not beneficial in terms of the range resolution, SAR applications generally do not operate from a top-down view. Thus, Eq. (6.10) is satisfied for most imaging scenarios with smooth terrain.

The normalized FBPC formula also can be simplified for some special cases.

6.3.1.1 Special Case - Flat Level Terrain

When $h(x,y) = 0, \forall(x,y)$, we have

$$r_\theta(x,y) = \sqrt{(x+R)^2 + (y + R\tan\theta)^2 + H^2} - \sqrt{R^2\sec^2\theta + H^2} \qquad (6.11)$$

and

$$f_2(x,y;\theta) = \frac{R^2\sec^2\theta}{\{d_\theta(x,y)\}^2} = \frac{R^2\sec^2\theta}{(x+R)^2 + (y+R\tan\theta)^2 + H^2}. \qquad (6.12)$$

Equation (6.10) is always satisfied and we have

$$\int f_2(x,y;\theta)d\theta = \frac{R}{\sqrt{(x+R)^2+H^2}}\left\{\tan^{-1}\left(\frac{y + R\tan\frac{\Theta}{2}}{\sqrt{(x+R)^2+H^2}}\right) - \tan^{-1}\left(\frac{y - R\tan\frac{\Theta}{2}}{\sqrt{(x+R)^2+H^2}}\right)\right\}. \qquad (6.13)$$

[2] See Appendix F.1.

6.3.1.2 Special Case - Far Field

When $H = aR$ for some constant $a > 0$ and $R \to \infty$, we have

$$r_\theta(x,y) \to \frac{1}{\sqrt{1+a^2\cos^2\theta}}\{x\cos\theta + y\sin\theta + a\cos\theta h(x,y)\} \tag{6.14}$$

and

$$f_2(x,y;\theta) \to \frac{\left|1+a^2\cos^2\theta - a\sin\theta\cos\theta\frac{\partial h}{\partial y}(x,y)\right|}{(1+a^2\cos^2\theta)^2}. \tag{6.15}$$

For the points where the gradient satisfies

$$\left|\frac{\partial h}{\partial y}(x,y)\right| < \begin{cases} \left\{1+a^2\cos^2\frac{\Theta}{2}\right\} / \left(a\sin\frac{\Theta}{2}\cos\frac{\Theta}{2}\right), & \Theta \le 2\tan^{-1}(\sqrt{1+a^2}) \\ 2\sqrt{1+a^2}/a, & \Theta > 2\tan^{-1}(\sqrt{1+a^2}), \end{cases} \tag{6.16}$$

the normalization constant is[3]

$$\int_{-\Theta/2}^{\Theta/2} f_2(x,y;\theta)d\theta = \frac{R}{S(x,y)}\left\{\tan^{-1}\left(\frac{y+R\tan\frac{\Theta}{2}}{S(x,y)}\right) - \tan^{-1}\left(\frac{y-R\tan\frac{\Theta}{2}}{S(x,y)}\right)\right\}, \tag{6.17}$$

where $S(x,y) = \sqrt{(x+R)^2 + (h(x,y)-H)^2}$. The range of look angles is generally smaller than 90^o and most cases fall into the first case in Eq. (6.16). Note that when $a = 0$, the FBPC formula reduces to the well-known FBP formula along straight lines.

6.3.2 Point Target Response and Resolution

It is difficult to exactly compute the resolution for FBP along curves, however we can make observations about the resolution using an approximation of the PTR.

6.3.2.1 Range Resolution

In this section, as one of the main results of this chapter, we present an approximation of the range resolution using the method of stationary phase [55]. Detailed derivation is presented in Appendix G.

Recall from Eq. (6.8) and Eq. (6.9) that the normalized PTR of a point scatterer at (x_0, y_0) is

$$\bar{h}(x,y;x_0,y_0) = \frac{1}{\rho_0\Delta\int f_2(x,y;\theta)d\theta}\left\{\int_{-\Theta/2}^{\Theta/2} f_2(x,y;\theta)\,\mathrm{sinc}(\Delta q_\theta)\,\mathrm{e}^{j\pi K\Delta q_\theta}\,d\theta\right.$$

[3] See Appendix F.2 for the derivation.

$$- j\frac{1}{\pi K}\int_{-\Theta/2}^{\Theta/2} f_2(x,y;\theta)\,\mathrm{dsinc}(\Delta q_\theta)\,\mathrm{e}^{j\pi K\Delta q_\theta}\,d\theta\Bigg\}. \tag{6.18}$$

The functions $f_2(x,y;\theta)$, $\mathrm{sinc}(\Delta q_\theta)$, and $\mathrm{dsinc}(\Delta q_\theta)$ are real valued and slowly varying over θ, and the offset ratio K is large in general. Thus, we can use the method of stationary phase to approximate the PTR. It can be shown that the dominant frequency θ_d, i.e. the stationary point of the phase function, satisfies

$$\tan\theta_d = \frac{1}{R}\left\{\frac{(y-y_0)\sqrt{(x_0+R)^2+(h(x_0,y_0)-H)^2}}{\sqrt{(x+R)^2+(h(x,y)-H)^2}-\sqrt{(x_0+R)^2+(h(x_0,y_0)-H)^2}} - y_0\right\}. \tag{6.19}$$

Then, we have

$$\begin{aligned} q_{\theta_d} &= r_{\theta_d}(x,y) - r_{\theta_d}(x_0,y_0) \\ &= \left\{\left(\sqrt{(x+R)^2+(h(x,y)-H)^2}-\sqrt{(x_0+R)^2+(h(x_0,y_0)-H)^2}\right)^2+(y-y_0)^2\right\}^{1/2}. \end{aligned} \tag{6.20}$$

Finally, by using the first-order Taylor series expansion of q_θ about $\theta=\theta_d$ and re-normalizing, the PTR can be approximated as

$$\left|\bar{h}(x,y;x_0,y_0)\right| \approx \left|\mathrm{sinc}(\Delta q_{\theta_d}) - j\frac{1}{\pi K}\mathrm{dsinc}(\Delta q_{\theta_d})\right| \tag{6.21}$$

for $|\theta_d| \le \Theta/2$.

Since θ_d is small for coordinates near the line defined by $y=y_0$, the above is a suitable approximation for describing the slice of the PTR in the range direction. By substituting $y=y_0$ in Eq. (6.21), we can make the following observations on the range resolution. First, the resolution is inversely proportional to Δ, the bandwidth of the spatial frequencies; this is analogous to the fact that range resolution relates inversely to range of frequencies employed for far-field imaging via PFA [28,42]. Second, the larger the frequency offset ratio K, the finer the resolution. Given a fixed bandwidth Δ, increasing K decreases the contribution of the imaginary term to the magnitude of the PTR. This in effect decreases the resolution.

Lastly, the resolution depends on q_θ, which in turn depends the geometry of the terrain in the neighborhood of the point scatterer. That is, the PTR slice is not simply a function of $x-x_0$, but is a function of

$$\sqrt{(x+R)^2+(h(x,y_0)-H)^2}-\sqrt{(x_0+R)^2+(h(x_0,y_0)-H)^2}, \tag{6.22}$$

the difference in the distances to the line of the radar flight path $\{(-R,y,H)|y\in\mathbb{R}\}$ from each of the two points $(x,y_0,h(x,y_0))$ and $(x_0,y_0,h(x_0,y_0))$. Thus, FBPC reconstruction can yield a

small value when there is a significant difference in elevation of the two points even if the range coordinates are close. This agrees with our intuition; we do not expect for the sidelobes of a point scatterer on the ground to equally affect equidistant (in the range direction) pixels with drastically different elevations, e.g. one that is on the ground and one that is at a high elevation. The above approximation suggests that in such cases the sidelobes at neighboring coordinates with larger elevation difference will be smaller than those on the ground. In the neighborhood (x, y_0) of (x_0, y_0), the above value further can be approximated as

$$\frac{(x_0 + R) + \frac{\partial h}{\partial x}(x_0, y_0)(h(x_0, y_0) - H)}{\sqrt{(x_0 + R)^2 + (h(x_0, y_0) - H)^2}}(x - x_0). \tag{6.23}$$

This indicates that even if the difference in elevation of the two points $h(x, y_0) - h(x_0, y_0)$, or similarly, the gradient $\frac{\partial h}{\partial x}(x_0, y_0)$, are the same, the resolution can depend heavily on radar flight paths. Also, point scatterers on the same flat terrain can have resolutions that differ drastically, depending on their range coordinates and elevations.

Under the far-field assumption, the dominant frequency θ_d from Eq. (6.19) satisfies

$$q_{\theta_d} = \frac{(x - x_0) - a(h(x, y) - h(x_0, y_0))}{\sqrt{1 + a^2}} \tag{6.24}$$

for $y = y_0$. From this formula, it becomes more clear how the topology near a point scatter and the radar grazing angle affect the range resolution. In particular, the resolution is finest when $a = \frac{h(x,y_0) - h(x_0,y_0)}{x - x_0}$ for locations satisfying $(h(x, y_0) - h(x_0, y_0))(x - x_0) > 0$.[4] That is, it is best to transmit pulses in the direction parallel to the terrain to achieve fine range resolution. The analysis agrees with the knowledge that a finer resolution is achieved when the radar flies at a low altitude for a flat and level terrain. This furthermore implies that we cannot form a high resolution image of a steep mountain slope from a side view.

The dependency of the range resolution on $a = H/R$ and the gradient of the terrain in the range direction is illustrated in Fig. 6.3. For simplicity, we show a flat terrain (marked with a blue line) with $h(x, y) = a_0 x$. When $a < -a_0$, as in Fig. 6.3(a), the radar pulse cannot illuminate the terrain and we are not able to reconstructed an image. We can produce images with a fine range resolution when a is slightly larger than $-a_0$, as in Fig. 6.3(b). The resolution becomes lower for larger values of a, as in Fig. 6.3(c).

This is also true when reconstructing an image using PFA; both warping the slant-plane image onto a steep DEM and projecting the slant-plane Fourier data onto a ground plane in Fourier domain result in poor resolution. The amount of increase in range resolution when the DEM is flat is

[4] For points with $(h(x, y_0) - h(x_0, y_0))(x - x_0) < 0$, the resolution becomes finer as a increases. However, this is not a case of interest since the radar pulses are not able to reach those points without penetrating the surface.

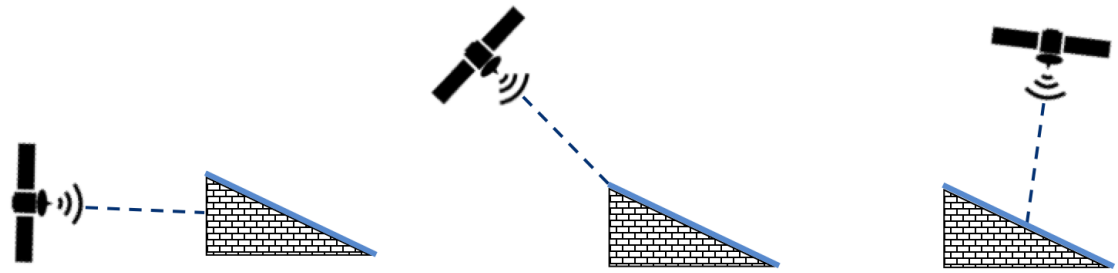

(a) No image (b) High-resolution image (c) Low-resolution image

Figure 6.3: The relationship between $a = H/R$ and the terrain gradient in the range direction and the resulting range resolution of the image.

given by cosine of the grazing angle, which is equivalent to $\sqrt{1+a^2}$ [6].

6.3.2.2 Cross-Range Resolution

An approximation of the cross-range resolution is more difficult to derive. However, we are able to derive an informative lower bound instead. When $d_\theta(x,y) - d_\theta(x_0,y_0) \ll d_\theta(x_0,y_0)$, i.e., considering points (x,y) in the neighborhood of the point scatterer location (x_0,y_0), we have

$$q_\theta \approx \frac{y_0 + R\tan\theta}{\sqrt{S^2(x_0,y_0) + (y_0 + R\tan\theta)^2}}(y - y_0) + \frac{1}{2}\frac{S^2(x,y) - S^2(x_0,y_0)}{\sqrt{S^2(x_0,y_0) + (y_0 + R\tan\theta)^2}}, \tag{6.25}$$

where $S(x,y) = \sqrt{(x+R)^2 + (h(x,y) - H)^2}$. We particularly are interested in the PTR on a curve defined by $S(x,y) = S(x_0,y_0)$, which is a line passing the point target location in the cross-range direction in case of flat terrain. Note that the normalized PTR can be written as

$$\bar{h}(x,y;x_0,y_0) = \frac{1}{\rho_0 \Delta \int f_2(x,y;\theta)d\theta} \int_{-\Theta/2}^{\Theta/2} \int_{\rho_0-\Delta/2}^{\rho_0+\Delta/2} \rho f_2(x,y;\theta)\, \mathrm{e}^{j2\pi q_\theta \rho}\, d\rho d\theta. \tag{6.26}$$

Since the resolution of the image formed from superposition of frequency components cannot be finer than half the inverse of the maximum spatial frequency employed [56], a lower bound on the cross-range resolution is given by[5]

$$\frac{\sqrt{S^2(x_0,y_0) + (y_0 + R\tan(\Theta/2))^2}}{4(\rho_0 + \Delta/2)|y_0 + R\tan(\Theta/2)|}. \tag{6.27}$$

Under the far field assumption and for most ranges of look angles satisfying $\tan^2(\Theta/2) \ll 1 + a^2$,

[5]The function $\frac{y_0 + R\tan\theta}{\sqrt{S^2(x_0,y_0) + (y_0 + R\tan\theta)^2}}$ is an increasing function on $[0, \Theta/2]$.

this bound reduces to $\sqrt{1+a^2}/(2(K+1)\Delta\tan(\Theta/2))$. The bound further simplifies to $\sqrt{1+a^2}/(2\Delta)$ (same as the range resolution) when $(K+1)\tan(\Theta/2) = 1$[6]. In [35], the resolution for BFA was computed assuming a purely sinusoidal source, and was given by $\lambda\sqrt{1+a^2}/(4\tan(\Theta/2))$, where λ is the wavelength of the source signal. Note that this last formula is very close to the above lower bound for large values of K.

6.3.3 Simulation of Point Target Responses

For all the simulations in this chapter, we choose the spatial frequency bandwidth to be $\Delta = 1$ so that the point target resolutions are close to one meter in idealistic scenarios. The value of the frequency offset ratio K does not have a significant impact on the PTRs and is fixed at $K = 10$. The horizontal and vertical coordinates of the figures to be presented correspond to the range and cross-range coordinates, respectively.

In the following, we show simulation results of PTRs by varying some of the key parameters that affects the resolution as discussed in Sec. 6.3.2. Each scene is composed of nine equal-strength point scatterers to clearly show the spatially variant PTRs at different point target locations. The range and cross-range coordinates of the point scatterers are both equal to -10, 0, and 10, and the images are shown on a small patch of size 30×30.

6.3.3.1 The Effect of Wavefront Curvature

Figure 6.4 shows the FBPC reconstructions of point scatterers on a flat level terrain with zero elevation for different standoff ranges R and elevations H of the radar. All point scatters are correctly centered at their respective locations indicated by the faint dotted lines. Comparing Fig. 6.4(a) and Fig. 6.4(c) or, similarly, Fig. 6.4(b) and Fig. 6.4(d), we can see that a smaller standoff range introduces a noticeable effect on the PTRs, due to wavefront curvature. These effects are most apparent in the PTRs centered at nonzero cross-range coordinates, as the mainlobes are tilted and the sidelobes are curved. Also, the cross-range resolution is larger for the point reflectors that are further from the radar, i.e. for larger range coordinates. The aforementioned effects are explained in Appendix E. For a fixed standoff range R, increasing the elevation of the radar, or equivalently, increasing the grazing angle, lowers the resolution. This is shown in Fig. 6.4(a) and Fig. 6.4(b) and, similarly, in Fig. 6.4(c) and Fig. 6.4(d). Each pair of figures has a fixed R, and the PTRs with the larger grazing angle have noticeably wider mainlobes. The increase in image entropies further suggest the lower resolution.

[6]We used the relationship $(K-1)\tan(\Theta/2) = 1$ for 2-D SAR imaging in Sec. 5.4 to achieve nearly equal range and cross-range resolutions.

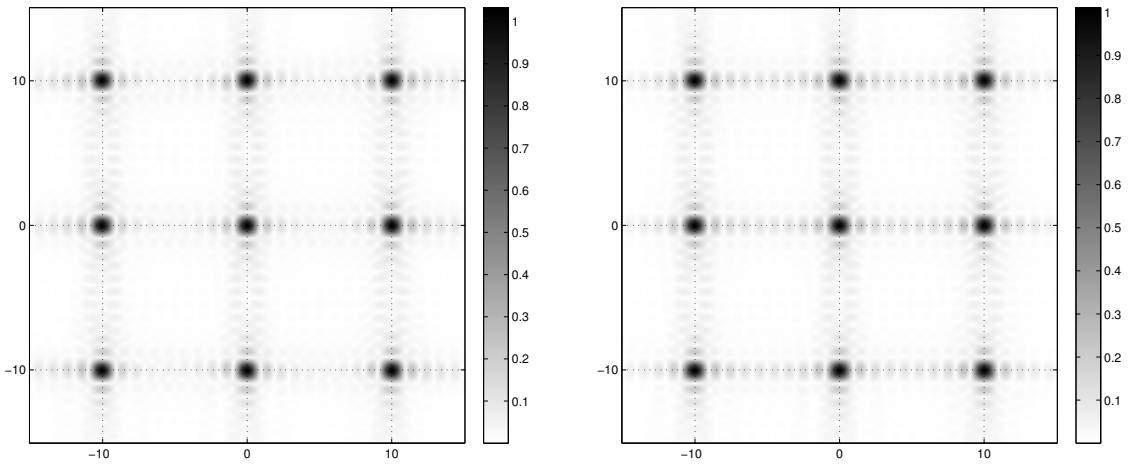

(a) $R = 500, H = 10$ (b) $R = 500, H = 50$

(c) $R = 100, H = 10$ (d) $R = 100, H = 50$

Figure 6.4: Effect of wavefront curvature. The point scatterers are on flat, level terrain with zero elevation are shown for different standoff ranges and elevations of the radar. The image entropies are: (a) 7.7208, (b) 7.7843, (c) 7.7773, and (d) 7.9624.

6.3.3.2 The Effect of Terrain Gradient

In the following set of simulations, we assume non-level flat terrain modeled by $h(x,y) = a_0 x + b_0 y$ for a radar flight path with $R = 500$ and $H = 50$. In order to isolate the effects of terrain gradients of each direction, we show the PTRs in two separate figures; one with a fixed b_0 and varying a_0, and another with a fixed a_0 and varying b_0.

Figure 6.5 shows the effect of a gradient in the range direction. Figure 6.5(a) is an example of the terrain for $a_0 = 0.5$, and the other four figures show how the PTRs change as the gradient increases. As noted in Sec. 6.3.2, the best range resolution is achieved when $a_0 = -a = -H/R = -0.1$. The PTRs for $a_0 = -0.1$ in Fig. 6.5(b) are correctly located at their relative locations and

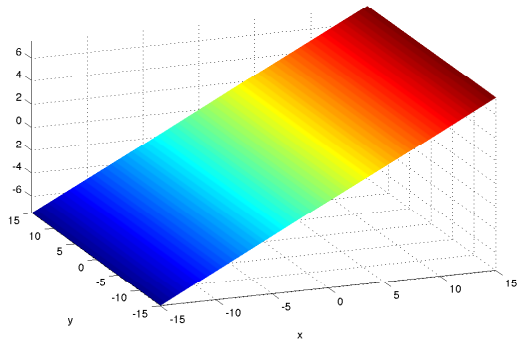

(a) DEM example: $h(x,y) = 0.5x$

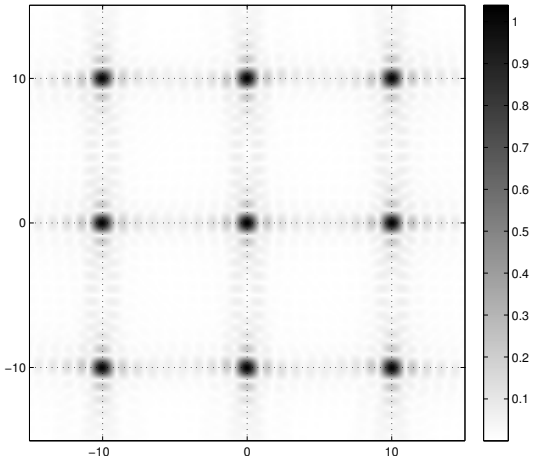

(b) $a_0 = -0.1$

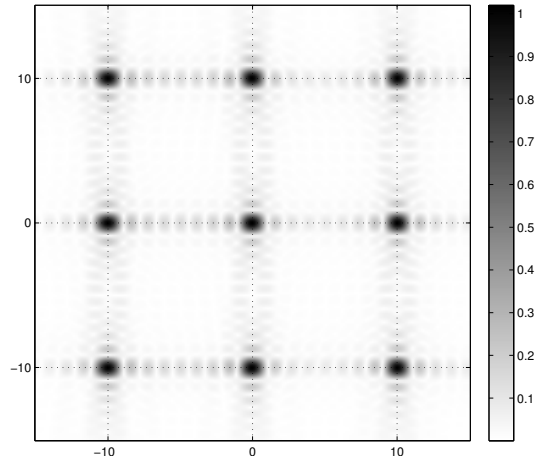

(c) $a_0 = 1$

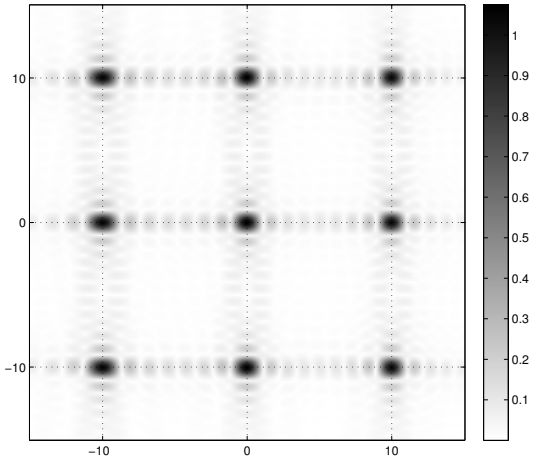

(d) $a_0 = 2$

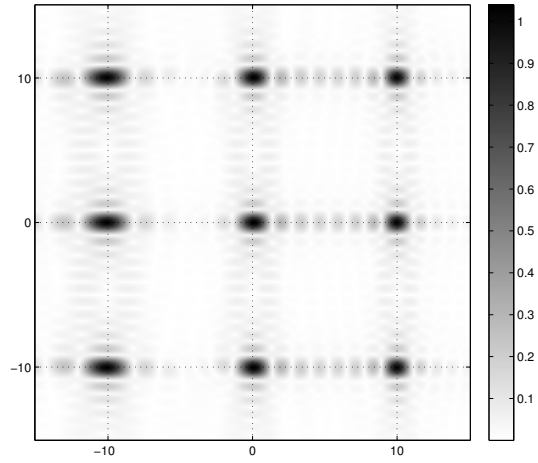

(e) $a_0 = 3$

Figure 6.5: The effect of terrain gradient in the range direction. (a) An example of non-level flat terrain defined by $h(x,y) = a_0 x$ with $a_0 = 0.5$. Figures (b) to (e) plot PTRs for different values of a_0. Entropies are: (b) 7.7487, (c) 7.8650, (d) 7.9413, and (e) 8.0761.

have the same shape and resolution at all nine different locations. Figures 6.5(c), 6.5(d), and 6.5(e) show that the mainlobes of the PTRs widen with steeper slope. We expect the same results with a fixed gradient and increase in flight elevation. Note that the cross-range resolution is not affected as much by the range gradient.

Equation (6.23) indicates that the PTR stretches out in the range direction by a factor of

$$\frac{\sqrt{1+a_0^2}\sqrt{(500+x_0)^2+(a_0x_0-50)^2}}{\sqrt{1+a^2}\sqrt{500+x_0)+a_0(a_0x_0-50)}},$$

compared to the PTR for $a_0 = -a$. Thus, the mainlobes not only widen as a_0 increases, but also as the range coordinate of the point scatterer decreases. The relative amount of stretch computed from the formula above are shown in Table 6.1. Rows 2 and 3 correspond to the PTR at $x_0 = -10$ and rows 4 and 5 correspond to the PTR at $x_0 = 10$. Each value in the table is a percentage representing the relative amounts of stretch with respect to some reference PTR. For rows 2 and 4 the references are the PTRs at $x_0 = 0$ on the same slope, and for rows 3 and 5 the references are the PTRs on the terrain with $a_0 = -0.1$, i.e. Fig. 6.5(b). For example, the last entry of row 2 suggests that the PTRs in Fig. 6.5(e) at $x_0 = -10$ are stretched by 138.33% when compared with those at $x_0 = 0$ in the same figure. Additionally, the last entry of row 3 suggests that these same PTRs are stretched by 435.26% when compared with those in Fig. 6.5(b).

Table 6.1: Relative amount of stretch of PTRs (in percentage) for different terrain gradients (in the range direction). Radar flight path is at standoff range $R = 500$ and elevation $H = 50$.

a_0	-0.1	0.1	0.2	0.5	1	2	3
PTR for $x_0 = -10$	100	100.08	100.19	100.78	102.81	112.58	138.33
(relative to PTR for $a_0 = -0.1$)	100	100.08	101.66	112.11	144.68	250.48	435.26
PTR for $x_0 = 10$	100	99.92	99.82	99.26	97.47	90.37	79.00
(relative to PTR for $a_0 = -0.1$)	100	99.92	101.30	110.44	137.16	201.08	248.58

Figure 6.6 shows the effect of a gradient in the cross-range direction. Figure 6.6(a) is an example of terrain for $b_0 = -0.2$, and all other four figures show how the PTRs change as the gradient increases. The gradient of the terrain in the cross-range direction does not affect the resolution as much as the gradient across the range direction. However, the PTRs become noticeably tilted for steep cross-range gradients. The tilt in the PTRs occurs because the backprojection smears the data along equidistant arcs. This means that the points on the DEM that are at lower elevations than the point target (hence further from the radar) are smeared closer to the radar in $x-y$ coordinates. In other words, the increase in elevation distance is compensated by a decrease in $x-y$ distance,

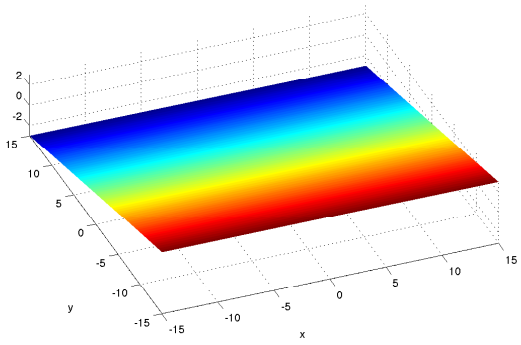

(a) DEM example: $h(x,y) = -0.2y$

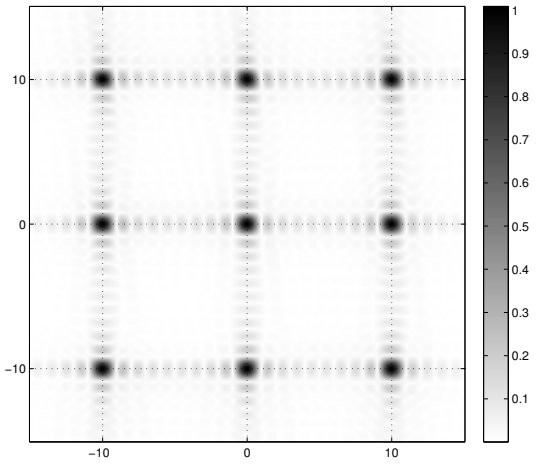

(b) $b_0 = -0.1$

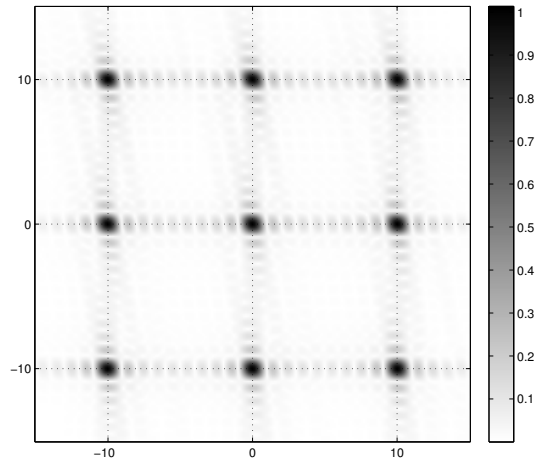

(c) $b_0 = -1$

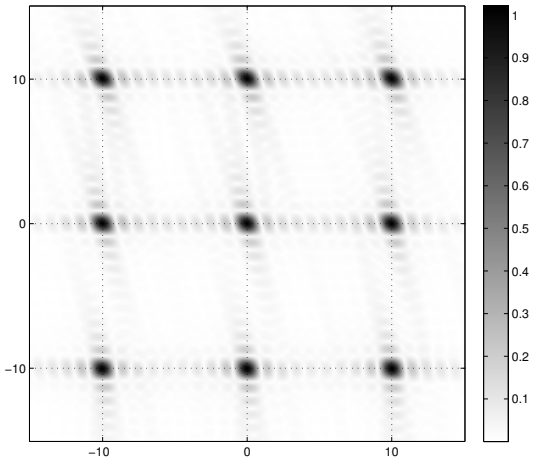

(d) $b_0 = -2$

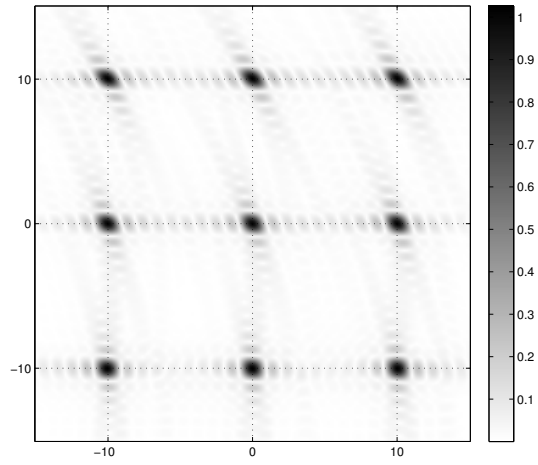

(e) $b_0 = -3$

Figure 6.6: The effect of a terrain gradient in the cross-range direction. (a) An example of non-level flat terrain defined by $h(x,y) = b_0 y$ with $b_0 = -0.2$. Figures (b) to (e) plot PTRs for different values of b_0. Entropies are: (b) 7.7525, (c) 7.7769, (d) 7.7576, and (e) 7.7663.

which in effect steers the equidistant arc towards the radar. For similar reasons, the points that are at higher elevations than the point target (hence closer to the radar) appear to be smeared away from the radar in $x-y$ coordinates. Figure 6.7 shows the contours of the PTRs associated with Fig. 6.5 and Fig. 6.6.

6.3.3.3 Importance of the DEM

Figure 6.8 shows the reconstruction of point targets at different levels of elevation, where the radar flight path is described by $R = 500$ and $H = 20$. The elevation for a point target at location (x, y) is modeled by $\epsilon h_p(x, y)$, where ϵ is a constant and h_p is shown in Fig. 6.8(a). Figures 6.8(b) to 6.8(f) are collections of nine separate 10×10 tiles of PTRs, where the dotted lines indicate the borders of individual tiles and the terrain is assumed to be flat and level in the vicinity of each point target location. In other words, each tile represents a PTR of a single point target on a DEM with a constant elevation.

The images of PTRs in the left column of Fig. 6.8 are reconstructed using the correct DEM, whereas the images in the right column of Fig. 6.8 are reconstructed assuming the DEM is on the ground plane. All PTRs have similar resolution regardless of the elevation of point targets and knowledge of the DEM, and the reconstructions employing the correct DEM successfully position the point targets in the correct locations for all values of ϵ. By contrast, the PTRs reconstructed with unknown or erroneous DEMs suffer from incorrect locations. Exceptions are the PTRs on the anti-diagonal tiles because the DEM for these tiles have zero elevation. The point scatterers at above zero elevation are shifted to the left (toward the radar) and the point scatterers below zero elevation are shifted to the right (away from the radar). This phenomenon is referred to as the layover effect. Note that the PTRs are displaced only along the range direction and the amount of displacement nearly proportional to ϵ.

The layover effect can be explained using the illustration in Fig. 6.9. The black dot represents an elevated reflector at a distance d_0 from the radar. Since the radar is not aware that the backscatter came from an elevated target, it assumes that the energy came from a point on the ground (marked with the blue dot in Fig. 6.9) at distance d_0 from the radar. Thus, the reflector appears at a wrong location in the reconstructed image.

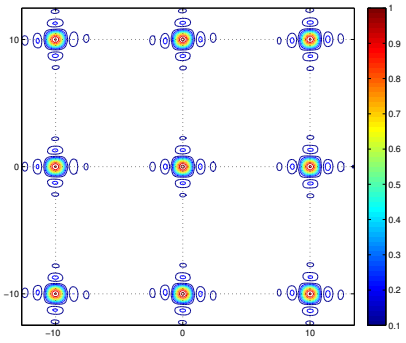

(a) $a_0 = -0.1, b_0 = 0$

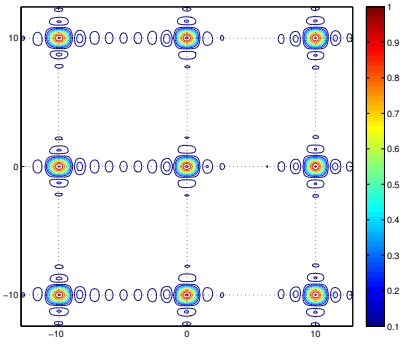

(b) $a_0 = 1, b_0 = 0$

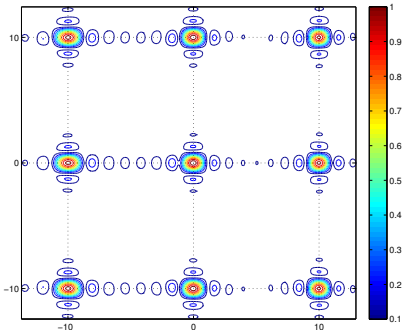

(c) $a_0 = 2, b_0 = 0$

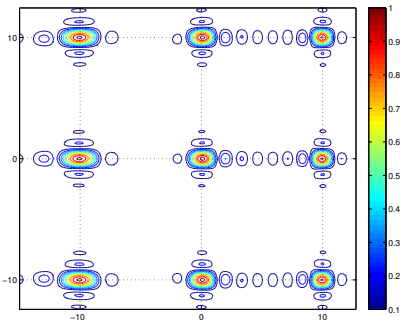

(d) $a_0 = 3, b_0 = 0$

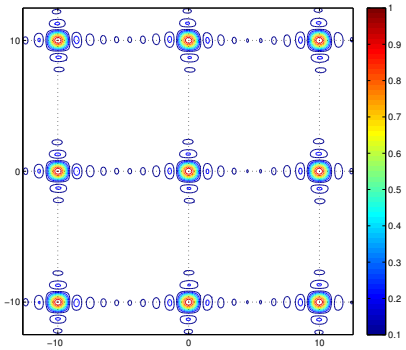

(e) $a_0 = 0, b_0 = -0.1$

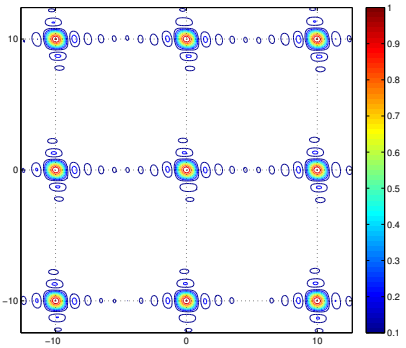

(f) $a_0 = 0, b_0 = -1$

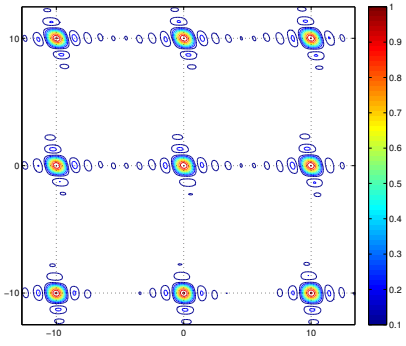

(g) $a_0 = 0, b_0 = -2$

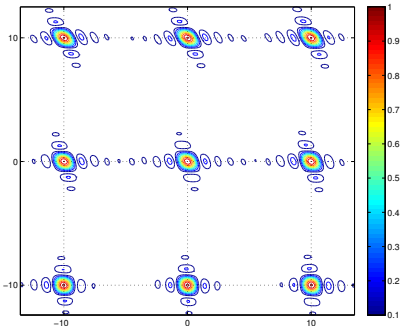

(h) $a_0 = 0, b_0 = -3$

Figure 6.7: Contour plots of data in Fig. 6.5 and Fig. 6.6. (a) to (d) correspond to (b) to (e) in Fig. 6.5 and (e) to (h) correspond to (b) to (e) in Fig. 6.6.

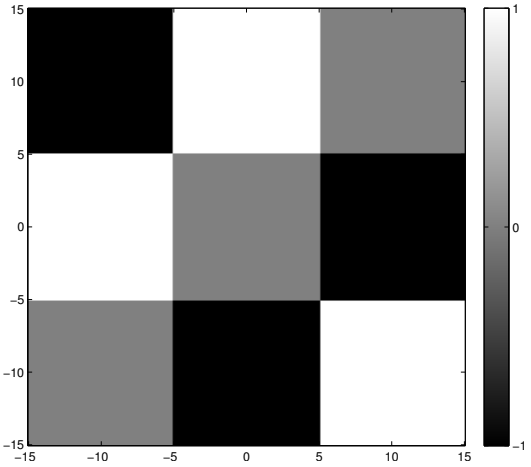

(a) $h_p(x, y)$

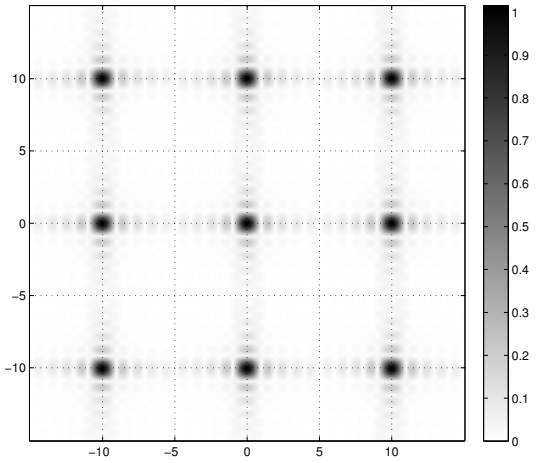

(b) Image on DEM $\epsilon = 5$

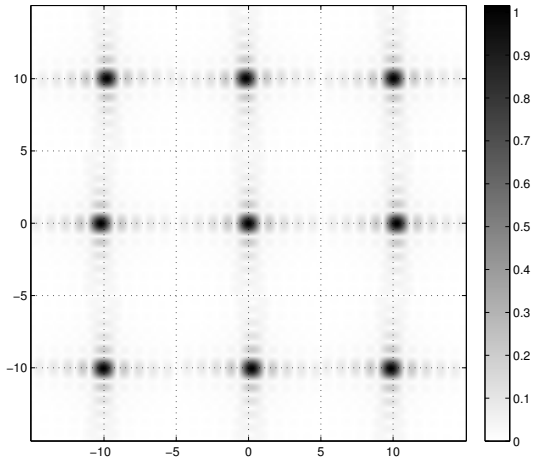

(c) Ground-plane image $\epsilon = 5$

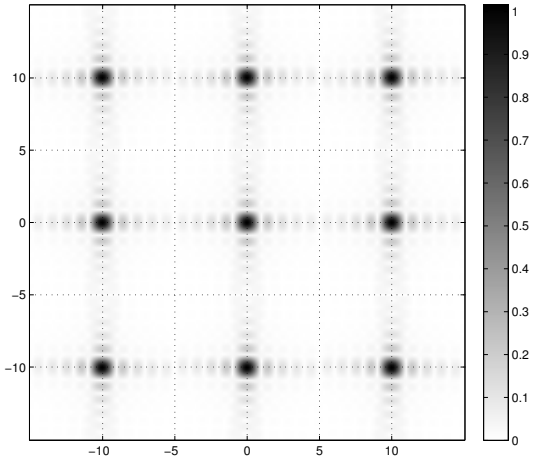

(d) Image on DEM $\epsilon = 20$

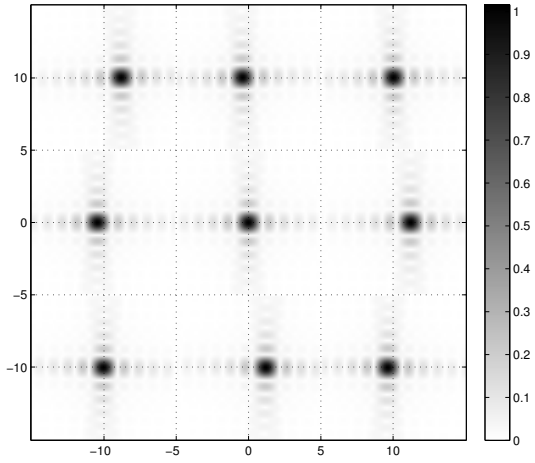

(e) Ground-plane image $\epsilon = 20$

Figure 6.8: Simulation of elevated point targets for different levels of elevation. The elevation is modeled by $\epsilon h_p(x, y)$, where the function h_p is shown in (a). (c) and (e) are reconstructed using the correct DEM and (b), (d), and (f) are reconstructed without the knowledge of elevation.

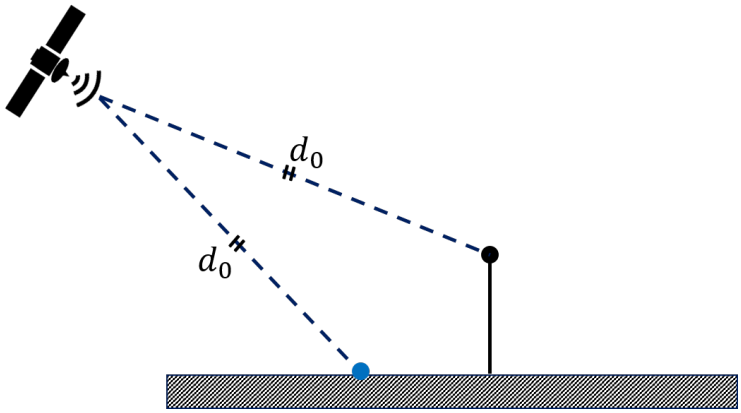

Figure 6.9: Illustration of the layover effect. The black dot represents an elevated reflector and the blue dot represents the shifted location of the reflector in an image reconstructed without the DEM.

6.3.4 Simulation of a Realistic SAR Scene

6.3.4.1 Simulation Setting

For a more realistic terrain model, we define the Gaussian DEM

$$h_G(x,y) = A_{\text{G}} \exp\left\{-\frac{(x-x_{0\text{G}})^2}{2\sigma_x^2} - \frac{(y-y_{0\text{G}})^2}{2\sigma_y^2}\right\} - C_G. \tag{6.28}$$

The DEM has the maximum elevation A_{G} at $(x_{0\text{G}}, y_{0\text{G}})$, and σ_x and σ_y determine the range and cross-range dimension, respectively, of the elevated region near $(x_{0\text{G}}, y_{0\text{G}})$. C_G is a constant that ensures $h_G(0,0) = 0$ without loss of generality. We adopt the Gaussian DEM as it has several favorable characteristics that simplify the formula of FBPC. Additionally, with Gaussian DEM it is simple to analyze whether a point on the DEM can be imaged or not with non-penetrating radars.

Consider a Gaussian DEM with the parameters $A_{\text{G}} = 30$, $\sigma_x = 50$, $\sigma_y = 40$, and $(x_{0\text{G}}, y_{0\text{G}}) = (60, -50)$. The contours of the DEM are shown in Fig. 6.10(a) and the contours of the gradient of the DEM in the range direction are shown in Fig. 6.10(b). The flight path of the radar should be chosen so that all points on the DEM can be imaged without obscuration. For this example, the maximum elevation is at $(60, -50)$, which is in the lower right corner of the image patch of size 128×128, and the gradients of the DEM in the range direction are positive for most points. As a result, all points on the terrain should be visible from the radar flight path when the elevation of the radar is fairly high.

Figure 6.10(c) shows a SAR image obtained from Sandia National Laboratories [25] that is used to model the magnitude of the scene reflectivity. Although we only image the magnitude of the reflectivities, note that we added uniformly random spatial phases to model the complex-valued reflectivities when synthesizing the SAR data. Finally, Fig. 6.10(d) shows the same image on the

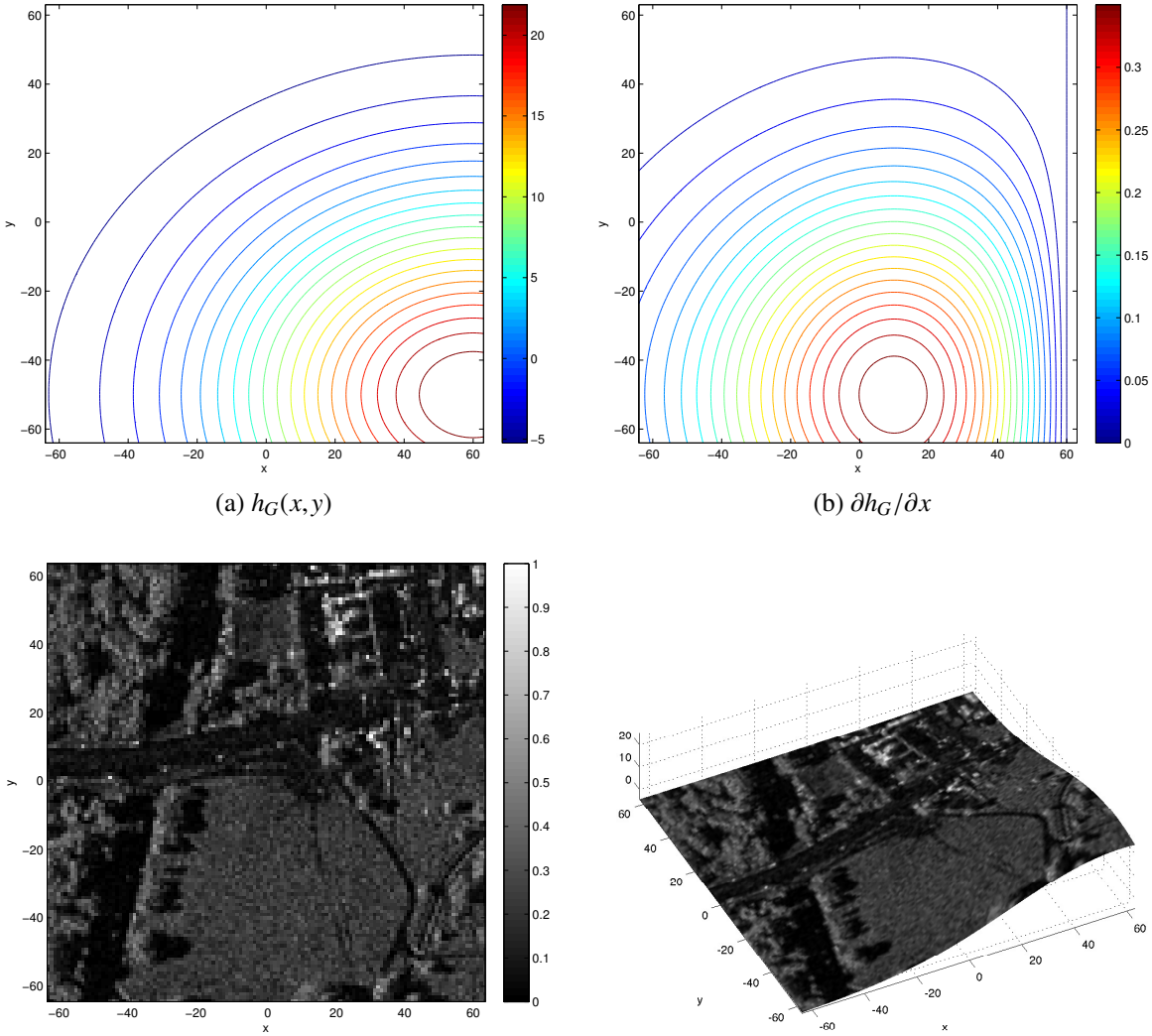

(a) $h_G(x,y)$ (b) $\partial h_G/\partial x$

(c) SAR image (d) SAR image on the terrain

Figure 6.10: An example of a Gaussian DEM and the SAR image used to model the reflectivity. (a) Contours of the Gaussian DEM and (b) contours of the terrain gradient in the range direction. The parameters for the Gaussian DEM are $A_{\mathrm{G}} = 30$, $\sigma_x = 50$, $\sigma_y = 40$, and $(x_{0\mathrm{G}}, y_{0\mathrm{G}}) = (60, -50)$. (c) is a 128×128 SAR image and (d) is the same image shown on the assumed terrain.

Gaussian terrain in 3-D space.

6.3.4.2 Simulation of FBPC

Figure 6.11 shows simulation results of FBPC for three different radar flight paths. Figures 6.11(a), 6.11(c), and 6.11(e) are the FBPC reconstructions for $R = 1000$ and $H = 50$, $R = 200$ and $H = 10$, and $R = 1000$ and $H = 400$, respectively. Figures 6.11(b), 6.11(d), and 6.11(f) show the errors in the reconstructions on a reverse colormap. Figure 6.11(a) is imaged from a fairly long distance

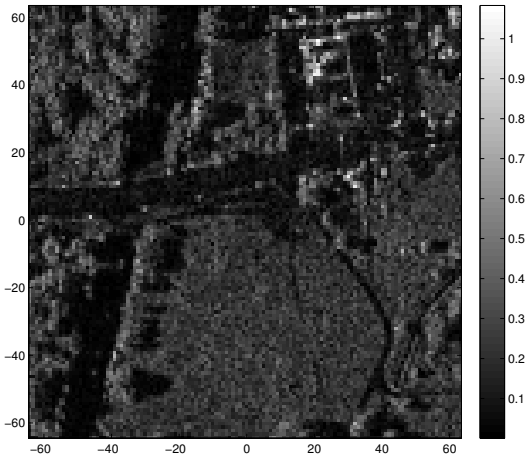

(a) FBPC for $R = 1000$ and $H = 50$

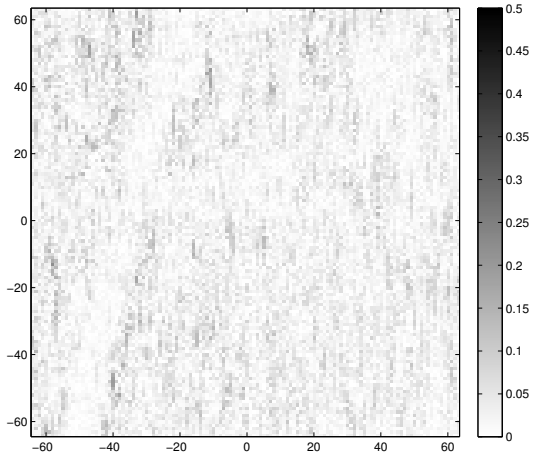

(b) Error in (a)

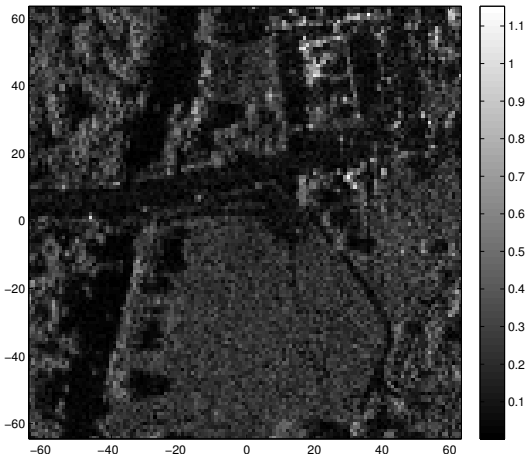

(c) FBPC for $R = 200$ and $H = 10$

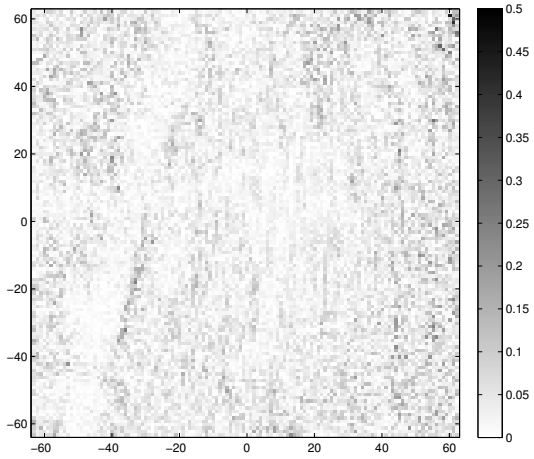

(d) Error in (c)

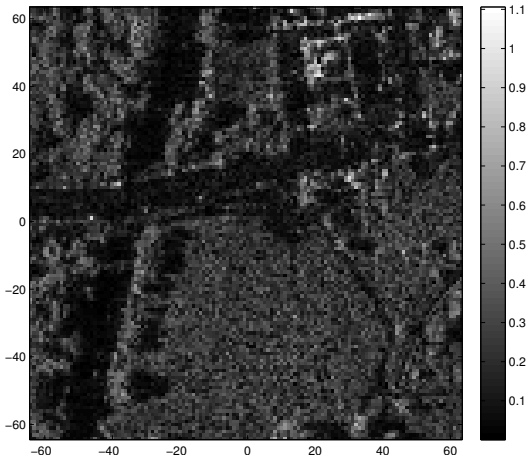

(e) FBPC for $R = 1000$ and $H = 400$

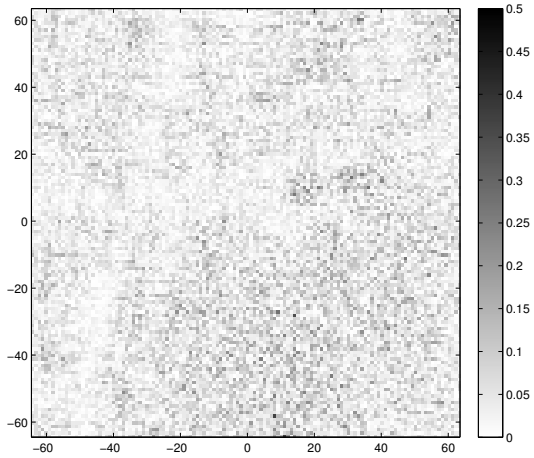

(f) Error in (e)

Figure 6.11: FBPC reconstruction and the reconstruction errors for different radar flight paths. RMSEs are: (a) 0.0386, (c) 0.0506, and (e) 0.0589. The maximum absolute errors are: (b) 0.221, (d) 0.372, and (f) 0.438.

and at a low grazing angle, and the reconstruction resembles the true reflectivity. The RMSE is less than 4% of the maximum reflectivity value, and the errors are spread out in the entire image, excluding the region of low reflectivity values. The error plot does not show any other specific behavior.

Figure 6.11(c) is imaged in a near-field scenario (at the same grazing angle as in Fig. 6.11(a)). The reconstruction itself looks similar to the true image, however, the error plot and the Root-Mean-Squared Error (RMSE) value suggest otherwise. Due to the significant amount of wavefront curvature, the degradation in resolution and the distortion of sidelobes induce large errors at the long ranges on the DEM. That is, the errors are most prominent at the right side of the image, as it can be seen in Fig. 6.11(d). Note that RMSE and the maximum error have increased 30% and 68%, respectively, as the distance between the radar and the scene has been reduced by 80%.

Figure 6.11(e) is imaged at a high grazing angle from a fairly long distance. RMSE and the maximum error have increased 53% and 98%, respectively, compared to Fig. 6.11(a), as the elevation of the radar increased to 400 from 50. The reconstruction is noisy in the lower half region of the image, which can be seen in both Fig. 6.11(e) and Fig. 6.11(f). The region of high error coincides with the region with steep slope in the range direction, which can be identified from Fig. 6.10(b). As both high grazing angle and high terrain gradient are detrimental to achieving optimal resolution, the reconstruction is expected to be erroneous. The right side of the image, which corresponds to a low terrain gradient, has relatively small errors.

Figure 6.12 shows simulation results of FBPC for $R = 1000$ and $H = 200$. Figures 6.12(a) and 6.12(b) correspond to reconstruction on the DEM and reconstruction on the ground plane. Without the knowledge of the DEM, the quality of the reconstruction is noticeably degraded. The scatterers with non-zero elevation are displaced in the range direction in an amount proportional to their elevation, and neighboring scatterers with different displacements and uncorrelated spatial phases interfere with each other to produce a more speckle image with a lower resolution than the correctly reconstructed image. Thus, Fig. 6.12(b) is not merely a warped version of Fig. 6.12(a).

On a larger scale, prominent structures on the terrain with high elevation appear shifted from their correct locations. This is shown more clearly in Fig. 6.12(c) and Fig. 6.12(d), where each shows a lower-right subregion of the reconstruction above it. The thin dark curve in the orthographically correct reconstruction meets with the red line described by $x = 43$, however, the curve is shifted to the left from its correct location and does not cross the red line in Fig. 6.12(d). Here, the structures in the subregion are shifted to the left because the terrain of the subregion is above zero elevation. Note that the pixels in the right column of Fig. 6.12(d) have near-zero values also because of the shift.

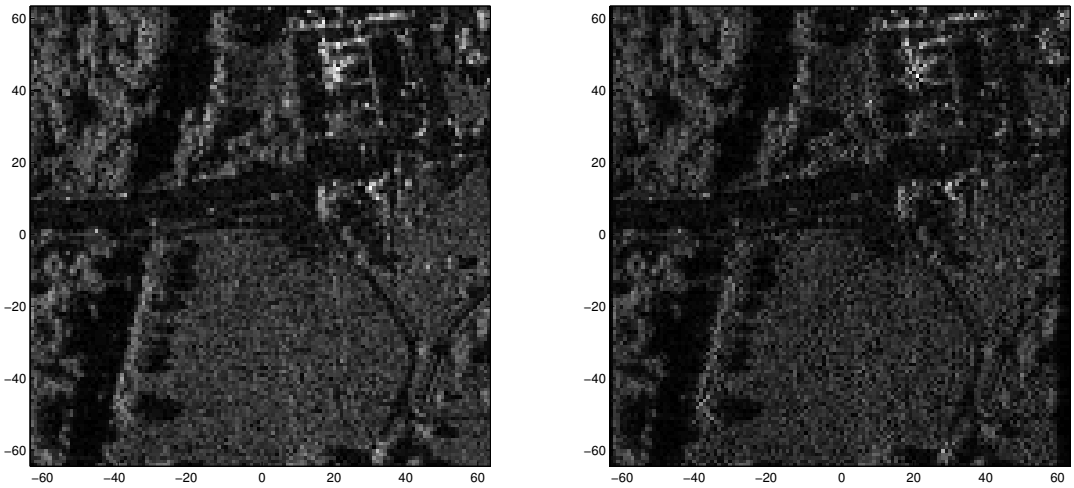

(a) Reconstruction on the DEM

(b) Reconstruction on the ground plane

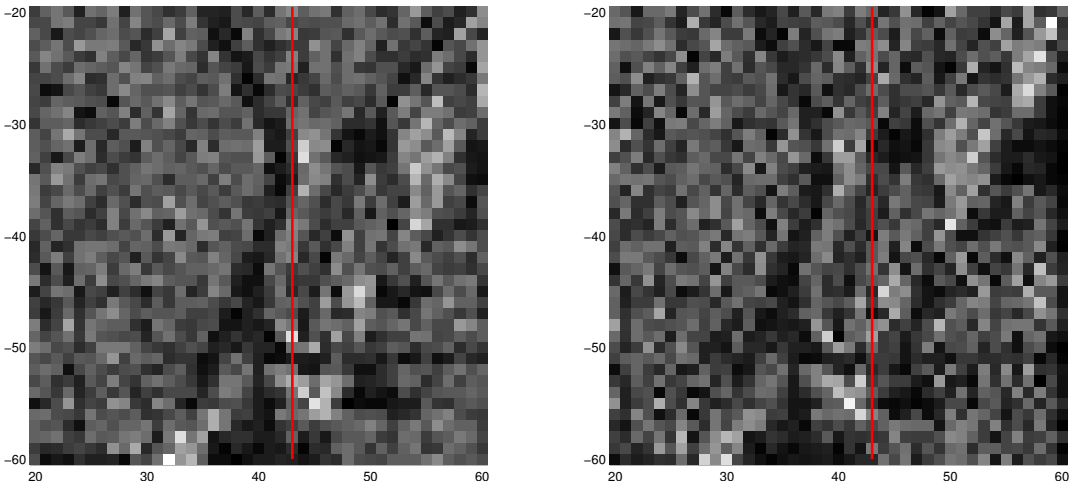

(c) Subregion of (a)

(d) Subregion of (b)

Figure 6.12: FBPC and the knowledge of DEM. (a) and (b) are images reconstructed with and without knowledge of the DEM, respectively, and (c) and (d) are the subregions in the lower right corner of (a) and (b), respectively. The red line in (c) and (d) corresponds to $x = 43$. RMSE of the reconstructions are (a) 0.0460 and (b) 0.1150.

6.4 Multichannel Autofocus Using a DEM

In this section, we consider the SAR defocusing problem and propose a linear-algebraic solution to the problem for scenes on a non-flat terrain.

6.4.1 MCA Approach for Focusing Image on a Known DEM

MCA was originally developed to solve the defocusing problem for the case of far-field imaging, but we extended the linear-algebraic approach in our preliminary work [43] for near-field imaging with flat topography. Since the low-return assumption is satisfied regardless of the particular imag-

ing scenario, the same approach also can be used for an arbitrary terrain. Importantly, the extension of MCA to incorporate near-field imaging with a known DEM is, in principle, straightforward due to the linear relationship between the SAR data and the recovered image via FBPC. That is, the defocused image can be modeled as a collection of multichannel outputs from the same unknown input: the phase errors. This allows us to form a linear solution space similar to how it is formed in the far-field imaging scenario.

In the previous section, the imaging algorithm was analyzed in the continuous domain for simplicity, but the actual SAR data are sampled and processed digitally. That is, the SAR data $P_\theta(\rho)$ are sampled at $\rho = \rho_k$, $k = 1, \ldots, N_\rho$, over a finite set of look angles $\theta = \theta_l$, $l = 1, \ldots, N_\theta$. We denote the discrete set of samples by $\{P[l,k]\}$, where $P[l,k] = P_{\theta_l}(\rho_k)$. In the following, we use bold capital letters and bold lower-case letters to denote matrices and vectors, respectively. For example, $\mathbf{P} \in \mathbb{C}^{N_\theta \times N_\rho}$ is the matrix representation of the demodulated data $\{P[l,k]\}$. The phase errors are denoted by $\boldsymbol{\phi} \in [-\pi, \pi)^{N_\theta}$, where ϕ_l is the phase error associated with look angle θ_l. Then, the demodulated data corrupted with phase errors are related to the error-free data by

$$\tilde{P}[l,k] = P[l,k]\, \mathrm{e}^{j\phi_l}. \tag{6.29}$$

Suppose that the estimates of the phase errors $\hat{\boldsymbol{\phi}} \in [-\pi, \pi)^{N_\theta}$ are used to correct the erroneous data. Then, the reflectivity value computed for coordinate $(x, y, h(x,y))$ from the corrected data can be written as

$$\hat{g}(x,y) = \boldsymbol{\Phi}_{(x,y)} \mathbf{e}^{-j\hat{\boldsymbol{\phi}}}. \tag{6.30}$$

Here, $\boldsymbol{\Phi}_{(x,y)} \in \mathbb{C}^{1 \times N_\theta}$ is a row vector, whose l-th entry is

$$\boldsymbol{\Phi}^{(l)}_{(x,y)} = \left\{ \rho_0 (N_\rho - 1) \sum_{l=1}^{N_\theta} f_2(x,y;\theta_l) \right\}^{-1} \sum_{k=1}^{N_\rho} \rho_k \tilde{P}[l,k]\, \mathrm{e}^{j2\pi r_{\theta_l}(x,y)\rho_k}, \tag{6.31}$$

and $\mathbf{e}^{-j\hat{\boldsymbol{\phi}}} \in \mathbb{C}^{N_\theta \times 1}$ is a column vector composed of $\mathrm{e}^{-j\phi_l}$'s.

Let $\mathcal{S} = \{(x_1, y_1), (x_2, y_2), \ldots, (x_{|\mathcal{S}|}, y_{|\mathcal{S}|})\}$ be a set of low-return coordinates that satisfy

$$\hat{g}(x,y) \approx 0, \quad \forall\, (x,y) \in \mathcal{S}. \tag{6.32}$$

The samples of the autofocused image that correspond to the presumed low-return region can be concatenated into a vector to form

$$\hat{\mathbf{g}}_{\mathcal{S}} = \boldsymbol{\Phi}_{\mathcal{S}}\, \mathbf{e}^{-j\hat{\boldsymbol{\phi}}}, \tag{6.33}$$

where $\boldsymbol{\Phi}_{\mathcal{S}}$ is a $|\mathcal{S}|$-by-N_θ matrix, whose n-th row is $\boldsymbol{\Phi}_{(x_n, y_n)}$. MCA aims to find phase error estimates that minimize the energy in the presumed low-return region, i.e., $\|\hat{\mathbf{g}}_{\mathcal{S}}\|_2$. By relaxing the all-pass

condition, MCA estimates the phase errors by

$$\hat{\boldsymbol{\phi}}^{*} = -\angle \left\{ \text{argmin}_{\|\mathbf{v}\|_2=1} \|\boldsymbol{\Phi}_{\mathcal{S}}\, \mathbf{v}\|_2 \right\}. \tag{6.34}$$

The solution to the optimization problem is the right singular vector of $\boldsymbol{\Phi}_{\mathcal{S}}$ corresponding to its smallest singular value.

The set of low-return coordinates used in MCA has a critical effect on the performance of MCA. However, little is known about how to identify the optimal set of low-return constraints. At least N_θ coordinates are needed for $\mathcal{S}$, however, a much larger size for $\mathcal{S}$ than the minimum required N_θ is often desired for good restoration results. Also, it is known that non-zero reconstruction values in the presumed low-return region of the perfectly focused image deteriorate the performance of MCA. One advantage over the original formulation of MCA is that the low-return coordinates do not have to be among the coordinates of the image you wish to reconstruct. The coordinates corresponding to the nulls of the antenna footprint can be used as idealistic low-return constraints. Note that in addition to the low-return region provided by the attenuation of the antenna footprint, a low-return region can be formed at points where an obstruction is on the line of sight to the radar.

The extension of MCA has several advantages over other autofocus approaches. First, the autofocus process remains a one-step computation since it directly uses the DEM in constructing the matrix $\boldsymbol{\Phi}_{\mathcal{S}}$. Although the construction of $\boldsymbol{\Phi}_{\mathcal{S}}$ requires more computation time due to the spatially variant filter f_2, it does not increase the order of computational complexity of MCA. Second, extended MCA approach does not make any further assumption aside from the approximation made in the development of FBPC. Thus, the performance is expected to be similar to that of the original MCA for scenarios in which FBPC works effectively. Accordingly, the performance of MCA is expected to degrade in the challenging cases discussed in the previous section where the quality of FBPC reconstruction was relatively poor. Such performance degradation is a result of the data collection geometry of challenging scenarios and will not be relieved by using other autofocus algorithms. Lastly, extended MCA is not iterative nor heuristic, and does not depend on the nature of phase errors.

Extended MCA for far-field applications yields the same solution as FMCA [33] using a 2-D periodic sinc interpolation kernel.[7] Since FMCA is equivalent to the original MCA when the SAR data are collected on a Cartesian grid [33], extended MCA truly is an extended version of the original MCA. It is applicable for near-field imaging, non-flat terrain, and works with any data collection grid in the Fourier domain. Note that it was shown earlier in [37] that PFA reconstruction is equivalent to FBP reconstruction when using the 2-D periodic sinc kernel with Jacobian weighting. The 2-D periodic sinc kernel may not be an optimal interpolation kernel. Thus, it is

[7] See Appendix H.

possible that the performance of PFA and FMCA may be better than that of FBP and extended MCA for far-field imaging with a different (better) interpolation kernel.

6.4.2 Simulations of Extended MCA

In this section, we present simulation results of the proposed autofocus algorithm. For simplicity, we model the ground terrain as having a Gaussian DEM, and the antenna pattern by a circular sinc function. Figure 6.13(a) shows the antenna footprint overlaid over an example Gaussian DEM with parameters $A_{\text{G}} = 20$, $\sigma_x = \sigma_y = 30$, and $(x_{0\text{G}}, y_{0\text{G}}) = (50, 40)$. The antenna footprint was designed so that the nulls of the footprint fits perfectly within the image patch of size 128-by-128. More specifically, the antenna footprint is given by $w(x,y) = \text{sinc}(\sqrt{x^2+y^2}/64)$. Figure 6.13(b) shows the contours of the range-direction terrain gradient $\frac{\partial h_G}{\partial x}(x,y)$, along with a black circle indicating a highly illuminated region defined by $w(x,y) \geq 0.1$. The highest elevation point of the terrain is outside the highly illuminated region, and the smallest value of $\frac{\partial h_G}{\partial x}(x,y)$ within the highly illuminated region is -0.094.[8] This means that a radar with flight parameters satisfying $H \geq 0.094R$ would be able to collect returns from all points in the highly illuminated region, without occlusion. In this section, we use a fixed, straight-line radar flight path with $R = 1000$ and $H = 100$. Correspondingly, we employ a set of Gaussian DEMs such that for the given flight path we are able to collect returns of all its points in the highly illuminated region. Note that in real applications, the DEM is given first and then the flight path is chosen according to the particular terrain so that the scene of interest can be seen from the radar with no obstructions.

We generate synthetic SAR data by using the image shown in Fig. 6.13(c)[9] as a model for the scene. Random spatial phases and the antenna pattern are applied to the scene and the demodulated data are synthesized using knowledge of the DEM. The demodulated data are then contaminated with phase errors generated from an i.i.d. uniform random distribution. Figures 6.13(d) and (e) are the FBPC reconstructions from the contaminated and uncontaminated SAR data, respectively. The image in Fig. 6.13(d) shows no prominent structure due to the severe defocusing caused by the i.i.d. random phase errors. Properly focused images are naturally depressed from attenuation by the antenna pattern, as shown in Fig. 6.13(e). In practice, the depressing effect in a highly illuminated region is inverted by amplitude normalization prior to display. Figure 6.13(f) shows the properly focused image multiplied by $\text{rect}[w(x,y)/0.2]\{w(x,y)\}^{-1}$, where rect is the rectangular function.

Figure 6.14 shows a set of autofocus results using extended MCA for different numbers of low-return constraints. The number of low returns $|\mathcal{S}|$ was chosen among $\{mN_\theta : m = 2, 3, \ldots, 7\}$,

[8] The colormap of the contour plot is modified so that only contours corresponding to levels in the range $\{\frac{\partial h_G}{\partial x}(x,y) : w(x,y) \geq 0.1\}$ are shown.

[9] This SAR image was provided by Sandia National Laboratories [25].

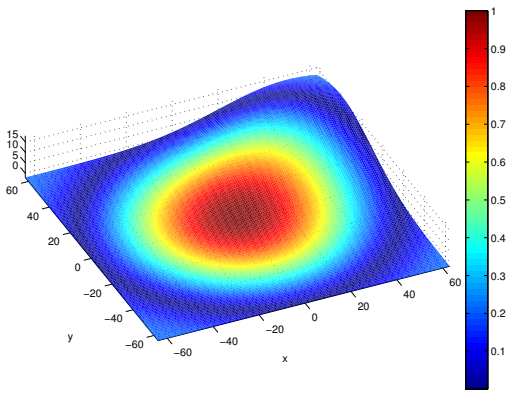

(a) Antenna pattern on Gaussian terrain

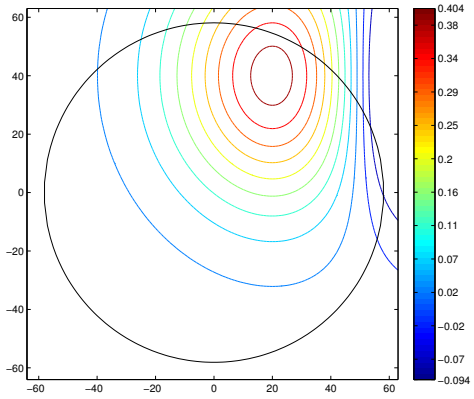

(b) $\frac{\partial h_G}{\partial x}$ and highly illuminated region

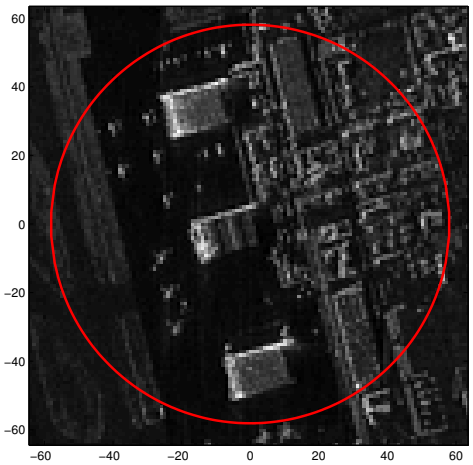

(c) Model scene

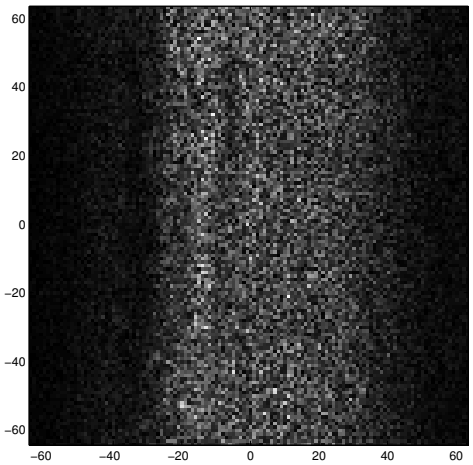

(d) Reconstruction from contaminated data

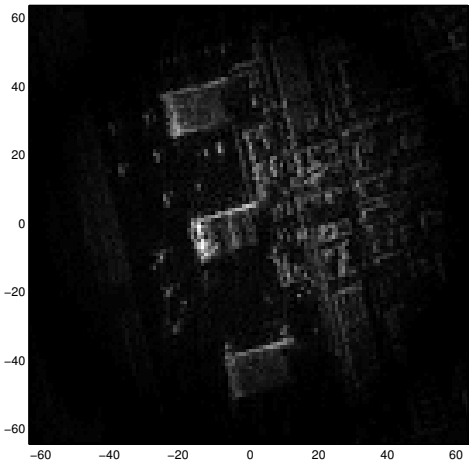

(e) Focused reconstruction (no phase error)

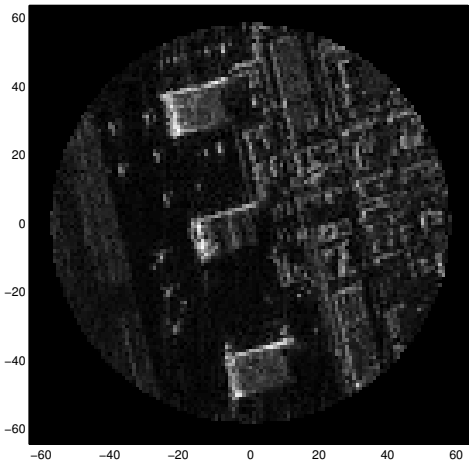

(f) Re-normalized (e)

Figure 6.13: Simulation setting for autofocus. (a) shows the antenna pattern, modeled by a circular sinc, on a terrain modeled by Gaussian DEM with parameters $A_{\mathrm{G}} = 20$, $\sigma_x = \sigma_y = 30$ and $(x_{0\mathrm{G}}, y_{0\mathrm{G}}) = (50, 40)$. (b) shows the contours of $\partial h_G / \partial x$, along with a black circle indicating a highly illuminated region. (c) is the SAR image that is used to model the reflectivity, along with a red circle indicating the highly illuminated region. (d) and (e) are FBPC reconstructions with and without phase errors, respectively, in the data. The phase errors are i.i.d., generated from a uniform random distribution. (f) is a re-normalized version of (e), where the amplitude attenuation by the antenna pattern is inverted.

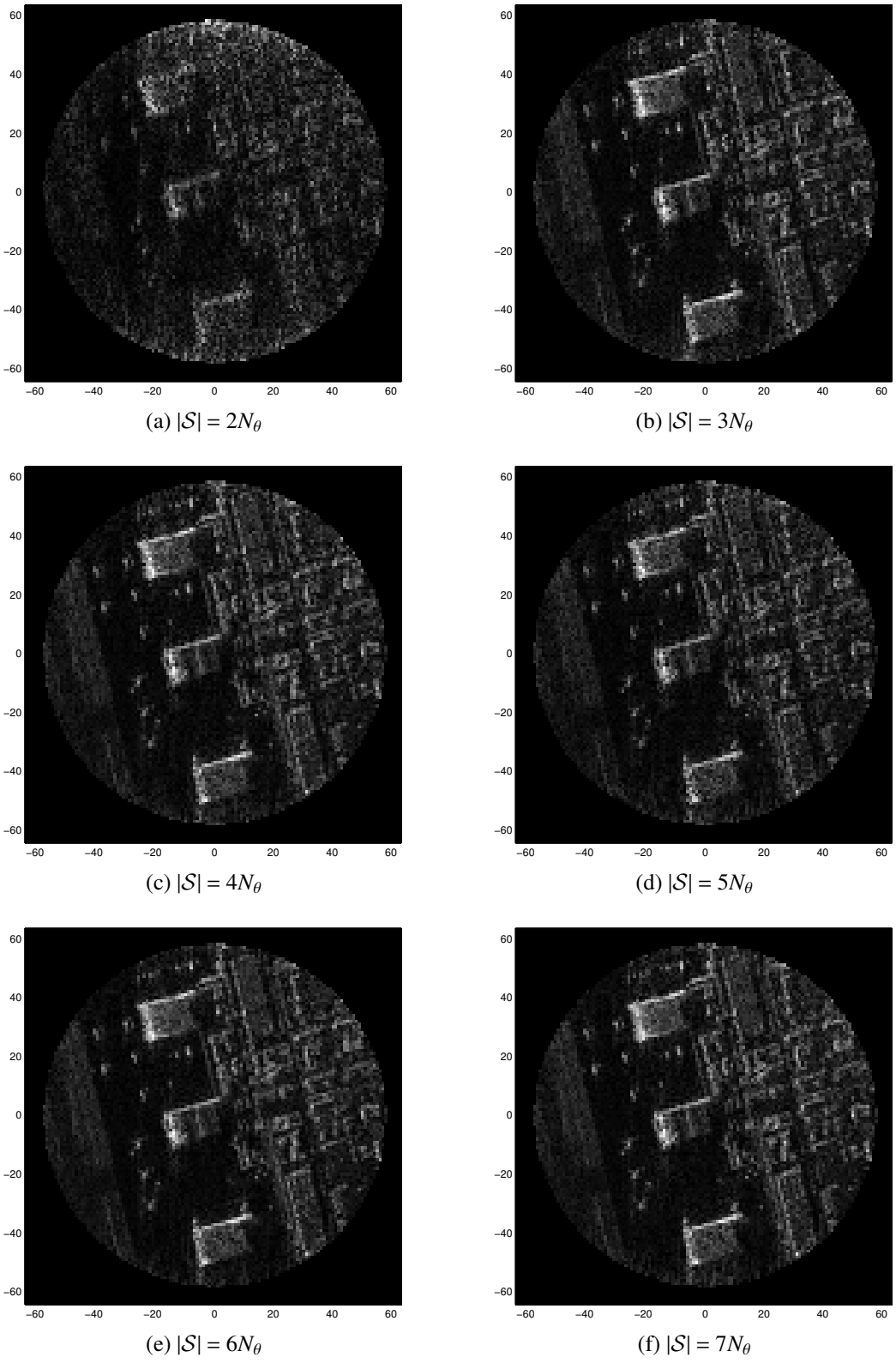

(a) $|\mathcal{S}| = 2N_\theta$ (b) $|\mathcal{S}| = 3N_\theta$

(c) $|\mathcal{S}| = 4N_\theta$ (d) $|\mathcal{S}| = 5N_\theta$

(e) $|\mathcal{S}| = 6N_\theta$ (f) $|\mathcal{S}| = 7N_\theta$

Figure 6.14: Restorations using extended MCA for different numbers of low-return constraints. The scene is assumed to be on terrain described by a Gaussian DEM with $A_{\mathrm{G}} = 20$, $\sigma_x = \sigma_y = 30$, and $(x_{0\mathrm{G}}, y_{0\mathrm{G}}) = (50, 40)$, and the antenna pattern is modeled by a circular sinc function. Entropies are (a) 8.0290, (b) 7.7650, (c) 7.7618, (d) 7.7737, (e) 7.7367, and (f) 7.7656, and the RMSEs are (a) 0.0894, (b) 0.0422, (c) 0.0480, (d) 0.0471, (e) 0.0350, and (f) 0.0366.

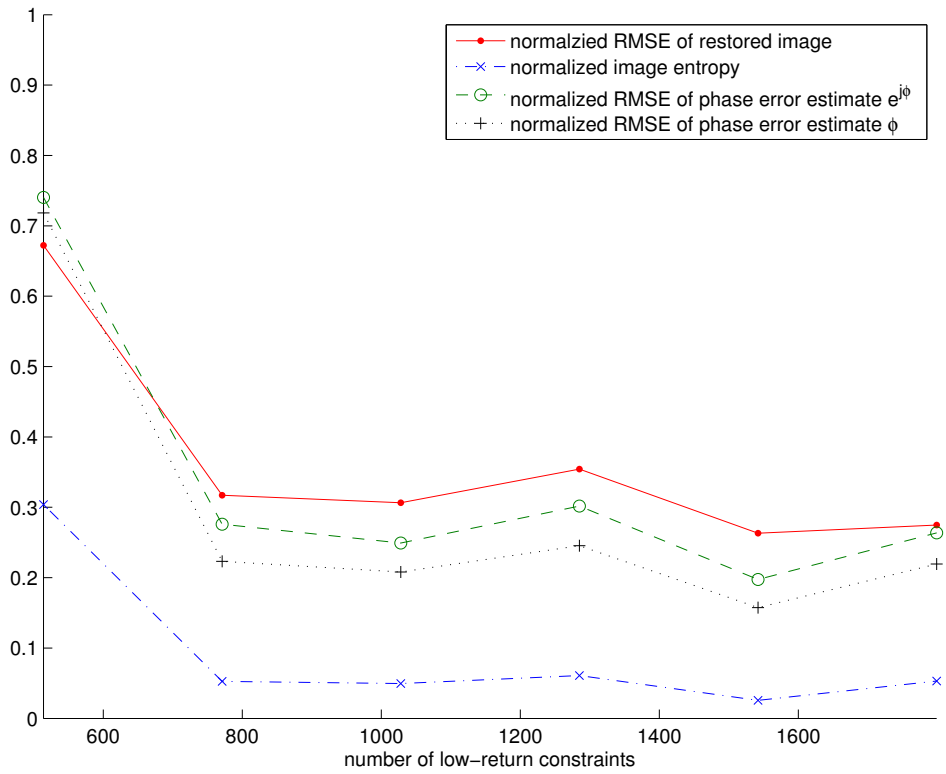

Figure 6.15: Normalized performance measures of extended MCA for different numbers of low-return constraints. The four performance measures (RMSE of restored image, image entropy, RMSE of the phase error estimates $\mathbf{e}^{j\hat{\boldsymbol{\phi}}}$, and RMSE of the phase error estimates $\hat{\boldsymbol{\phi}}$) are normalized so that 1 corresponds to the defocused image and 0 corresponds to the perfectly focused image.

where N_θ was 257. The low-return coordinates for each autofocus restoration were chosen from within the 128×128 image coordinates that correspond to the (mN_θ)-lowest values of the antenna footprint $w(x,y)$. As shown in images (a) to (f) in Fig. 6.14, the restoration quality differs for different numbers of constraints. For this example, extended MCA using more than $2N_\theta$ constraints produced a well-focused image, and both the image entropy and RMSE of the images indicate that Fig. 6.14(e) with $|\mathcal{S}| = 6N_\theta$ is the "best" restoration among them. It may appear that using a large enough number of constraints guarantees a good restoration, however, it should be noted that this is not always the case. The quality of the restored image may fluctuate (possibly significantly) as the number of constraints is increased. This makes it difficult to estimate the optimal number of low-return constraints to use. The general trend, however, is that the quality of the restored image improves little, if at all, beyond use of a certain number of low-return constraints. Thus, a simple approach that we adopt to determine a reasonable number of low-return constraint is to run MCA several times with varying number of low-return constraints and choose the restoration result with the lowest image entropy.

Figure 6.15 shows four different performance measures of extended MCA for different num-

bers of low-return constraints. The measurements are normalized so that 1 corresponds to the performance for the defocused image and 0 corresponds to the performance for the perfectly-focused image (reconstructed from error-free data). The red line shows the normalized RMSE of the restored image, with errors measured relative to the original scene reflectivity. The blue line shows the normalized image entropy of the restored images before re-normalization with the inverse of the antenna pattern.[10] The green and black lines show the normalized RMSEs of the phase error estimates, with the errors in $\hat{\boldsymbol{\phi}}$ measured by $\mathbf{e}^{j\hat{\boldsymbol{\phi}}} - \mathbf{e}^{j\boldsymbol{\phi}}$ and $\hat{\boldsymbol{\phi}} - \boldsymbol{\phi}$, respectively.[11] Note that the four performance measures follow the same trend. In real applications, only entropy can be measured without knowing the true values of reflectivity or phase errors. Hence, we use image entropy to identify the best restoration result of extended MCA, but we use RMSE of the restored images to evaluate the performance since these numbers are easier to interpret.

In Fig. 6.16, we elaborate on the application of extended MCA. The black pixels in Fig. 6.16(a) depict the $6N_\theta$ low-return coordinates that were used to produce the best restoration result in Fig. 6.14. The phase error estimates that were computed using the $6N_\theta$ low-return constraints are shown in Fig. 6.16(b). The true phase errors are marked with red dots and the estimates are marked with blue circles as functions of the associated look angle θ. The RMSE of the phase error estimates is 0.0445π.

Figure 6.17 shows how the usage of a DEM affects the autofocus results, with two sets of simulations for different Gaussian DEMs. The left column corresponds to parameters $A_{\text{G}} = 20$, $\sigma_x = \sigma_y = 30$, and $(x_{0\text{G}}, y_{0\text{G}}) = (50, 40)$ as in previous simulations, and the right column corresponds to the same set of parameters except $\sigma_x = \sigma_y = 20$. The first and second rows show images restored by extended MCA using and not using the DEM, respectively. The restoration quality is deteriorated without the use of the DEM. The last row shows images reconstructed using a two-step process: 1) correct the phase errors in the demodulated data using extended MCA without the DEM, and 2) reconstruct the image using FBP along curves onto the DEM. That is, the images in the second and last row are restored with the same phase corrections, with the difference being that Figs. 6.17(c) and (d) are formed on the ground plane and Figs. 6.17(e) and (f) are reformatted onto the known DEM. The image quality in Fig. 6.17(e) is noticeably increased from that in Fig. 6.17(c) and is comparable to that in Fig. 6.17(a). Yet, the image quality in Fig. 6.17(f) is not improved as much. Note that extended MCA was not a complete failure without the DEM and it restored focused images fairly well. This is because FBPC reconstructions onto the ground plane would not have had severe defocus or layover effect in the presumed low-return region for the particular

[10] For severely defocused images, only pixels near the edge of the highly illuminated region have large values after re-normalization. Such images have very low entropies, thus, entropy of the re-normalized images is not a valid performance measure.

[11] Possible constant phase shift in the phase error estimates and phase wrapping have been discounted when computing the RMSEs of the phase error estimates.

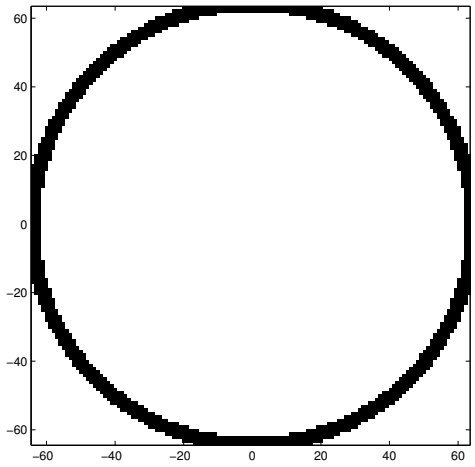

(a) Presumed low-return region

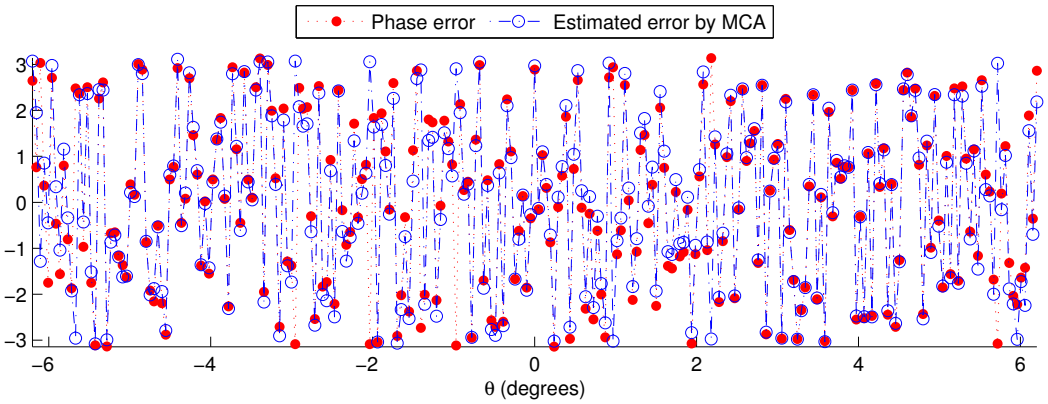

(b) Phase errors and the estimates

Figure 6.16: Application of extended MCA. (a) is the locus of the low-return coordinates for $|\mathcal{S}| = 6N_\theta$ that were used to produce the autofocused image in Fig. 6.14(e). (b) shows the phase errors that caused the defocusing (red dots) and the estimates by extended MCA (blue circles). RMSE of the restored image is 0.0350 and RMSE of the phase error estimates in (b) is 0.0445π.

DEMs used here.

Figure 6.18(a) summarizes the same sets of simulations for more variations of the DEM. NRMSEs of the "best" restorations are plotted as functions of $\sigma = \sigma_x = \sigma_y$ for five different values of A_{G}. Note that larger standard deviation σ corresponds to a larger portion of scene being at high elevation and larger values of A_{G} correspond to steeper terrain. The red dots and blue crosses correspond to the images restored by extended MCA using and not using the DEM, respectively. The green circles correspond to the images reconstructed onto the known DEM with phase corrections made without the DEM. Extended MCA using the DEM produced fairly focused images in all cases, with performance being best for the terrain with a gradual slope ($A_{\mathrm{G}} = 10$). Without the DEM, the performance of extended MCA degrades considerably as A_{G} grows.

The restoration quality improves as MCA restorations without the DEM are reformatted onto

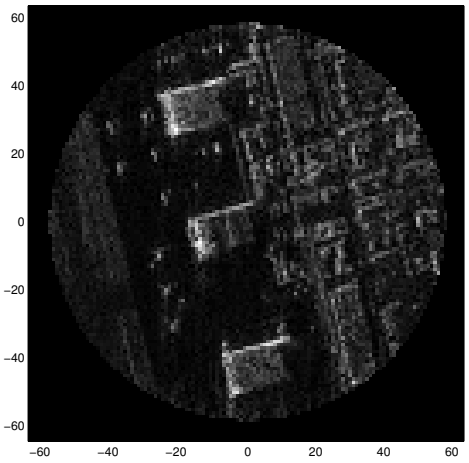

(a) using DEM, $\sigma = 30$, RMSE=0.0350

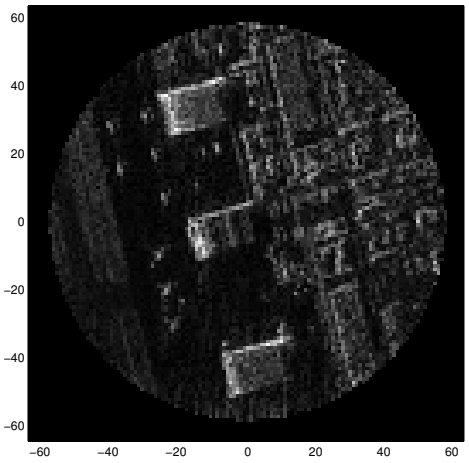

(b) using DEM, $\sigma = 20$, RMSE=0.0379

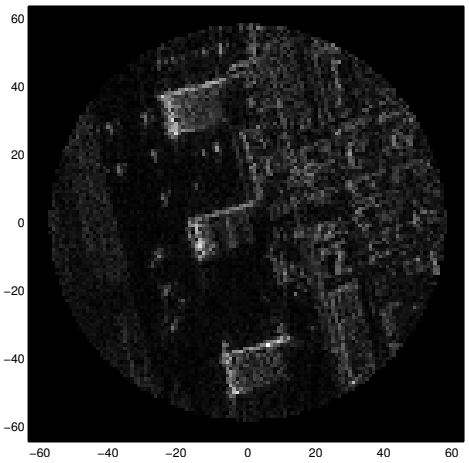

(c) without DEM, $\sigma = 30$, RMSE=0.0600

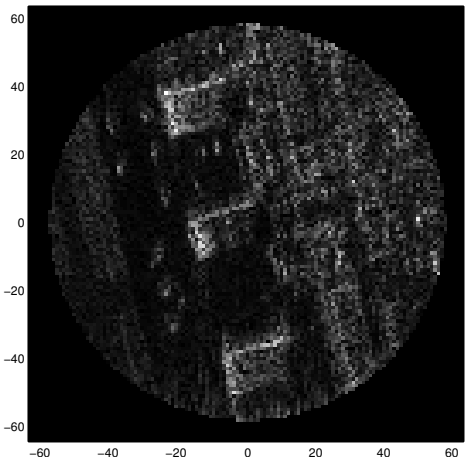

(d) without DEM, $\sigma = 20$, RMSE=0.0703

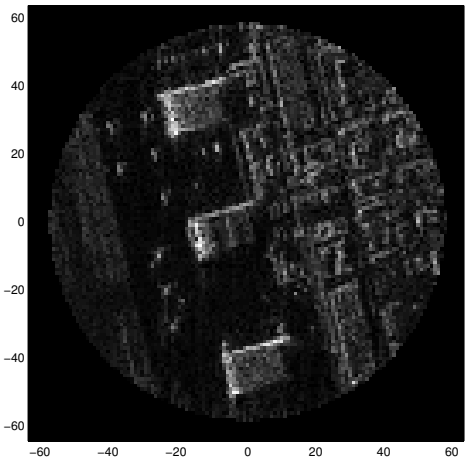

(e) Reformatted, $\sigma = 30$, RMSE=0.0356

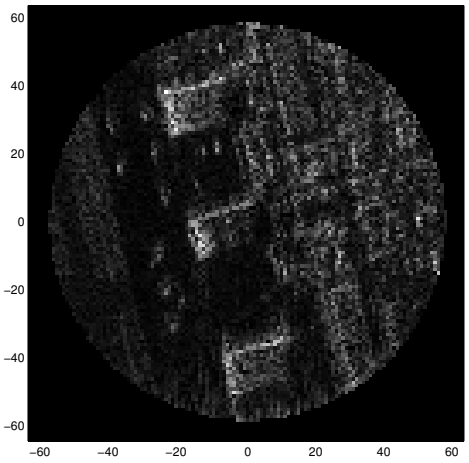

(f) Reformatted, $\sigma = 20$, RMSE=0.0656

Figure 6.17: Further extended MCA simulation results. The terrain is modeled by a Gaussain DEM with $A_{\mathrm{G}} = 20$, $\sigma_x = \sigma_y = \sigma$ and $(x_{0\mathrm{G}}, y_{0\mathrm{G}}) = (50, 40)$. The left and right columns correspond to simulations for $\sigma = 30$ and $\sigma = 20$, respectively. (a) and (b) are restored by extended MCA using the DEM and (c) and (d) are restored without using the DEM. (e) and (f) are reconstructed onto the DEM by FBP along curves after correcting the phase errors with estimations made by extended MCA without the DEM.

the known DEM. The quality enhancement is enough to make the resulting image comparable to that of the MCA restoration using the DEM for some cases, however, this is not a good approach in general. The phase error estimates obtained by using flawed low-return constraints for the ground plane images are inaccurate in challenging cases. When σ or A_{G} is large, simply reformatting a focused image onto the correct DEM is insufficient to produce a satisfactory result.

NRMSEs are also shown as a function of A_{G} for five different values of σ in Fig. 6.18(b). Similar observations can be made from this figure.

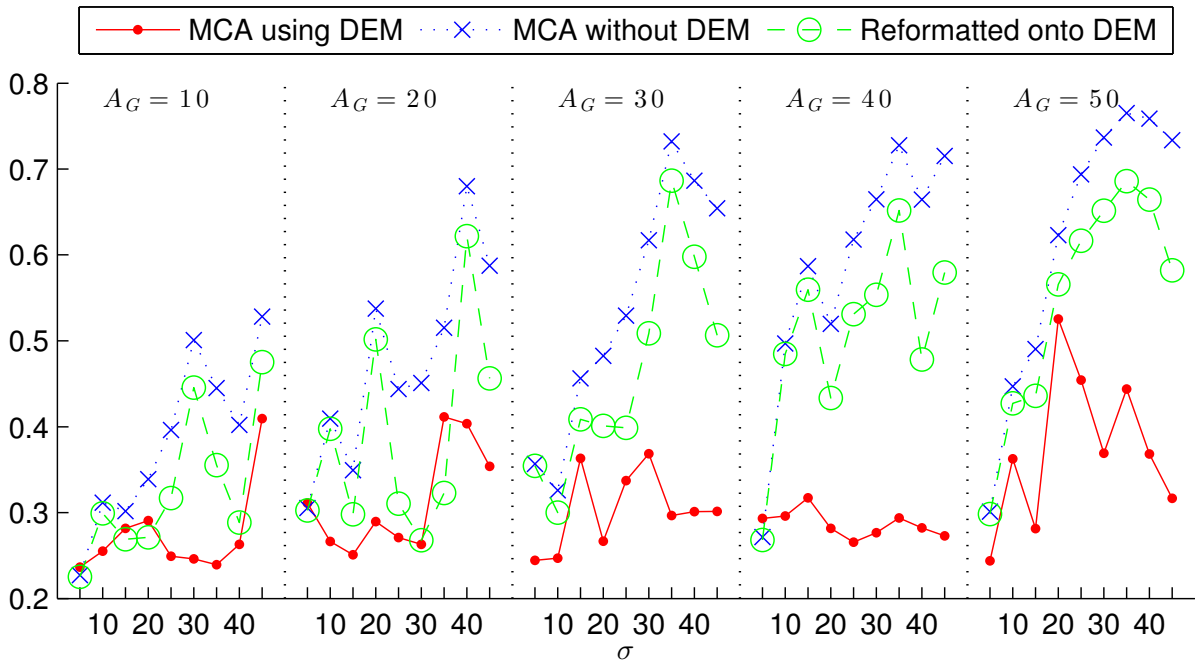

(a)

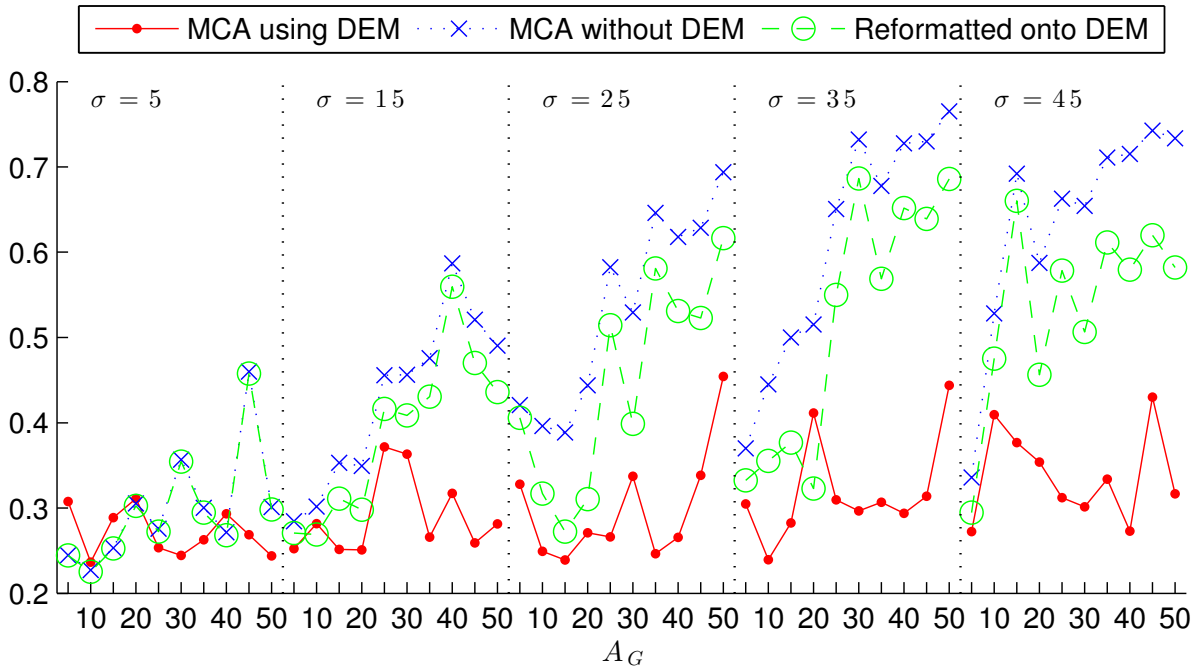

(b)

Figure 6.18: NRMSE of the "best" restorations of extended MCA. The terrain is modeled by a Gaussian DEM with $\sigma_x = \sigma_y = \sigma$ and $(x_{0G}, y_{0G}) = (50, 40)$. (a) NRMSE as a function of σ for nine different values of σ and five different values of A_G. (b) NRMSE as a function of A_G for ten different values of A_G and five different values of σ.

CHAPTER 7

Conclusion

7.1 Overcoming Polar-Format Issues in MCA

MCA does not provide the expected performance when used with SAR data collected on a polar grid, even for quite narrow data-collection angles. Our proposed method, RMCA, overcomes this problem by forming the solution space in the inverse-polar domain, where the defocusing effect is truly one dimensional. As with MCA, the performance of RMCA depends on the choice of the low-return constraints; thus, the low-return region must be carefully specified in the inverse-polar domain to achieve the best performance. To gain a better understanding of the inverse-polar domain, we provided an analytical formula for the impulse response. Simulation results demonstrated that, with an adequate selection of low-return constraints, RMCA achieves excellent performance for practical ranges of look angles, up to several degrees.

The performance of multichannel autofocus algorithms is degraded when the attenuation pattern has a relatively wide transition band. In fact, the transition is relatively smooth in the inverse-polar domain compared to that in the spatial domain, and even more, it is smoother for a wider range of look angles. Hence, the robustness to nonzero pixels in the presumed low-return region is very important for RMCA. Fortunately, the quality of RMCA restorations can be improved by incorporating sharpness metric optimization as a regularization term, as discussed in [21]. This challenge becomes more extreme if there are strong point reflectors in the weakly illuminated region of the radar beam. Since we cannot detect the strong reflectors prior to focusing the image, we have suggested using random subregions of the presumed low-return region in Ch. 4 and [32], or iteratively refining the image and the low-return constraints. Other possible issues that relate to nonideal low returns include multiplicative noise due to system nonlinearities, displacement of moving targets, and error in the inertial measurement unit of the radar.

The performance of RMCA is affected by variables that must be prescribed, such as the geometry of the presumed low-return region and the number of constraints. We analyzed how the geometry of the low-return region can affect the performance of RMCA in Ch. 4 for a simple case

where the antenna pattern is modeled by a rect function. However, the performance dependency on the geometry for a more realistic antenna pattern was not studied, which could be a topic of future research. Also, methods for optimal selection of the number of low-return constraints are not known and could be studied. The robustness and performance of the autofocus algorithm could be improved by seeking answers to these optimization questions.

7.2 Using Multiple Low-Return Constraints for MCA

We have presented a promising demonstration of the random subregion approach for selecting the low-return constraints of RMCA in the case of a few very strong anomalies in the presumed low-return region. With this simple approach, we can restore a well-focused image within a small number of trials, with high probability. Furthermore, even when the restoration is not perfect, one may use the information from the well-focused image to refine the low-return constraints and iterate. However, several key questions remain areas of active research. These include an analysis of the optimal size of the presumed low-return region and its subregion, how the performances differ as the location of anomalies or the range of look angles changes, and the possibility of a different type of subregion with a more robust performance. In wide-angle SAR, choosing the low-return constraints becomes more critical since the focused inverse-polar data do not exhibit a clear transition from high to low return in general; thus, when selecting the subregion, we must account for the fact that neighboring pixels of an anomaly in the inverse-polar domain may have significant magnitude.

7.3 Elimination of Filtering in FBP

Although omitting the filtering step in FBP degrades the point target response in CT, where there is no frequency offset, the difference in the shape and focus measures of the PTRs for SAR can be minor, especially as the frequency offset ratio, K, increases. In the 1-D analysis, the change in the mainlobe width and HPHW can be upper bounded by functions of K^{-2}, and the simulation results suggest that the positive effect of filtering is negligible for typical frequency offset ratios used in SAR systems.

As in the analysis of the 1-D analog, the effect of filtering on the 2-D PTRs produced by backprojection depended on the frequency offset ratio. The differences in the values of PTRs were smaller in the cross-range direction than in the range direction; the difference also diminished more sharply in the cross-range direction, whereas the difference in the range direction were the same as in the 1-D analysis.

The results for the near-field case are more complicated to assess, since the effect of filtering not only depends on the frequency offset ratio but also on how close the radar is to the center of the scene and the target. However, the dependency on wavefront curvature is weaker than on the frequency offset ratio, and simulation results showed that filtering increases average resolution less than 1% when $K \geq 4$, regardless of the wavefront curvature, and the effect of filtering is negligible for $K \geq 8$ ($\Theta \leq 16^o$).

In near-field imaging, filtering is not very beneficial when the frequency offset ratio is small because the filter for FBP is derived using a stationary phase approximation that assumes the employed radar frequencies are large. Hence, even the image reconstructed with filtering is not of good quality. On the other hand, filtering does not provide benefit when the frequency offset ratio is large and the filtering formula is accurate, because filtering is unimportant for large values of K. Overall, this is good news, because the filtering step can be complex in the near-field case. It is fortunate that in SAR systems using typical imaging parameters, the filtering step can be eliminated.

7.4 Imaging onto a Known DEM via FBPC and Autofocus

In Ch. 6, an explicit formulation of FBPC for spotlight-mode SAR imaging with a straight-line level flight path was given and analyzed. More specifically, we derived an approximation for the point target resolution using the method of stationary phase. This formula allowed us to analyze the dependency of image quality on the terrain, the amount of wavefront curvature, and the radar grazing angle. In summary, when the DEM is exactly known, FBP along curves produces orthographically correct images. However, when there are errors in the DEM, or if the DEM is simply unknown, images of prominent structures may suffer from layover effects. In other words, strong scatterers may appear in incorrect locations in the reconstructed image. The resolution is mostly affected by the terrain gradient in the range direction, or equivalently, by the grazing angle of the radar. Thus, imaging steep slopes, or, similarly, using a top-down view from the radar results in images with poor resolution.

MCA is a powerful framework for solving the SAR defocusing problem. We showed that it can be extended to situations with a known DEM, or for near-field imaging, by directly integrating the DEM into the linear-algebraic formulation for MCA. Importantly, extended MCA does not involve any additional post-processing steps to account for the DEM or for the effects of wavefront curvature. Similar to FBPC reconstruction, the performance of extended MCA is dependent on the terrain. It is important to use the DEM within MCA, especially when the slope of the terrain is steep, or when a large area of the scene is highly elevated within a presumed low-return region. The presumed low-return region may not correspond to low returns in the image formed on the ground

plane, resulting in inaccurate estimates of the phase errors. Simple reformatting of the image onto the known DEM, via a post-processing step, does not resolve the remaining defocusing problem due to the inaccurate corrections of the phase errors.

In Ch. 6, we considered a simple scenario where the radar travelled along a straight path. This allowed us to simplify the analysis of the point target responses that helped us to gain meaningful insight into the problem. However, the FBPC and extended MCA can be further extended to applications with arbitrary flight paths or for strip-map or squint-mode SAR. Although the analysis of point target responses would not hold for these extensions, most of the intuition from the straight-path analysis would carry over; we would still expect performance degradation for steep terrain or high grazing angles, and using the DEM within the formulation of MCA would still be important. Therefore, a natural future direction would be to apply MCA to the aforementioned scenarios.

FBPC employs spatially-variant filters that are computationally costly to apply. However, we have seen in Chapter 5 that such filters may offer little improvement to the quality of the reconstructed images. This point is especially relevant for radars operating at a long range with high frequency offset ratios. It remains to be seen if this lack of improvement is also valid for more complicated terrain and near-field scenarios. An in-depth study to confirm this hypothesis regarding the necessity of filtering may help improve the computational performance of FBPC.

We considered only the case where the radar is able to illuminate the entire terrain patch with each transmitted waveform. In general, portions of the terrain patch may be "shadowed" due to obstructions by non-penetrable objects or terrain within the radar transmission path. Although we cannot reconstruct an image in such a region, the shadowed region could be used as a low-return region for MCA. A shadowed region corresponds to zero return, and therefore may provide for ideal low-return constraints for MCA and enhance its performance.

For situations where the DEM is being derived from a pair of SAR images using interferometry, it may be the case that a defocusing problem exists in producing an accurate DEM. This raises the possibility of jointly estimating the errors in the DEM and the phase errors that defocus the image reconstructed using the DEM. This could be the subject of further study.

APPENDIX A

Formula of FBP along Curves onto a Known DEM

In this appendix, we show how the FBPC formula for a known DEM presented in Eq. (6.5) is obtained from [40]. The formula reduces to Eq. (5.4) for a special case where the radar and the terrain are at zero elevation.

A.1 Notation and Inversion Formula from [40]

$\psi(z)$ denotes the 3-D vector coordinate of the scene surface parameterized by a 2-D vector z, and $\gamma(s) \in \mathbb{R}^3$ denotes the radar location parameterized by a scalar variable s. $V(z)$ is the surface reflectivity at $\psi(z)$ that we wish to image. $R_{s,z} = \psi(z) - \gamma(s) \in \mathbb{R}^3$ is a vector to the point $\psi(z)$ on the scene terrain from the radar location $\gamma(s)$. t denotes the time of data collection, c_0 is the speed of light, and ω is the angular frequency argument. $A(z,s,t,\omega)$ is determined by various factors including the antenna beam pattern and the waveform of the radar.[1]

$d(s,t)$ is the data collected at time t from the radar at location $\gamma(s)$, and is related to the reflectivity V by

$$d(s,t) = \int A(z,s,t,\omega)\, V(z)\, \mathrm{e}^{-j\omega\left(t-\frac{2}{c_0}|R_{s,z}|\right)} d\omega dz. \tag{A.1}$$

Assuming that A is "well-bounded,"[2] we can reconstruct the image by

$$\hat{V}(z) = \frac{1}{(2\pi)^3} \int A^{-1}\left(z, s, \frac{2|R_{s,z}|}{c_0}, \omega\right) \left|\frac{\partial \xi}{\partial(s,\omega)}\right| (z,s,\omega)\, d(s,t)\, \mathrm{e}^{j\omega\left(t-\frac{2}{c_0}|R_{s,z}|\right)} d\omega ds dt, \tag{A.2}$$

[1] $A(z,s,t,\omega) = \omega^2 p(\omega) j_s(\omega, \widehat{R_{s,z}}, \gamma(s)) j_r(\omega, \widehat{R_{s,z}}, \gamma(s))/\{(4\pi)^2 |R_{s,z}|^2\}$, where p, j_s, j_r are the Fourier transforms of the waveform, current density of the transmission and reception antenna, respectively. $\widehat{v} = v/|v|$ is the unit vector of v. See Eq. (19) in [39] for more details.

[2] A is said to be "well-bounded" if $\sup_{(s,t,z)\in K} |\partial_\omega^\alpha \partial_s^\beta \partial_t^\delta \partial_{z_1}^{\rho_1} \partial_{z_2}^{\rho_1} A(z,s,t,\omega)| \le C_{K,\alpha,\beta,\delta,\rho_1,\rho_2} (1+\omega^2)^{(2-|\alpha|)/2}$ for any compact set K. See Eq. (6) in [40] for more details.

where the Jacobian determinant is

$$\left|\frac{\partial \xi}{\partial(s,\omega)}\right|(z,s,\omega) = \frac{4|\omega|}{c_0^2}\left|\begin{array}{cc} -\widehat{R_{s,z}}\cdot\frac{\partial\psi(z)}{\partial z_1} & P\perp\gamma'(s)\cdot\frac{\partial\psi(z)}{\partial z_1} \\ -\widehat{R_{s,z}}\cdot\frac{\partial\psi(z)}{\partial z_2} & P\perp\gamma'(s)\cdot\frac{\partial\psi(z)}{\partial z_2}\end{array}\right|. \tag{A.3}$$

Here, $P\perp\gamma'(s)$ is a scaled projection of $\gamma'(s)$ to the plane perpendicular to $R_{s,z}$, i.e.

$$P\perp\gamma'(s) = \frac{\gamma'(s) - (\widehat{R_{s,z}}\cdot\gamma'(s))\widehat{R_{s,z}}}{|R_{s,z}|}, \tag{A.4}$$

and $\widehat{v}$ is the notation for the unit vector corresponding to vector v. For simplicity, we have ignored the smooth taper function in the formulas.

A.2 Inversion Formula for a Straight and Level Flight Path

First, we make two changes of variables by

$$\begin{cases} t = \frac{2}{c_0}(u + d(0,0;s)) \\ \omega = -c_0\pi\rho \end{cases}, \tag{A.5}$$

so that Eq. (A.1) becomes

$$\tilde{d}(s,u) = \int V(z)\int \pi c_0 \tilde{A}(z,s,u,\rho)\,\mathrm{e}^{jc_0\pi\rho\frac{2}{c_0}\left(u+d(0,0;s)-|R_{s,z}|\right)}\,d\rho dz \tag{A.6}$$

$$= \pi c_0\int V(z)\,\mathcal{F}_\rho^{-1}\left\{\tilde{A}(z,s,u,\rho)\right\}\Big|_{u+d(0,0;s)-|R_{s,z}|}dz, \tag{A.7}$$

where $\mathcal{F}_\rho^{-1}$ denotes the Fourier transformation with respect to the variable ρ. We also write $\tilde{d}(s,u) = d(s,t)$ and $\tilde{A}(z,s,u,\rho) = A(z,s,t,\omega)$ for notational simplicity.

We let $s = -\tan\theta$ to represent the straight and level flight path in our scenario. For simplicity, let $d(x,y;s)$ and $r(x,y;s)$ denote $d_\theta(x,y)$ and $r_\theta(x,y)$, respectively. We consider our time-domain data to be the band-limited projections along curves. That is, the data collected from radar location $(-R,sR,H)$ is

$$\bar{p}(u;s) = \Delta\int g(x,y)\,\mathrm{sinc}\left[\Delta\{u - r(x,y;s)\}\right]\mathrm{e}^{j2\pi\rho_0\{u-r(x,y;s)\}}dxdy, \tag{A.8}$$

which is related to the demodulated data through $P_\theta(\rho) = \int \bar{p}(u;-\tan\theta)\,\mathrm{e}^{-i2\pi\rho u}du$. By comparing Eq. (A.8) with Eq. (A.7), and noting that $|R_{s,z}| - d(0,0;s) = r(x,y;s)$, we can find the function A

that makes our data model equivalent to Eq. (A.7):

$$\tilde{A}(z,s,u,\rho) = \frac{1}{\pi c_0}\mathcal{F}_x\left(\Delta\,\mathrm{sinc}\left[\Delta x\right]\mathrm{e}^{j2\pi\rho_0 x}\right) = \frac{1}{\pi c_0}\,\mathrm{rect}\left[\frac{1}{\Delta}(\rho-\rho_0)\right]. \tag{A.9}$$

With an appropriate taper function that limits the integration region to $\rho \in [\rho_0 - \Delta/2, \rho_0 + \Delta/2]$, the inversion formula (Eq. (A.2)) becomes

$$\hat{V}(z) = \frac{\pi c_0}{(2\pi)^2}\int\int\int_{\rho_0-\Delta/2}^{\rho_0+\Delta/2}\left|\frac{\partial\xi}{\partial(s,\omega)}\right|(z,s,-c_0\pi\rho)\,\tilde{d}(s,u)\,\mathrm{e}^{-j2\pi\rho\{u-r(x,y;s)\}}\,d\rho ds du. \tag{A.10}$$

Now, note that $\gamma'(s) = (0,R,0)$, $R_{s,z} = (x+R, y-sR, h(x,y)-H)$, and $|R_{s,z}| = d(x,y;s)$ for our scenario. Then, we have

$$P \perp \gamma'(s) = \frac{R}{\{d(x,y;s)\}^3}\,p(x,y,s), \tag{A.11}$$

where $p(x,y,s) = \Big(-(x+R)(y-sR),\, \{d(x,y;s)\}^2 - (y-sR)^2,\, -(y-sR)(h(x,y)-H)\Big)$ is a 3-D vector. The Jacobian determinant can be simplified by the following:

$$\left|\frac{\partial\xi}{\partial(s,\omega)}\right| = \frac{4R|\omega|}{c_0^2\{d(x,y;s)\}^4}\begin{vmatrix} -R_{s,z}\cdot\frac{\partial\psi(z)}{\partial z_1} & p(x,y,s)\cdot\frac{\partial\psi(z)}{\partial z_1} \\ -R_{s,z}\cdot\frac{\partial\psi(z)}{\partial z_2} & p(x,y,s)\cdot\frac{\partial\psi(z)}{\partial z_2}\end{vmatrix} \tag{A.12}$$

$$= \frac{4R|\omega|}{c_0^2\{d(x,y;s)\}^4}\left|\left(R_{s,z}\cdot\frac{\partial\psi(z)}{\partial z_1}\right)\left(p(x,y,s)\cdot\frac{\partial\psi(z)}{\partial z_1}\right) - \left(R_{s,z}\cdot\frac{\partial\psi(z)}{\partial z_1}\right)\left(p(x,y,s)\cdot\frac{\partial\psi(z)}{\partial z_1}\right)\right| \tag{A.13}$$

$$\begin{aligned} &= \frac{4R|\omega|}{c_0^2\{d(x,y;s)\}^4}\times \\ &\left|\left\{(x+R)+(h(x,y)-H)\frac{\partial h}{\partial x}\right\}\left\{(y-sR)^2-\{d(x,y;s)\}^2+(h(x,y)-H)\frac{\partial h}{\partial y}\right\}\right. \\ &\qquad\left.-(y-sR)\left\{(y-sR)+(h(x,y)-H)\frac{\partial h}{\partial y}\right\}\left\{(x+R)+(h(x,y)-H)\frac{\partial h}{\partial x}\right\}\right| \end{aligned} \tag{A.14}$$

$$\begin{aligned} &= \frac{4R|\omega|}{c_0^2\{d(x,y;s)\}^4}\left|(x+R)+(h(x,y)-H)\frac{\partial h}{\partial x}\right|\times \\ &\qquad\left|\{d(x,y;s)\}^2+(y-sR-1)(h(x,y)-H)\frac{\partial h}{\partial y}\right|, \end{aligned} \tag{A.15}$$

where $\frac{\partial h}{\partial x}$ and $\frac{\partial h}{\partial y}$ are shorthand notations for $\frac{\partial h}{\partial x}(x,y)$ and $\frac{\partial h}{\partial y}(x,y)$.

The inversion formula, Eq. (A.2), then becomes

$$\hat{V}(z) = \int\frac{R|(x+R)+(h(x,y)-H)\frac{\partial h}{\partial x}||\{d(x,y;s)\}^2+(y-sR-1)(h(x,y)-H)\frac{\partial h}{\partial y}|}{\{d(x,y;s)\}^4}$$

$$\int \int_{\rho_0-\Delta/2}^{\rho_0+\Delta/2} |\rho| \tilde{d}(s,u)\, \mathrm{e}^{-j2\pi\rho(u-r(x,y;s))}\, d\rho du ds. \tag{A.16}$$

By changing s to $-\tan\theta$, the formula reduces to a much familiar form of

$$\hat{g}(x,y) = \int F_\theta(x,y) \int_{\rho_0-\Delta/2}^{\rho_0+\Delta/2} |\rho| P_\theta(\rho)\, \mathrm{e}^{j2\pi r_\theta(x,y)\rho}\, d\rho d\theta, \tag{A.17}$$

where

$$F_\theta(x,y) = \frac{R|(x+R) + (h(x,y)-H)\frac{\partial h}{\partial x}|\,|\{d_\theta(x,y)\}^2 + (y+R\tan\theta-1)(h(x,y)-H)\frac{\partial h}{\partial y}|}{\cos^2\theta\{d_\theta(x,y)\}^4} \tag{A.18}$$

is the spatially-variant weight.

A.3 Special Case: Radar and Terrain at Zero Elevation

Here, we consider a 2-D collection geometry where the radar flight path is at zero elevation, and the scene surface is on the ground plane. That is, $H = 0$ and $h(x,y) = 0$. Then, the spatially-variant weight Eq. (A.18) reduces to

$$F_\theta(x,y) = \frac{R|(x+R)|}{\cos^2\theta\{d_\theta(x,y)\}^2} = \frac{R|x+R|\sec^2\theta}{(x+R)^2+(y+R\tan\theta)^2}. \tag{A.19}$$

Note that this result can also be obtained from [39].

APPENDIX B

Upper Bound and Approximation of Mainlobe Width without Filtering in 1-D

Here, we derive the upper bound, Eq. (5.17), and the approximation, Eq. (5.18), of the half mainlobe width $z_{0,m}(K)$. The bound and approximation show how the mainlobe width of $\bar{h}_0(;K)$ depends on the frequency offset ratio K when filtering is omitted.

Let $f(z;K) \triangleq \{\pi^2(K^2-1)z^2+2\}\sin(\pi z) - 2\pi z\cos(\pi z)$. Then, $z_{0,m}(K)$ is the smallest positive z that satisfies $f(z;K)=0$. The derivative of f is

$$f'(z;K) = 2\pi^2K^2z\sin(\pi z) + \pi^3(K^2-1)z^2\cos(\pi z). \tag{B.1}$$

Since $f'(z;K)>0$ for $0<z\le\frac{1}{2}$ and $f(0;K)=0$, $f(z;K)$ is positive for $0<z\le\frac{1}{2}$. Also, it is clear from the formula of $f(z;K)$ that it is positive for $\frac{1}{2}<z\le 1$. Thus, $z_{0,m}(K)$ is larger than 1. Furthermore, since $f(1.5;K) = -\frac{9}{4}\pi^2(K^2-1)-2$ is negative, $z_{0,m}(K)$ is between 1 and 1.5.

The second-order derivative of f is

$$f''(z;K) = \pi^2\Big[K^2\{(2-\pi^2z^2)\sin(\pi z)+4\pi z\cos(\pi z)\} + \{\pi^2z^2\sin(\pi z) - 2\pi z\cos(\pi z)\}\Big]. \tag{B.2}$$

For all $K>1$, $f''(z;K)$ is negative for $1\le z\le z_n$, where $z_n\approx 1.27$ is the value of z that satisfies $(2-\pi^2z^2)\sin(\pi z)+4\pi z\cos(\pi z)=0$. By using the fact that f' is a decreasing negative function in the range of $(1,z_n)$, it can be shown that f is upper-bounded by its tangent at $z=1$ in the range of interest. The tangent is given by $-\pi^3(K^2-1)(z-1)+2\pi$ and the cross point of the tangent and the z-axis is an upper bound to $z_{0,m}(K)$. This upper bound is $1+\frac{2/\pi^2}{K^2-1}$.

The approximation of $z_{0,m}(K)$ is derived from the second-order Taylor series of f about $z=1$. Since $\sin(\pi z)\approx\pi(z-1)$ and $\cos(\pi z)\approx 1-\frac{\pi^2}{2}(z-1)^2$, we have

$$\begin{aligned} f(z;K) &= [\pi^2(K^2-1)(z-1)^2 + 2\pi^2(K^2-1)(z-1) + \{\pi^2(K^2-1)+2\}]\sin(\pi z) - 2\pi\{(z-1)+1\}\cos(\pi z) \\ &\approx 2\pi^3(K^2-1)(z-1)^2 + \{\pi^3(K^2-1)+2\pi\}(z-1) - 2\pi(z-1) - 2\pi + \pi^3(z-1)^2 \end{aligned}$$

$$= \pi^3\{2(K^2-1)+1\}(z-1)^2 + \pi^3(K^2-1)(z-1) - 2\pi \tag{B.3}$$

By solving the quadratic equation for $(z-1)$, we have

$$z_{0,m}(K) \approx 1 + \frac{\sqrt{(K^2-1)^2 + \frac{16}{\pi^2}(K^2-1) + \frac{8}{\pi^2}} - (K^2-1)}{4(K^2-1)+2} \tag{B.4}$$

$$= 1 + \frac{\sqrt{K^4 - 2aK^2 + a} - (K^2-1)}{4(K^2-1)+2}, \tag{B.5}$$

where $a = 1 - \frac{8}{\pi^2} \approx 0.19$. Using $\sqrt{1+x} \approx 1 + \frac{x}{2}$ for $x \ll 1$, the above further can be approximated as

$$z_{0,m}(K) \approx 1 + \frac{(K^2-a)\{1 + \frac{a(1-a)}{2(K^2-a)^2}\} - (K^2-1)}{4(K^2-1)+2} = 1 + \frac{1-a}{4} \times \frac{2K^2-a}{(2K^2-1)(K^2-a)}. \tag{B.6}$$

APPENDIX C

Bounds for HPHW without Filtering in 1-D

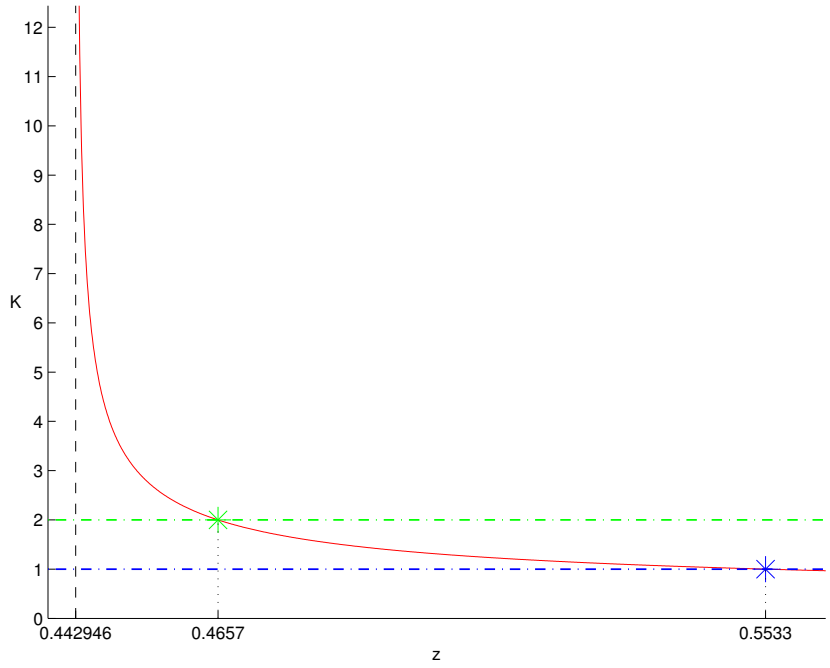

Figure C.1: Computing HPHW of $\bar{h}_0(;K)$ from Eq. (C.1). The red line shows the function on the right-hand side of Eq. (C.1), and the blue and green stars show the HPHW value for $K = 1$ and $K = 2$, respectively. The HPHW of $\bar{h}_r$ is also indicated by the black dashed line at $z = z_{r,h}$.

Here, we derive Eq. (5.20), which shows how $z_{0,h}(K)$, the HPHW of $\bar{h}_0(;K)$, depends on the frequency offset ratio K.

As stated in Sec. 5.4.2.2, the HPHW of $\bar{h}_0(;K)$ satisfies Eq. (5.19), which we can rewrite as

$$K = \frac{\mathrm{sinc}(z) - \cos(\pi z)}{\sqrt{\pi^2 z^2/2 - \sin^2(\pi z)}}. \tag{C.1}$$

Figure C.1 shows how $z_{0,h}(K)$ can be computed for different values of K. It can easily be seen

that the only values of z affecting the calculation of $z_{0,h}(K)$ are in the range of $[z_{r,h}, z_{\max}]$, where $z_{r,h} \approx 0.442946$ is the HPHW of $\bar{h}_r$ and $z_{\max} = z_{0,h}(1) \approx 0.5533$.

Then first, note that $\mathrm{sinc}(z) - \cos(\pi z)$ is an increasing function of z within the range of interest. Secondly, note that

$$1 - \pi^2 (z - \frac{1}{2})^2 \leq \sin^2(\pi z), \tag{C.2}$$

which follows from the second-order Taylor series expansion of $\sin^2(\pi z)$ about $z = \frac{1}{2}$. Lastly, we have

$$\begin{aligned} \sin^2(\pi z) = 1 - \cos^2(\pi z) = 1 - \sin^2\left\{\pi\left(z - \frac{1}{2}\right)\right\} &= 1 - \left\{\mathrm{sinc}(z - \frac{1}{2})\right\}^2 \left\{\pi(z - \frac{1}{2})\right\}^2 \\ &\leq 1 - \pi^2 \left\{\mathrm{sinc}(z_{r,h} - \frac{1}{2})\right\}^2 \left(z - \frac{1}{2}\right)^2, \end{aligned} \tag{C.3}$$

where the inequality holds for $z \in [z_{r,h}, z_{\max}]$.

By combining the above inequalities, we get

$$\frac{\{\mathrm{sinc}(z_{r,h}) - \cos(\pi z_{r,h})\}^2}{\pi^2 z^2/2 - 1 + \pi^2 (z - \frac{1}{2})^2} \leq K^2 \leq \frac{\{\mathrm{sinc}(z_{\max}) - \cos(\pi z_{\max})\}^2}{\pi^2 z^2/2 - 1 + \pi^2 \,\mathrm{sinc}^2(z_{r,h} - \frac{1}{2})(z - \frac{1}{2})^2}.$$

Solving each inequality for z yields

$$\frac{\{\mathrm{sinc}(z_{\max}) - \cos(\pi z_{\max})\}^2}{K^2} \geq \frac{\pi^2}{2} z^2 - 1 + \pi^2 \left\{\mathrm{sinc}(z_{r,h} - \frac{1}{2})\right\}^2 (z - \frac{1}{2})^2$$

and

$$\frac{\pi^2}{2} z^2 - 1 + \pi^2 (z - \frac{1}{2})^2 \geq \frac{\{\mathrm{sinc}(z_{r,h}) - \cos(\pi z_{r,h})\}^2}{K^2},$$

and finally

$$\frac{1}{3} + \sqrt{\frac{2}{3\pi^2} - \frac{1}{18}} \sqrt{1 + \frac{c_4}{K^2}} \leq z_{0,h}(K) \leq c_1 + c_2 \sqrt{1 + \frac{c_3}{K^2}},$$

where the constants are given in the following.

- $c_1 = \mathrm{sinc}^2(z_{r,h} - \frac{1}{2}) / \{2\,\mathrm{sinc}^2(z_{r,h} - \frac{1}{2}) + 1\} \approx 0.3321$
- $c_2 = \sqrt{2 - \frac{\pi^2 - 8}{2} \mathrm{sinc}^2(z_{r,h} - \frac{1}{2})} / \pi / \{2\,\mathrm{sinc}^2(z_{r,h} - \frac{1}{2}) + 1\} \approx 0.1108$
- $c_3 = \{2\,\mathrm{sinc}^2(z_{r,h} - \frac{1}{2}) + 1\} \{\mathrm{sinc}(z_{\max}) - \cos(\pi z_{\max})\}^2 / \{1 - \frac{\pi^2 - 8}{4} \mathrm{sinc}^2(z_{r,h} - \frac{1}{2})\} \approx 2.9845$
- $c_4 = \frac{12}{12 - \pi^2} \{\mathrm{sinc}(z_{r,h}) - \cos(\pi z_{r,h})\}^2 \approx 1.5752$

APPENDIX D

Computation of Integrated Sidelobe Ratios in 1-D

Here, we compute the ISLR of $\bar{h}_r$ and the derive the approximation to the ISLR of $\bar{h}_0(;K)$ stated in Eq. (5.21). The ISLR of the impulse response with filtering (1-D analogy) is computed as the following.

$$\begin{aligned}
(\text{ISLR})\{\bar{h}_r\} &= \frac{\int_{-\infty}^{\infty}|\bar{h}_r(z)|^2dz}{\int_{-1}^{1}|\bar{h}_r(z)|^2dz} - 1 = \frac{\int_{-\infty}^{\infty}|\operatorname{rect}(f)|^2df}{\int_{-1}^{1}|\operatorname{sinc}(z)|^2dz} - 1 = \left(\int_{-1}^{1}|\operatorname{sinc}(z)|^2dz\right)^{-1} - 1 \\
&= \left(2\int_0^1 \frac{\{\sin(\pi z)\}^2}{(\pi z)^2}dz\right)^{-1} - 1 = \left(2\int_0^1 \frac{1-\cos(2\pi z)}{2(\pi z)^2}dz\right)^{-1} - 1 \\
&= \left(2\left[\frac{\cos(2\pi z)-1}{2\pi^2 z}\right]_0^1 + 2\int_0^1 \frac{\sin(2\pi z)}{\pi z}dz\right)^{-1} - 1 \\
&= \left(2\int_0^1 \frac{\sin(2\pi z)}{\pi z}dz\right)^{-1} - 1 = \left(2\int_0^{2\pi}\frac{\sin(t)}{t/2}\frac{1}{2\pi}dt\right)^{-1} - 1 = \left(\frac{2}{\pi}\operatorname{Si}(2\pi)\right)^{-1} - 1 \\
&= \frac{\pi}{2\operatorname{Si}(2\pi)} - 1 \approx 0.107634,
\end{aligned}$$

where the second equality follows from Parseval's Theorem and Si is the sine integral function defined as $\operatorname{Si}(x) = \int_0^x \frac{\sin(t)}{t}dt$. In dB measure, the ISLR is $-9.68(dB)$.

When we leave out the filtering, we have

$$(\text{ISLR})\{\bar{h}_0(;K)\} = \frac{\int_{-\infty}^{\infty}|\bar{h}_0(z;K)|^2dz}{\int_{-z_1}^{z_1}|\bar{h}_0(z;K)|^2dz} - 1 = \frac{\int_{-\infty}^{\infty}|\operatorname{sinc}(z) + j\frac{1}{\pi K}\operatorname{dsinc}(z)|^2dz}{\int_{-z_1}^{z_1}|\operatorname{sinc}(z) + j\frac{1}{\pi K}\operatorname{dsinc}(z)|^2dz} - 1, \tag{D.1}$$

where z_1 is shorthand notation for $z_{0,m}(K)$, which is half of the mainlobe of $\bar{h}_0(;K)$. The numerator can be evaluated by applying Parseval's Theorem as in the following.

$$\int_{-\infty}^{\infty}|\bar{h}_0(z;K)|^2dz = \frac{f_0^2}{\Delta^2}\int_{-\infty}^{\infty}\left|\bar{h}_0\left(\frac{z}{\Delta};K\right)\right|^2dz = \frac{f_0^2}{\Delta}\int_{-\infty}^{\infty}|\bar{h}_0(x;K)|^2dx$$

$$
\begin{aligned}
&= \frac{f_0^2}{\Delta}\int_{f_0-\Delta/2}^{f_0+\Delta/2}\left(-\frac{1}{f_0^2}f+\frac{2}{f_0}\right)^2 df \\
&= \frac{f_0^2}{\Delta}\int_{f_0-\Delta/2}^{f_0+\Delta/2}\left(\frac{2f_0-f}{f_0^2}\right)^2 df \\
&= \frac{1}{f_0^2\Delta}\int_{-\Delta/2}^{\Delta/2}(f_0-f')^2\,df' \\
&= \frac{1}{3f_0^2\Delta}\left[(f'-f_0)^3\right]_{-\Delta/2}^{\Delta/2} = \frac{1}{3f_0^2\Delta}\left\{\left(\frac{\Delta}{2}-f_0\right)^3+\left(\frac{\Delta}{2}+f_0\right)^3\right\} \\
&= \frac{2}{3f_0^2\Delta}\left(\frac{\Delta^3}{8}+3\frac{\Delta}{2}f_0^2\right) = 1+\frac{1}{3L^2}.
\end{aligned}
$$

The denominator of Eq. (D.1) is given by

$$
\begin{aligned}
&\int_{-z_1}^{z_1}\{\mathrm{sinc}(z)\}^2+\frac{1}{\pi^2K^2}\{\mathrm{dsinc}(z)\}^2dz \\
&\quad= \int_{-z_1}^{z_1}\{\mathrm{sinc}(z)\}^2+\frac{\{\cos(\pi z)\}^2-2\,\mathrm{sinc}(z)\cos(\pi z)+\{\mathrm{sinc}(z)\}^2}{\pi^2K^2z^2}dz \\
&\quad= \left[\frac{2\pi z\,\mathrm{Si}(2\pi z)+\cos(2\pi z)-1}{2\pi^2z}\right]_{-z_1}^{z_1}-\left[\frac{\pi z\,\mathrm{Si}(2\pi z)+\{\cos(\pi z)\}^2}{\pi^2K^2z}\right]_{-z_1}^{z_1} \\
&\qquad+\left[\frac{4\pi^2z^2\,\mathrm{Si}(2\pi z)+\sin(2\pi z)+2\pi z\cos(2\pi z)}{2\pi^3K^2z^2}\right]_{-z_1}^{z_1} \\
&\qquad-\left[\frac{4\pi^3z^3\,\mathrm{Si}(2\pi z)+(2\pi^2z^2-1)\cos(2\pi z)+\pi z\sin(2\pi z)+1}{6\pi^4K^2z^3}\right]_{-z_1}^{z_1} \\
&\quad= \left[\frac{1}{\pi}\mathrm{Si}(2\pi z)+\frac{\cos(2\pi z)}{2\pi^2z}-\frac{1}{2\pi^2z}\right]_{-z_1}^{z_1} \\
&\quad+\frac{1}{\pi^2K^2}\left[\frac{\pi}{3}\mathrm{Si}(2\pi z)+\frac{\cos(2\pi z)}{6z}+\frac{\sin(2\pi z)}{3\pi z^2}-\frac{1}{2z}+\frac{\cos(2\pi z)-1}{6\pi^2z^3}\right]_{-z_1}^{z_1} \\
&\quad= \left[\frac{1}{\pi}\left(1+\frac{1}{3K^2}\right)\mathrm{Si}(2\pi z)+\frac{1}{2\pi^2z}\left(1+\frac{1}{3K^2}\right)\cos(2\pi z)\right]_{-z_1}^{z_1} \\
&\qquad+\left[\frac{-3K^2-1-1+\cos(2\pi z)-2\{\cos(\pi z)-\mathrm{sinc}(z)\}^2}{6\pi^2K^2z}\right]_{-z_1}^{z_1} \\
&\quad= \frac{2}{\pi}\left(1+\frac{1}{3K^2}\right)\mathrm{Si}(2\pi z_1)+\frac{1}{\pi^2z_1}\left(1+\frac{1}{3K^2}\right)\cos(2\pi z_1) \\
&\qquad-\frac{1}{\pi^2z_1}\left(1+\frac{1}{3K^2}\right)-\frac{2\sin^2(\pi z_1)+2\{\cos(\pi z_1)-\mathrm{sinc}(z_1)\}^2}{3\pi^2K^2z_1} \\
&\quad= \frac{2}{\pi}\left(1+\frac{1}{3K^2}\right)\mathrm{Si}(2\pi z_1)-2\left(1+\frac{1}{3K^2}\right)\frac{\sin^2(\pi z_1)}{\pi^2z_1}-\frac{(K^2-1)^2\pi^2z_1^2+4}{6K^2}\frac{\sin^2(\pi z_1)}{\pi^2z_1}.
\end{aligned}
\tag{D.2}
$$

The last equality follows since z_1 satisfies

$$\cos(\pi z_1) - \mathrm{sinc}(z_1) = \frac{(K^2-1)\pi}{2} z_1 \sin(\pi z_1).$$

Since the third summand of Eq. (D.2) has a value much smaller than the first and second summands, we can ignore the third term and approximate the ISLR of $\bar{h}_0(;K)$ with

$$(\mathrm{ISLR})\{\bar{h}_0(;K)\} \approx \frac{\pi}{2} \frac{1}{\mathrm{Si}(2\pi z_1) - \sin^2(\pi z_1)/(\pi z_1)} - 1. \tag{D.3}$$

APPENDIX E

Understanding the Spatially-Varying Resolution for Near-Field

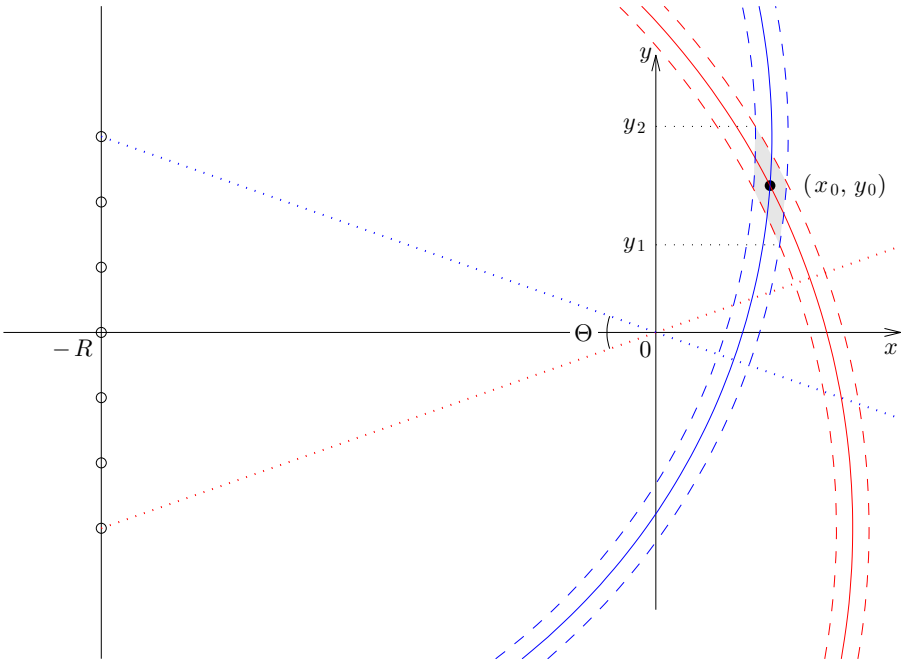

Figure E.1: Circular projections for near field.

Here, we explain why the resolution varies for different point target locations in Fig. 5.13.

To simplify the analysis, consider backprojecting a rect function with width 2δ, centered at a location corresponding to a point target at (x_0, y_0). Suppose the radar's flight path is at distance R from the center of the image patch, and the data collection angle is Θ. Figure E.1 shows the geometry.

The backprojection corresponding to a single view angle θ is

$$b_\theta(x, y; x_0, y_0) = \text{rect}\left(\frac{r_\theta(x, y) - r_\theta(x_0, y_0)}{\delta}\right), \tag{E.1}$$

where $r_\theta(x,y) = \sqrt{(x+R)^2 + (y+R\tan\theta)^2}$. The sum of backprojections for different view angles $|\theta| \le \Theta/2$ form the final image, where there is a region surrounding the point target where the reconstruction has a nearly constant value. This region is defined by

$$\{(x,y) : |r_{-\Theta/2}(x,y) - r_{-\Theta/2}(x_0,y_0)| \le \delta\} \cup \{(x,y) : |r_{\Theta/2}(x,y) - r_{\Theta/2}(x_0,y_0)| \le \delta\},$$

where the two sets, corresponding to backprojections from the extreme angles $-\Theta/2$ and $\Theta/2$, form a region with four vertices. Among the four points, we are interested in two extreme points in the cross-range direction, satisfying:

$$(x_1,y_1) = \{r_{-\Theta/2}(x,y) - r_{-\Theta/2}(x_0,y_0) = \delta\} \cup \{r_{\Theta/2}(x,y) - r_{\Theta/2}(x_0,y_0) = -\delta\}$$

and

$$(x_2,y_2) = \{r_{-\Theta/2}(x,y) - r_{-\Theta/2}(x_0,y_0) = -\delta\} \cup \{r_{\Theta/2}(x,y) - r_{\Theta/2}(x_0,y_0) = \delta\}.$$

The intersection has a cross-range span of

$$\begin{aligned}
|y_2 - y_1| &= \frac{(r_{-\Theta/2}(x_0,y_0)+\delta)^2 - (r_{\Theta/2}(x_0,y_0)-\delta)^2}{4R\tan\left(\frac{\Theta}{2}\right)} - \frac{(r_{-\Theta/2}(x_0,y_0)-\delta)^2 - (r_{\Theta/2}(x_0,y_0)+\delta)^2}{4R\tan\left(\frac{\Theta}{2}\right)} \\
&= \frac{\delta\left(r_{-\Theta/2}(x_0,y_0) + r_{\Theta/2}(x_0,y_0)\right)}{R\tan\left(\frac{\Theta}{2}\right)} \\
&= \frac{\delta}{\tan(\Theta/2)}\left\{\sqrt{(1+\frac{x_0}{R})^2 + (\tan\frac{\Theta}{2} + \frac{y_0}{R})^2} + \sqrt{(1+\frac{x_0}{R})^2 + (\tan\frac{\Theta}{2} - \frac{y_0}{R})^2}\right\}.
\end{aligned}$$

For point targets along the range-axis, i.e. when $y_0 = 0$,

$$|y_2 - y_1| = \frac{2\delta}{\tan\left(\frac{\Theta}{2}\right)}\sqrt{(1+\frac{x_0}{R})^2 + \tan^2\frac{\Theta}{2}} \approx \frac{2\delta}{\tan\left(\frac{\Theta}{2}\right)}\left(1+\frac{x_0}{R}\right),$$

which becomes smaller as $x_0 \to -R$. This result helps explain why resolution is higher for locations in the image that are closer to the radar flight path for near-field imaging.

APPENDIX F

Explicit Formula for the Spatially-Variant Normalization Constant

F.1 Derivation of the Normalization Constant

Here, we present the derivation of the normalization constant $\int f_2(x,y;\theta)\,d\theta$ for FBPC using the Nolan-Cheney filter. Recall that f_2 is

$$f_2(x,y;\theta) = \frac{R^2\sec^2\theta|\{d_\theta(x,y)\}^2 + (y+R\tan\theta-1)(h(x,y)-H)\frac{\partial h}{\partial y}(x,y)|}{\{d_\theta(x,y)\}^4}.$$

The following is satisfied for points with a smooth gradient $\frac{\partial h}{\partial y}(x,y)$, for most typical ranges of look angles Θ and grazing angles from the radar:

$$\{d_\theta(x,y)\}^2 + (y+R\tan\theta-1)(h(x,y)-H)\frac{\partial h}{\partial y}(x,y) > 0, \quad \forall|\theta| \le \frac{\Theta}{2}. \tag{F.1}$$

In such cases, we have

$$\begin{aligned}
\int_{-\Theta/2}^{\Theta/2} f_2(x,y;\theta)d\theta &= R^2\int_{-\Theta/2}^{\Theta/2}\frac{\{d_\theta(x,y)\}^2 + (y+R\tan\theta-1)(h(x,y)-H)\frac{\partial h}{\partial y}(x,y)}{\cos^2\theta\{d_\theta(x,y)\}^4}d\theta &\text{(F.2)}\\
&= R^2\int_{-\Theta/2}^{\Theta/2}\frac{\sec^2\theta}{\{d_\theta(x,y)\}^2} + \frac{(y+R\tan\theta-1)(h(x,y)-H)\frac{\partial h}{\partial y}(x,y)\sec^2\theta}{\{d_\theta(x,y)\}^4}d\theta &\text{(F.3)}\\
&= R^2\int_{-\Theta/2}^{\Theta/2}\frac{\sec^2\theta}{(x+R)^2+(y+R\tan\theta)^2+(h(x,y)-H)^2}d\theta\\
&\quad + R^2\int_{-\Theta/2}^{\Theta/2}\frac{(h(x,y)-H)\frac{\partial h}{\partial y}(x,y)(y+R\tan\theta-1)\sec^2\theta}{\{(x+R)^2+(y+R\tan\theta)^2+(h(x,y)-H)^2\}^2}d\theta &\text{(F.4)}\\
&= R^2\int_{-\tan\frac{\Theta}{2}}^{\tan\frac{\Theta}{2}}\frac{1}{(x+R)^2+(y+Rt)^2+(h(x,y)-H)^2}dt
\end{aligned}$$

$$+R^2\int_{-\tan\frac{\Theta}{2}}^{\tan\frac{\Theta}{2}}\frac{(h(x,y)-H)\frac{\partial h}{\partial y}(x,y)(y+Rt-1)}{\{(x+R)^2+(y+Rt)^2+(h(x,y)-H)^2\}^2}dt \tag{F.5}$$

$$=R^2\left[\frac{\tan^{-1}\left(\frac{y+Rt}{S(x,y)}\right)}{RS(x,y)}\right]_{-\tan\frac{\Theta}{2}}^{\tan\frac{\Theta}{2}}$$

$$-R^2(h(x,y)-H)\frac{\partial h}{\partial y}(x,y)\left[\frac{\tan^{-1}\left(\frac{y+Rt}{S(x,y)}\right)}{2RB^3(x,y)}+\frac{\frac{S^2(x,y)+(y+Rt)}{S^2(x,y)+(y+Rt)^2}}{2RS^2(x,y)}\right]_{-\tan\frac{\Theta}{2}}^{\tan\frac{\Theta}{2}} \tag{F.6}$$

$$=\left\{1-\frac{(h(x,y)-H)\frac{\partial h}{\partial y}(x,y)}{2S^2(x,y)}\right\}\frac{\tan^{-1}\left(\frac{y+R\tan\frac{\Theta}{2}}{S(x,y)}\right)-\tan^{-1}\left(\frac{y-R\tan\frac{\Theta}{2}}{S(x,y)}\right)}{S(x,y)/R}$$

$$-\frac{R(h(x,y)-H)\frac{\partial h}{\partial y}(x,y)}{2S^2(x,y)}$$

$$\times\left\{\frac{S^2(x,y)+(y+R\tan\frac{\Theta}{2})}{S^2(x,y)+(y+R\tan\frac{\Theta}{2})^2}-\frac{S^2(x,y)+(y-R\tan\frac{\Theta}{2})}{S^2(x,y)+(y-R\tan\frac{\Theta}{2})^2}\right\} \tag{F.7}$$

$$=\left\{1-\frac{(h(x,y)-H)\frac{\partial h}{\partial y}(x,y)}{2S^2(x,y)}\right\}\frac{\tan^{-1}\left(\frac{y+R\tan\frac{\Theta}{2}}{S(x,y)}\right)-\tan^{-1}\left(\frac{y-R\tan\frac{\Theta}{2}}{S(x,y)}\right)}{S(x,y)/R}$$

$$+\frac{R^2\tan\frac{\Theta}{2}(h(x,y)-H)\frac{\partial h}{\partial y}(x,y)\{(2y-1)S^2(x,y)+y^2-R^2\tan^2\frac{\Theta}{2}\}}{S^2(x,y)\{S^2(x,y)+(y+R\tan\frac{\Theta}{2})^2\}\{S^2(x,y)+(y-R\tan\frac{\Theta}{2})^2\}}, \tag{F.8}$$

where $S(x,y)=\sqrt{(x+R)^2+(h(x,y)-H)^2}$.

F.2 Condition for Explicitly Calculating the Normalization Constant in the Far-Field Case

We show how the condition given by Eq. (6.10) can be reformatted for the far-field scenario assumed in Sec. 6.3.1.2. When $R\to\infty$ with $H=aR$, f_2 is given by Eq. (6.15) and the condition becomes

$$1+a^2\cos^2\theta > a\sin\theta\cos\theta\frac{\partial h}{\partial y}(x,y),\quad \forall|\theta|\le\frac{\Theta}{2}. \tag{F.9}$$

This can be rewritten as

$$\left|\frac{\partial h}{\partial y}(x,y)\right| < \frac{1+a^2\cos^2\theta}{a\sin\theta\cos\theta},\quad \forall\theta\in\left(0,\frac{\Theta}{2}\right]. \tag{F.10}$$

Note the absolute-value sign and the corresponding change in the range for θ. Let $q(\theta)$ denote the right-hand-side equation above, and then the condition becomes $\left|\frac{\partial h}{\partial y}(x,y)\right| < \min_{\theta\in(0,\Theta/2]} q(\theta)$. Since

$$q'(\theta) = \frac{\tan^2\theta - 1 - a^2}{a\sin^2\theta}, \tag{F.11}$$

$q'(\theta)$ is negative for small θ's, increases as θ becomes larger, and $q'(\theta) = 0$ for $\theta = \tan^{-1}(\sqrt{1+a^2})$. The minimum of $q(\theta)$ is achieved at $\theta = \tan^{-1}(\sqrt{1+a^2})$ when it is in $(0,\Theta/2]$ and at $\theta = \Theta/2$ otherwise. The condition can be written as in Eq. (6.16) since $q(\sqrt{1+a^2}) = 2\sqrt{1+a^2}/a$. Note that the following is a sufficient condition for satisfication of Eq. (6.16) due to the fact that $q(\theta)$ can be written as $(\sec\frac{\Theta}{2}/a + a\cos\frac{\Theta}{2})/\sin\frac{\Theta}{2}$ and $x+y \geq 2\sqrt{xy}$:

$$\left|\frac{\partial h}{\partial y}(x,y)\right| < \begin{cases} 2/\sin(\frac{\Theta}{2}), & \Theta \leq 2\tan^{-1}(\sqrt{1+a^2}) \\ \sqrt{8/a}, & \Theta > 2\tan^{-1}(\sqrt{1+a^2}). \end{cases} \tag{F.12}$$

APPENDIX G

Stationary Phase Approximation of the PTR for FBP along Curves

We present a detailed derivation of Eq. (6.21), an approximation of the PTR for FBPC. By ignoring the normalization factor, the PTR for a point target at (x_0, y_0) can be written as

$$\int_{-\Theta/2}^{\Theta/2} f_2(x,y;\theta)\,\mathrm{sinc}(\Delta q_\theta)\,\mathrm{e}^{j\pi K\Delta q_\theta}\,d\theta - j\frac{1}{\pi K}\int_{-\Theta/2}^{\Theta/2} f_2(x,y;\theta)\,\mathrm{dsinc}(\Delta q_\theta)\,\mathrm{e}^{j\pi K\Delta q_\theta}\,d\theta. \tag{G.1}$$

Since the amplitude parts of the integrands slowly vary over θ and the offset ratio K is large in general, we can use the method of stationary phase.

The dominant frequency θ_d is the look angle θ that makes the derivative of the phase (exponent) equal to zero, i.e., θ_d satisfies $\left.\frac{dq_\theta}{d\theta}\right|_{\theta_d} = 0$. The derivative of q_θ is

$$\begin{aligned}\frac{dq_\theta}{d\theta} &= \frac{d}{d\theta}\left\{\sqrt{S^2(x,y)+(y+R\tan\theta)^2} - \sqrt{S^2(x_0,y_0)+(y_0+R\tan\theta)^2}\right\} \\ &= R\sec^2\theta\left\{\frac{y+R\tan\theta}{\sqrt{S^2(x,y)+(y+R\tan\theta)^2}} - \frac{y_0+R\tan\theta}{\sqrt{S^2(x_0,y_0)+(y_0+R\tan\theta)^2}}\right\}.\end{aligned} \tag{G.2}$$

Recall that $S(x,y)$ is shorthand notation for $\sqrt{(x+R)^2+(h(x,y)-H)^2}$. Thus, we have

$$\frac{y+R\tan\theta_d}{\sqrt{S^2(x,y)+(y+R\tan\theta_d)^2}} = \frac{y_0+R\tan\theta_d}{\sqrt{S^2(x_0,y_0)+(y_0+R\tan\theta_d)^2}}. \tag{G.3}$$

Let $\sin\phi_d$ denote the value above, and then we have

$$\tan\phi_d = \frac{y+R\tan\theta_d}{S(x,y)} = \frac{y_0+R\tan\theta_d}{S(x_0,y_0)} = \frac{(y+R\tan\theta_d)-(y_0+R\tan\theta_d)}{S(x,y)-S(x_0,y_0)}. \tag{G.4}$$

Since $\tan\phi_d = (y-y_0)/(S(x,y)-S(x_0,y_0))$ from the last equality, we can solve for the tangent of θ_d

by using the first and second equality in Eq. (G.4) to yield:

$$\tan\theta_d = \frac{1}{R}\left\{\frac{S(x,y)(y-y_0)}{S(x,y)-S(x_0,y_0)} - y\right\} = \frac{1}{R}\left\{\frac{S(x_0,y_0)(y-y_0)}{S(x,y)-S(x_0,y_0)} - y_0\right\}. \tag{G.5}$$

The phase evaluated at the dominant frequency is

$$\begin{aligned} q_{\theta_d} &= r_{\theta_d}(x,y) - r_{\theta_d}(x_0,y_0) = d_{\theta_d}(x,y) - d_{\theta_d}(x_0,y_0) \\ &= \sqrt{S^2(x,y) + (y + R\tan\theta_d)^2} - \sqrt{S^2(x_0,y_0) + (y_0 + R\tan\theta_d)^2} \\ &= S(x,y)\sqrt{1 + \frac{(y-y_0)^2}{\{S(x,y)-S(x_0,y_0)\}^2}} - S(x_0,y_0)\sqrt{1 + \frac{(y-y_0)^2}{\{S(x,y)-S(x_0,y_0)\}^2}} \\ &= \{S(x,y)-S(x_0,y_0)\}\sqrt{1 + \frac{(y-y_0)^2}{\{S(x,y)-S(x_0,y_0)\}^2}} \\ &= \sqrt{\{S(x,y)-S(x_0,y_0)\}^2 + (y-y_0)^2}. \end{aligned} \tag{G.6}$$

By using the Taylor series expansion of q_θ about θ_d in the phase and using $\theta = \theta_d$ in the amplitude part of the integrand, Eq. (G.1) can be approximated as

$$\int_{-\Theta/2}^{\Theta/2} f_2(x,y;\theta_d)\left\{\mathrm{sinc}(\Delta q_{\theta_d}) - j\frac{1}{\pi K}\,\mathrm{dsinc}(\Delta q_{\theta_d})\right\} \mathrm{e}^{j\pi K\Delta\{q_{\theta_d} + q'(\theta_d)(\theta-\theta_d) + \frac{1}{2}q''(\theta_d)(\theta-\theta_d)^2 + \cdots\}}\, d\theta. \tag{G.7}$$

By dropping the second and higher order terms in the Taylor series expansion, we have

$$\Theta f_2(x,y;\theta_d)\left\{\mathrm{sinc}(\Delta q_{\theta_d}) - j\frac{1}{\pi K}\,\mathrm{dsinc}(\Delta q_{\theta_d})\right\} \mathrm{e}^{j\pi K\Delta q_{\theta_d}}. \tag{G.8}$$

In order to adjust to the approximation made, we re-normalize the PTR and finally get

$$\left|\bar{h}(x,y;x_0,y_0)\right| \approx \left|\mathrm{sinc}(\Delta q_{\theta_d}) - j\frac{1}{\pi K}\,\mathrm{dsinc}(\Delta q_{\theta_d})\right|. \tag{G.9}$$

Note that this approximation is valid only when $|\theta_d| \le \Theta/2$, which corresponds to small values of $(y - y_0)$.

APPENDIX H

Equivalence of Extended MCA and FMCA for Far-Field Imaging

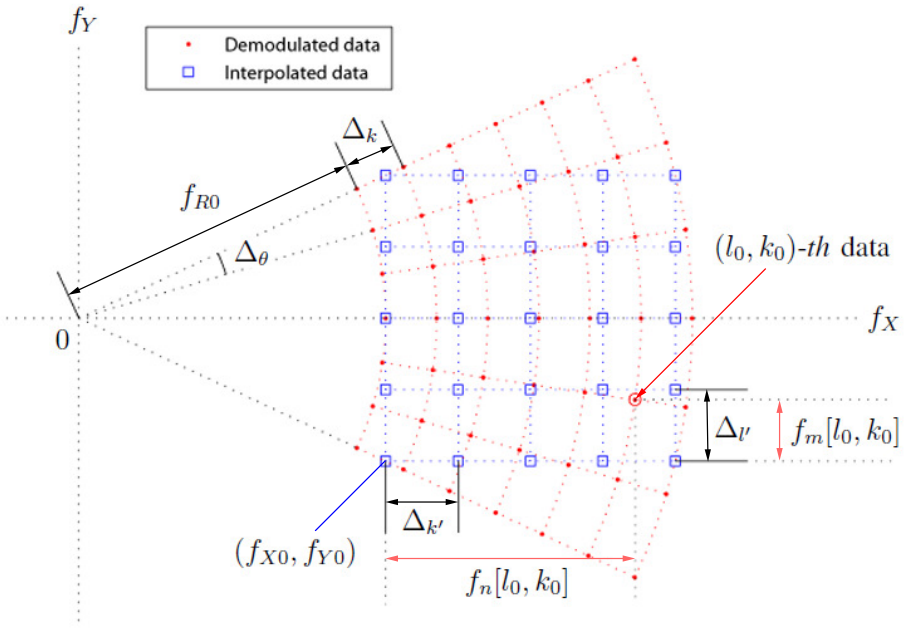

Figure H.1: Data grids and sampling parameters in the 2-D Fourier domain for SAR data acquired in the far field. The red dots represent polar-format grid of the demodulated data, and the blue squares represent the Cartesian grid of the interpolated data. f_{R0}, f_{X0}, and f_{Y0} denote the lowest spatial frequencies of the grids in the radial, range, and cross-range directions, respectively. Δ_k, Δ_θ, $\Delta_{k'}$, and $\Delta_{l'}$ denote the grid spacings in the radial, angular, range, and cross-range directions, respectively. $f_n[l_0,k_0]$ and $f_m[l_0,k_0]$ denote the relative coordinates of the sample point of $P[l_0,k_0]$ from the point (f_{X0},f_{Y0}) in the range and cross-range directions, respectively.

Here, we derive a sufficient condition for extended MCA and FMCA to be equivalent algorithms. The two autofocus algorithms are compared for a far-field imaging scenario where the elevations of the scene and the radar are the same.

The demodulated data are 2-D Fourier transformations of the reflectivity, sampled on a polar

grid, depicted as red dots in Fig. H.1. That is,

$$P[l,k] = G\left(\{f_{R0} + \Delta_k(k-1)\}\cos\theta_l, \{f_{R0} + \Delta_k(k-1)\}\sin\theta_l\right), \tag{H.1}$$

where $G(f_X, f_Y)$ is the 2-D Fourier transform of $g(x,y)$. f_{R0} is the lowest radial spatial frequency and Δ_k is the sampling interval of the radial spatial frequencies. PFA interpolates the data onto a Cartesian grid, which is depicted as blue squares in Fig. H.1, and then applies a 2-D inverse FFT to form an image. f_{X0} and f_{Y0} are the lowest range and cross-range spatial frequencies, respectively, of the Cartesian grid, and $\Delta_{k'}$ and $\Delta_{l'}$ are the grid spacings in the range and cross-range directions, respectively. The image reconstructed by PFA can be expressed as

$$\hat{g}_{\text{PFA}}[m,n] = \frac{C[m,n]}{M'N'} \sum_{l'=0}^{M'-1} \sum_{k'=0}^{N'-1} \sum_{l=1}^{N_\theta} \sum_{k=1}^{N_\rho} P[l,k]\Psi_{PC}[l',k';l,k]\, \mathrm{e}^{j2\pi\left(\frac{l'm}{M'} + \frac{k'n}{N'}\right)}, \tag{H.2}$$

where Ψ_{PC} is a polar-to-Cartesian interpolation kernel and $C[m,n] = \exp\left[j2\pi\left\{\frac{mf_{Y0}}{M'\Delta_{l'}} + \frac{nf_{X0}}{N'\Delta_{k'}}\right\}\right]$. N' and M' are the number of Cartesian-grid samples in the range and cross-range directions, respectively.

FMCA assumes that there is a set of indices $\mathcal{D}$ corresponding to a low-return region and estimates the phase errors with

$$\hat{\boldsymbol{\phi}}^*_{\text{PFA}} = -\angle\left\{\min_{\|\mathbf{h}\|_2=1} \|\boldsymbol{\Phi}_{\text{PFA},\,\mathcal{D}}\,\mathbf{h}\|_2\right\}, \tag{H.3}$$

where $\boldsymbol{\Phi}_{\text{PFA},\,\mathcal{D}}$ is a $|\mathcal{D}|$-by-N_θ matrix, composed of rows: $\{\boldsymbol{\Phi}_{\text{PFA},\,[m,n]} | [m,n] \in \mathcal{D}\}$. The l-th entry of $\boldsymbol{\Phi}_{\text{PFA},\,[m,n]}$ is

$$\boldsymbol{\Phi}^{(l)}_{\text{PFA},\,[m,n]} = \frac{C[m,n]}{M'N'} \sum_{l'=0}^{M'-1} \sum_{k'=0}^{N'-1} \sum_{k=1}^{N_\rho} \tilde{P}[l,k]\Psi_{PC}[l',k';l,k]\, \mathrm{e}^{j2\pi\left(\frac{l'm}{M'} + \frac{k'n}{N'}\right)}. \tag{H.4}$$

Now, note that extended MCA and FMCA are equivalent algorithms if $\boldsymbol{\Phi}_{\mathcal{S}} = \boldsymbol{\Phi}_{\text{PFA},\,\mathcal{D}}$. For the purpose of comparison, we choose the low-return coordinates for the two algorithms to be the same. That is, $|\mathcal{D}| = |\mathcal{S}|$ and $\left(\frac{m}{M'\Delta_{l'}}, \frac{n}{N'\Delta_{k'}}\right) \in \mathcal{S}, \forall [m,n] \in \mathcal{D}$. When the radar elevation is equal to zero[1], the functions $f_2(x,y;\theta)$ of Eq. (6.15) and $r_\theta(x,y)$ of Eq. (6.14) reduce to 1 and $x\cos\theta + y\sin\theta$, respectively. Equation (6.31) then simplifies to

$$\boldsymbol{\Phi}^{(l)}_{(x,y)} = \frac{1}{\rho_0(N_\rho - 1)N_\theta} \sum_{k=1}^{N_\rho} \rho_k \tilde{P}[l,k]\, \mathrm{e}^{j2\pi(x\cos\theta_l + y\sin\theta_l)\rho_k}. \tag{H.5}$$

[1] We can assume that the elevations of the radar and terrain are both zero, without loss of generality.

From Eqs. (H.4) and (H.5), a sufficient condition for the algorithms to be equivalent is

$$\sum_{l'=0}^{M'-1}\sum_{k'=0}^{N'-1}\Psi_{PC}[l',k';l,k]\,\mathrm{e}^{j2\pi\left(\frac{l'm}{M'}+\frac{k'n}{N'}\right)}=\frac{\rho_k}{C[m,n]}\mathrm{e}^{j2\pi\left(\frac{m}{M'\Delta_{l'}}\sin\theta_l+\frac{n}{N'\Delta_{k'}}\cos\theta_l\right)\rho_k},\quad\forall\, l,k, \tag{H.6}$$

where the constants are discarded for simplicity. Since the left-hand side of the equation is the inverse FFT of Ψ_{PC} as a function of l' and k', the sufficient condition is equivalent to the interpolation kernel satisfying the following:

$$\Psi_{PC}[l',k';l,k]=\sum_{m=0}^{M'-1}\sum_{n=0}^{N'-1}\frac{\rho_k}{C[m,n]}\mathrm{e}^{j2\pi\left(\frac{\rho_k\sin\theta_l m}{M'\Delta_{l'}}+\frac{\rho_k\cos\theta_l n}{N'\Delta_{k'}}\right)}\mathrm{e}^{-j2\pi\left(\frac{l'm}{M'}+\frac{k'n}{N'}\right)} \tag{H.7}$$

$$=\rho_k\left[\sum_{m=0}^{M'-1}\exp\left\{-j2\pi\frac{m}{M'}\left(l'-\frac{\rho_k\sin\theta_l-f_{Y0}}{\Delta_{l'}}\right)\right\}\right]\times\left[\sum_{n=0}^{N'-1}\exp\left\{-j2\pi\frac{n}{N'}\left(k'-\frac{\rho_k\cos\theta_l-f_{X0}}{\Delta_{k'}}\right)\right\}\right] \tag{H.8}$$

$$=C_R[l',k';l,k]\,\mathrm{asinc}\left(l'-\frac{f_m[l,k]}{\Delta_{l'}},M'\right)\mathrm{asinc}\left(k'-\frac{f_n[l,k]}{\Delta_{k'}},N'\right), \tag{H.9}$$

where $C_R[l',k';l,k]=\rho_k\exp\left[-j\pi\left\{\frac{M'-1}{M'}\left(l'-f_m[l,k]/\Delta_{l'}\right)+\frac{N'-1}{N'}\left(k'-f_n[l,k]/\Delta_{k'}\right)\right\}\right]$. As depicted in Fig. H.1, $f_m[l,k]=\rho_k\sin\theta_l-f_{Y0}$ and $f_n[l,k]=\rho_k\cos\theta_l-f_{X0}$ are the relative coordinates of the polar-format data indexed by $[l,k]$ from the lower-left sample of the Cartesian grid in the range and cross-range direction, respectively. Here, $\mathrm{asinc}(x,N)=\sin(\pi x)/\sin(\frac{\pi}{N}x)$ is a periodic sinc function.

BIBLIOGRAPHY

[1] D. C. Munson, Jr., J. D. O'Brien, and W. K. Jenkins, "A tomographic formulation of spotlight-mode synthetic aperture radar," *Proc. IEEE*, vol. 71, no. 8, pp. 917–925, Aug. 1983.

[2] M. D. Desai and W. K. Jenkins, "Convolution backprojection image reconstruction for spotlight mode synthetic aperture radar," *IEEE Trans. Image Process.*, vol. 1, no. 4, pp. 505–517, Oct. 1992.

[3] A. F. Yegulalp, "Fast backprojection algorithm for synthetic aperture radar," in *Proc. IEEE Radar Conf.*, Waltham, MA, Apr. 1999, pp. 60–65.

[4] Y. Ding and D. C. Munson, Jr., "A fast back-projection algorithm for bistatic SAR imaging," in *Proc. IEEE Int. Conf. Image Processing*, 2002, pp. 449–452.

[5] L. M. H. Ulander, H. Hellsten, and G. Stenström, "Synthetic-aperture radar processing using fast factorized back-projection," *IEEE Trans. Aerosp. Electron. Syst.*, vol. 39, no. 3, pp. 760–776, Jul. 2003.

[6] C. V. Jakowatz, D. E. Wahl, P. H. Eichel, D. C. Ghiglia, and P. A. Thompson, *Spotlight-Mode Synthetic Aperture Radar: A Signal Processing Approach*. Boston, MA: Kluwer Academic, 1996.

[7] G. A. Bendor and T. W. Gedra, "Single-pass fine-resolution sar autofocus," *NAECON*, pp. 482–488, 1983.

[8] P. H. Eichel, D. C. Ghiglia, C. V. Jakowatz, and D. E. Wahl, "Phase-gradient autofocus for SAR phase correction: Explanation and demonstration of algorithmic steps," in *Proc. Digital Signal Processing Workshop*, Starved Rock State Park, IL, Sep. 1992, pp. 6.6.1–6.6.2.

[9] C. V. Jakowatz and D. E. Wahl, "Eigenvector method for maximum-likelihood estimation of phase errors in synthetic-aperture-radar imagery," *JOSA A*, vol. 10, no. 12, pp. 2539–2546, 1993.

[10] J. R. Fienup and J. J. Miller, "Aberration correction by maximizing generalized sharpness metrics," *JOSA A*, vol. 20, no. 4, pp. 609–620, 2003.

[11] R. L. Morrison, M. N. Do, and D. C. Munson, "Sar image autofocus by sharpness optimization: A theoretical study," *IEEE Transactions on Image Processing*, vol. 16, no. 9, pp. 2309–2321, 2007.

[12] F. Berizzi and G. Corsini, "Autofocusing of inverse synthetic aperture radar images using contrast optimization," *IEEE Trans. Aerosp. Electron. Syst.*, vol. 32, no. 3, pp. 1185–1191, Jul. 1996.

[13] J. Kolman, "PACE: An autofocus algorithm for SAR," in *IEEE International Radar Conference*. IEEE, 2005, pp. 310–314.

[14] A. F. Yegulalp, "Minimum entropy sar autofocus," in *Adaptive Sensor Array Processing (ASAP) Workshop, MIT Lincoln Laboratory, Lexington, MA*, 1999.

[15] R. L. Morrison and J. Munson, D. C., "An experimental study of a new entropy based SAR autofocus technique," in *Proc. IEEE Int. Conf. Image Processing*, 2002, pp. 441–444.

[16] T. J. Kragh, "Monotonic iterative algorithm for minimum-entropy autofocus," in *Proc. Adaptive Sensor Array Processing Workshop*, MIT Lincoln Laboratory, MA, Jun. 2006.

[17] L. Xi, L. Guosui, and J. Ni, "Autofocusing of ISAR images based on entropy minimization," *IEEE Trans. Aerosp. Electron. Syst.*, vol. 35, no. 4, pp. 1240–1252, Oct. 1999.

[18] R. A. Wiggins, "Minimum entropy deconvolution," *Geoexploration*, vol. 16, no. 1, pp. 21–35, 1978.

[19] O. Shalvi and E. Weinstein, "New criteria for blind deconvolution of nonminimum phase systems (channels)," *IEEE Transactions on Information Theory*, vol. 36, no. 2, pp. 312–321, 1990.

[20] C. Cafforio, C. Prati, and F. Rocca, "Full resolution focusing of SEASAT SAR images in the frequency-wave number domain," *International Journal of Remote Sensing*, vol. 12, no. 3, pp. 491–510, 1991.

[21] R. L. Morrison, Jr., M. N. Do, and D. C. Munson, Jr., "MCA: A multichannel approach to SAR autofocus," *IEEE Trans. Image Process.*, vol. 18, no. 4, pp. 840–853, Apr. 2009.

[22] R. L. Morrison and M. N. Do, "Multichannel autofocus algorithm for synthetic aperture radar," in *Proc. IEEE Int. Conf. Image Processing*, Atlanta, GA, Oct. 2006, pp. 2341–2344.

[23] H. J. Cho and D. C. Munson, Jr., "Overcoming polar-format issues in multichannel SAR autofocus," in *Proc. 42nd Asilomar Conf. Signals, Systems, and Computers*, Pacific Grove, CA, Oct. 2008, pp. 523–527.

[24] ——, "Overcoming polar-format issues in synthetic aperture radar multichannel autofocus," *IET Radar, Sonar & Navigation*, vol. 10, no. 1, pp. 132–139, 2016.

[25] Synthetic aperture radar imagery. Sandia National Laboratories. Albuquerque, NM. [Online]. Available: http://www.sandia.gov/radar/imagery.html

[26] G. W. Stewart, "Perturbation theory for the singular value decomposition," in *SVD and Signal Processing, II: Algorithms, Analysis and Applications*. Elsevier, 1990, pp. 99–109.

[27] M. H. Hayes, "The reconstruction of a multidimensional sequence from phase or magnitude of its Fourier transform," *IEEE Trans. Acoust., Speech, Signal Process.*, vol. 30, no. 2, pp. 140–154, Apr. 1982.

[28] D. C. Munson, Jr. and J. L. C. Sanz, "Phase-only image reconstruction from offset Fourier data," in *Proc. SPIE 556, Int. Conf. Speckle*, San Diego, CA, Aug. 1985, pp. 227–235.

[29] J. Hsieh, *Computed Tomography: Principles, Design, Artifacts, and Recent Advances*. SPIE, 2003.

[30] W.-H. Hsiao and R. P. Millane, "Effects of Fourier-plane amplitude and phase errors on image reconstruction. I. Small amplitude errors," *JOSA A*, vol. 24, no. 10, pp. 3180–3188, Oct. 2007.

[31] D. S. Jones and M. Kline, "Asymptotic expansion of multiple integrals and the method of stationary phase," *J. Math. and Phys.*, vol. 37, pp. 1–28, 1958.

[32] H. J. Cho and D. C. Munson, Jr., "Multichannel SAR autofocus using multiple low-return constraints," in *Proc. IEEE Int. Conf. Acoustic, Speech, and Signal Processing*, Dallas, TX, Mar. 2010, pp. 1346–1349.

[33] K.-H. Liu and D. C. Munson, Jr., "Fourier-domain multichannel autofocus for synthetic aperture radar," *IEEE Trans. Image Process.*, vol. 20, no. 12, pp. 3544–3552, Dec. 2011.

[34] S. Xiao, D. C. Munson, Jr., S. Basu, and Y. Bresler, "An $N^2 \log N$ back-projection algorithm for SAR image formation," in *Proc. 34th Asilomar Conf. on Signals, Systems, and Computers*, Pacific Grove, CA, Nov. 2000, pp. 3–7.

[35] C. V. Jakowatz Jr, D. E. Wahl, and D. A. Yocky, "Beamforming as a foundation for spotlight-mode SAR image formation by backprojection," in *SPIE Defense and Security Symposium*, vol. 6970. International Society for Optics and Photonics, 2008, pp. 69 700Q–1–69 700Q–15.

[36] ——, "A beamforming algorithm for bistatic SAR image formation," in *SPIE Defense, Security, and Sensing*, vol. 7699. International Society for Optics and Photonics, 2010, pp. 769 902–1–769 902–6.

[37] H. Choi and D. C. Munson, Jr., "Direct-Fourier reconstruction in tomography and synthetic aperture radar," *Int. J. Imag. Syst. and Technol.*, vol. 9, no. 1, pp. 1–13, 1998.

[38] N. E. Doren, C. V. Jakowatz, D. E. Wahl, and P. A. Thompson, "General formulation for wavefront curvature correction in polar-formatted spotlight-mode SAR images using space-variant post-filtering," in *Proc. IEEE Int. Conf. Image Processing*, Santa Barbara, CA, Oct. 1997, pp. 861–864.

[39] C. J. Nolan and M. Cheney, "Synthetic aperture inversion," *Inverse Problems*, vol. 18, no. 1, pp. 221–235, 2002.

[40] C. Nolan and M. Cheney, "Synthetic aperture inversion for arbitrary flight paths and nonflat topography," *Image Processing, IEEE Transactions on*, vol. 12, no. 9, pp. 1035–1043, Sept 2003.

[41] C. Yarman, B. Yazici, and M. Cheney, "Bistatic synthetic aperture radar imaging for arbitrary flight trajectories," *Image Processing, IEEE Transactions on*, vol. 17, no. 1, pp. 84–93, Jan 2008.

[42] D. C. Munson, Jr. and J. L. C. Sanz, "Image reconstruction from frequency-offset Fourier data," *Proc. IEEE*, vol. 72, no. 6, pp. 661–669, Jun. 1984.

[43] H. J. Cho and D. C. Munson, Jr., "CBP-based multichannel autofocus for near-field SAR imaging," in *Proc. SPIE 8051, Algorithms for Synthetic Aperture Radar Imagery XVIII*, Orlando, FL, Apr. 2011, pp. 80 510K–80 510K–9.

[44] S. E. Reutebuch, R. J. McGaughey, H.-E. Andersen, and W. W. Carson, "Accuracy of a high-resolution lidar terrain model under a conifer forest canopy," *Canadian Journal of Remote Sensing*, vol. 29, no. 5, pp. 527–535, 2003.

[45] A. Hirano, R. Welch, and H. Lang, "Mapping from ASTER stereo image data: DEM validation and accuracy assessment," *ISPRS Journal of Photogrammetry and Remote Sensing*, vol. 57, no. 5, pp. 356–370, 2003.

[46] N. Marechal, "Tomographic formulation of interferometric sar for terrain elevation mapping," *IEEE transactions on geoscience and remote sensing*, vol. 33, no. 3, pp. 726–739, 1995.

[47] F. Nex and F. Remondino, "UAV for 3D mapping applications: a review," *Applied Geomatics*, vol. 6, no. 1, pp. 1–15, 2014.

[48] The national map: Elevation. [Online]. Available: http://nationalmap.gov/elevation.html

[49] O. Arikan and J. Munson, D. C., "A new back-projection algorithm for spotlight-mode SAR and ISAR," in *Proc. SPIE 1058, High Speed Computing II*, Los Angeles, CA, Jan. 1989, pp. 107–117.

[50] S. Xiao, "Topics in CT and SAR imaging: fast back-projection algorithms and optimal antenna spacings," Ph.D. dissertation, University of Illinois at Urbana-Champaign, Urbana, IL, 2001.

[51] C. V. Jakowatz Jr and D. E. Wahl, "Considerations for autofocus of spotlight-mode SAR imagery created using a beamforming algorithm," in *SPIE Defense, Security, and Sensing*, vol. 7337. International Society for Optics and Photonics, 2009, pp. 73 370A–1–73 370A–9.

[52] J. N. Ash, "An autofocus method for backprojection imagery in synthetic aperture radar," *IEEE Geoscience and Remote Sensing Letters*, vol. 9, no. 1, pp. 104–108, Jan 2012.

[53] J. Torgrimsson, P. Dammert, H. Hellsten, and L. M. Ulander, "Autofocus and analysis of geometrical errors within the framework of fast factorized back-projection," in *SPIE Defense+ Security*. International Society for Optics and Photonics, 2014, pp. 909 303–909 303.

[54] J. J. Duistermaat and L. Hormander, *Fourier integral operators*. Springer, 1996, vol. 2.

[55] N. Bleistein and R. A. Handelsman, *Asymptotic expansion of integrals*. Courier Corportation, 1975.

[56] F. Natterer, *The mathematics of computerized tomography*. Siam, 1986, vol. 32.